Theses and Dissertations

Summer 2010

Evaluation of attenuation and scatter correction requirements in small animal PET and SPECT imaging

Arda Bekir Konik
University of Iowa

EVALUATION OF ATTENUATION AND SCATTER CORRECTION
REQUIREMENTS IN SMALL ANIMAL PET AND SPECT IMAGING

by

Arda Bekir Konik

An Abstract

Of a thesis submitted in partial fulfillment of the
requirements for the Doctor of Philosophy degree
in Physics in
the Graduate College of
The University of Iowa

July 2010

Thesis Supervisor: Professor Mark T. Madsen

ABSTRACT

Positron emission tomography (PET) and single photon emission tomography (SPECT) are two nuclear emission-imaging modalities that rely on the detection of high-energy photons emitted from radiotracers administered to the subject. The majority of these photons are attenuated (absorbed or scattered) in the body, resulting in count losses or deviations from true detection, which in turn degrades the accuracy of images. In clinical emission tomography, sophisticated correction methods are often required employing additional x-ray CT or radionuclide transmission scans. Having proven their potential in both clinical and research areas, both PET and SPECT are being adapted for small animal imaging. However, despite the growing interest in small animal emission tomography, little scientific information exists about the accuracy of these correction methods on smaller size objects, and what level of correction is required.

The purpose of this work is to determine the role of attenuation and scatter corrections as a function of object size through simulations. The simulations were performed using Interactive Data Language (IDL) and a Monte Carlo based package, Geant4 application for emission tomography (GATE). In IDL simulations, PET and SPECT data acquisition were modeled in the presence of attenuation. A mathematical emission and attenuation phantom approximating a thorax slice and slices from real PET/CT data were scaled to 5 different sizes (i.e., human, dog, rabbit, rat and mouse). The simulated emission data collected from these objects were reconstructed. The reconstructed images, with and without attenuation correction, were compared to the ideal (i.e., non-attenuated) reconstruction. Next, using GATE, scatter fraction values (the ratio of the scatter counts to the total counts) of PET and SPECT scanners were measured for various sizes of NEMA (cylindrical phantoms representing small animals and human), MOBY (realistic mouse/rat model) and XCAT (realistic human model) digital phantoms. In addition, PET projection files for different sizes of MOBY phantoms were

reconstructed in 6 different conditions including attenuation and scatter corrections. Selected regions were analyzed for these different reconstruction conditions and object sizes. Finally, real mouse data from the real version of the same small animal PET scanner we modeled in our simulations were analyzed for similar reconstruction conditions.

Both our IDL and GATE simulations showed that, for small animal PET and SPECT, even the smallest size objects (~2 cm diameter) showed ~15% error when both attenuation and scatter were not corrected. However, a simple attenuation correction using a uniform attenuation map and object boundary obtained from emission data significantly reduces this error in non-lung regions (~1% for smallest size and ~6% for largest size). In lungs, emissions values were overestimated when only attenuation correction was performed. In addition, we did not observe any significant improvement between the uses of uniform or actual attenuation map (e.g., only ~0.5% for largest size in PET studies). The scatter correction was not significant for smaller size objects, but became increasingly important for larger sizes objects.

These results suggest that for all mouse sizes and most rat sizes, uniform attenuation correction can be performed using emission data only. For smaller sizes up to ~ 4 cm, scatter correction is not required even in lung regions. For larger sizes if accurate quantization needed, additional transmission scan may be required to estimate an accurate attenuation map for both attenuation and scatter corrections.

Abstract Approved: _____

Thesis Supervisor

_____

Title and Department

_____

Date

EVALUATION OF ATTENUATION AND SCATTER CORRECTION
REQUIREMENTS IN SMALL ANIMAL PET AND SPECT IMAGING

by

Arda Bekir Konik

A thesis submitted in partial fulfillment of the
requirements for the Doctor of
Philosophy degree in Physics in
the Graduate College of
The University of Iowa

July 2010

Thesis Supervisor: Professor Mark T. Madsen

Graduate College
The University of Iowa
Iowa City, Iowa

CERTIFICATE OF APPROVAL

_____

PH.D. THESIS

_____

This is to certify that the Ph. D. thesis of

Arda Bekir Konik

has been approved by the Examining Committee
for the thesis requirement for the Doctor of
Philosophy degree in Physics at the July 2010 graduation.

Thesis Committee: _____
                      Mark T. Madsen, Thesis Supervisor

                      _____
                      John J. Sunderland

                      _____
                      Richard D. Hichwa

                      _____
                      Vincent G. J. Rodgers

                      _____
                      Wayne N. Polyzou

                      _____
                      William H. Klink

To Mali

ACKNOWLEDGEMENTS

TABLE OF CONTENTS

LIST OF TABLES

LIST OF FIGURES

CHAPTER I

INTRODUCTION

The images in positron emission tomography (PET) and single photon emission computed tomography (SPECT) are based on the detection of high-energy photons emitted by minute amounts of radiotracers introduced into a subject. The objective of emission tomography is to estimate the internal distribution of these radiolabels, which reveal physiological information non-invasively. In order to achieve this, projections are acquired at multiple angles through the body. With ideal projections, the three-dimensional emission image should be accurately reconstructed. In reality, however, photons are absorbed and mostly scattered in the attenuating medium (e.g., tissue, bones etc) distorting the projection files, and thereby degrading the quality and accuracy of reconstructed images. Various attenuation and scatter correction methods have been developed to compensate for these effects. In clinical emission tomography, sophisticated correction methods employing x-ray computed tomography (CT) or radionuclide transmission scans, are often required. Combined PET/CT [1] and SPECT/CT [2] cameras have been built to fuse emission images with anatomical data and to provide accurate attenuation maps to be used in scatter and attenuation corrections. Having proven their potential in both clinical and research areas, these combined scanners are being adapted for small animal imaging using similar correction approaches [3-5]. However, photon attenuation and its negative impact on images in small animal imaging are significantly less than in human imaging. Hence, the value of transmission-based corrections is not obvious for small animal imaging considering the additional cost and complexity of these methods. In fact, sometimes small animal PET imaging is performed without applying attenuation or scatter correction despite the CT capabilities of the scanners [6]. In addition, it has been reported that for small mouse-sized objects, the scatter correction employing the object attenuation map could not model the scatter

properly, since the majority of the scatter arises from environmental and detector scatter rather than the object itself [7]. In these respects, it is worthwhile to understand the relation between object sizes and the effectiveness of the correction methods. There has been an extensive amount of research done on the effects of attenuation and correction methods; however, none of these studies appeared to have investigated these effects for an extended range of sizes (Zaidi et al. and references therein) [8, 9]. Thus, the objective of this study is to determine the effect of photon interactions and the role of attenuation and scatter corrections over a wide range of object sizes.

Our study is mostly based on computer simulations using Interactive Data Language (IDL), and a Monte Carlo based package, Geant4 application for emission tomography (GATE) [10]. In addition, we used real small animal PET data to validate the simulation results. Our results confirm that transmission based attenuation and scatter corrections are essential for human size objects. In small animal imaging however, simple corrections based on emission data alone may be sufficient for most mouse and rat studies. The research plan is summarized in the following paragraphs, and details presented in the corresponding chapters.

Research Plan

Computer simulations are indispensable tools of nuclear medicine since they allow conducting multiple experiments in much shorter times than physical measurements in which typically very expensive equipment is used. Simulations can provide direct evaluation of certain quantities (e.g., scatter counts) that can only be estimated by indirect measurements when real devices are used. In addition, unlike real experiments, simulations allow the user to manipulate the parameters (e.g., phantom size, amount of radioactivity etc.) of a study with ease.

This research consists of a series of realistic simulations of SPECT and PET in order to determine the role of attenuation and scatter corrections as a function of object size.

Preliminary Studies with IDL

Using IDL, PET and SPECT scanner simulations were performed employing a mathematical emission and attenuation phantom that approximated a slice through the thorax. In addition, real data from a human PET/CT study were employed in the simulations. Slices from PET data were used as the unknown radioactivity distribution and the CT data as the associated attenuation map. The simulations were performed in the presence of attenuation, however without including the scatter effect.

Both attenuation objects were scaled to 5 different sizes approximating a human, dog, rabbit, rat and mouse: 36 cm, 18 cm, 9 cm, 4.5 cm and 2.25 cm. The projection files (sinogram data) obtained from these radioactivity distributions are reconstructed (using filter back projection, FBP) in three different conditions: perfect correction; uniform attenuation correction based on boundary information; and without attenuation correction.

- Perfect correction: This represents the ideal reconstruction of the true radioactivity distribution, where projection files are obtained in the absence of attenuation material. This serves as the reference image for the comparison of reconstructed images.

- Uniform attenuation correction using body contour: The projections are obtained in the presence of attenuation effect. This correction is performed using the emission data only, obtained through acquisition. The emission data is employed to specify the boundaries of the image. For the uniform attenuation map inside these boundaries, the water attenuation coefficient is assumed (0.096 cm^{-1} and 0.155 cm^{-1} for PET and SPECT, respectively) and incorporated in the reconstruction algorithm.

- Without Attenuation correction: The projections obtained in the presence of attenuation effect are directly reconstructed without applying any attenuation correction.

The reconstructions with and without attenuation corrections were compared to the perfect reconstruction for various regions selected on both mathematical phantom and real slices.

GATE Simulations

GATE is a dedicated Monte Carlo software package for emission tomography. This software allows for modeling detailed scanner geometries and radiation interactions with matter, tracking events (recording position, time and energy of an event), and creating various types of output files including projection files. Owing to its versatility, GATE is used worldwide by researchers in the emission tomography field, and many papers describing experiments based on GATE simulations have been published in respected journals [11].

We used GATE to perform PET and SPECT simulations of several digital phantoms—including the NEMA (cylindrical phantoms representing mouse, rat and human) [12, 13], XCAT (realistic human model) [14] and MOBY (realistic mouse/rat model) [15]—over a wide range of sizes. Our GATE simulations consisted of two main parts: Scatter Fraction measurements and analysis of reconstructed images.

Scatter Fraction Measurements

Scatter fraction, the ratio of scatter counts to the total counts, is a useful parameter to quantify the magnitude of scatter and to estimate the potential impact of scatter on the reconstructed images. Scatter fraction measurements of various phantoms - listed above - were performed using a human PET scanner model along with small animal PET and SPECT scanner models. In order to cover a wide range of energies, in addition to PET

annihilation photons (511 keV), we employed three different SPECT radionuclides having different photon emission energies: ^{99m}Tc (140 keV), ^{111}In (171 and 245 keV) and ^{125}I (~30 keV).

Analysis of reconstructed images

Projection files for six different sizes (~2.1-6.4 cm diameter) of MOBY phantoms were obtained and reconstructed to analyze the impact of photon interactions on the reconstructed images and evaluate the requirement of attenuation and scatter corrections. The projection files were reconstructed using both our IDL routines and a more professional reconstruction code. Reconstruction were performed for 6 different conditions:

- Scatter correction + accurate attenuation correction
- Scatter correction + simple attenuation correction
- Accurate attenuation correction only
- Simple attenuation correction only
- Scatter correction only
- No correction

where "simple attenuation correction" used the uniform attenuation map (water attenuation coefficients in the object boundary) as explained in the IDL study, and "accurate attenuation correction" employed actual attenuation coefficient distribution. The reconstructed images were scaled to a single size and analyzed for various regions. The mean errors were calculated with respect to the perfect reconstruction, which is the first condition in the list above.

Experimental Study

Existing real mouse sinogram data collected from the actual small animal PET scanner was reconstructed with and without corrections following similar approaches applied for the GATE simulation work.

CHAPTER II

BACKGROUND AND SIGNIFICANCE

Tomographic Imaging

Tomography has a wide range of applications in many fields such as astronomy, geophysics and medical imaging, all of which share the same general objective: reconstructing the volumetric image of an unknown object from external measurements only. The tomographic methodologies in medical imaging include x-ray computed tomography (CT), magnetic resonance imaging (MRI), and emission tomography (ET). Each methodology is sensitive to different properties of an unknown object. CT measures the distribution of attenuation coefficients, MRI—e.g., proton density[1], and emission tomography—radionuclide distribution. The basic mathematical principles of projection-based tomography are briefly described in the following paragraphs.

Projections in tomography are collected at multiple angles through an unknown object. Each projection profile (projection bin) p(ϕ, t) corresponds to a collection of line integrals (parallel, cone beam or fan beam organization) through the object of interest. A simple simulation example of parallel line integrals through a 2D image is illustrated in Figure 1, where (t, s) is the rotated coordinate system at angle ϕ with respect to (x, y) coordinate system. The relation between these two coordinate systems is as follows:

$$t = x\cos\phi + y\sin\phi$$
$$s = -x\sin\phi + y\cos\phi$$

(1)

Hence, a single line integral at an angle ϕ along the line can be represented as [16, 17]:

---

[1] MRI can be operated in various modes including diffusion imaging, T1 and T2 relaxation. Although imaging from projections is possible, in most cases the data are acquired in the frequency domain, which is reconstructed by inverse Fourier transformation.

$$p(\phi,t') = \int\limits_{-\infty}^{\infty} f_\phi(t',s)\,ds = \int\limits_{-\infty}^{\infty}\int\limits_{-\infty}^{\infty} f_\phi(t,s)\,\delta(t-t')\,dt\,ds =$$

$$= \int\limits_{-\infty}^{\infty}\int\limits_{-\infty}^{\infty} f(x,y)\,\delta(x\cos\phi + y\sin\phi - t')\,dx\,dy$$

(2)
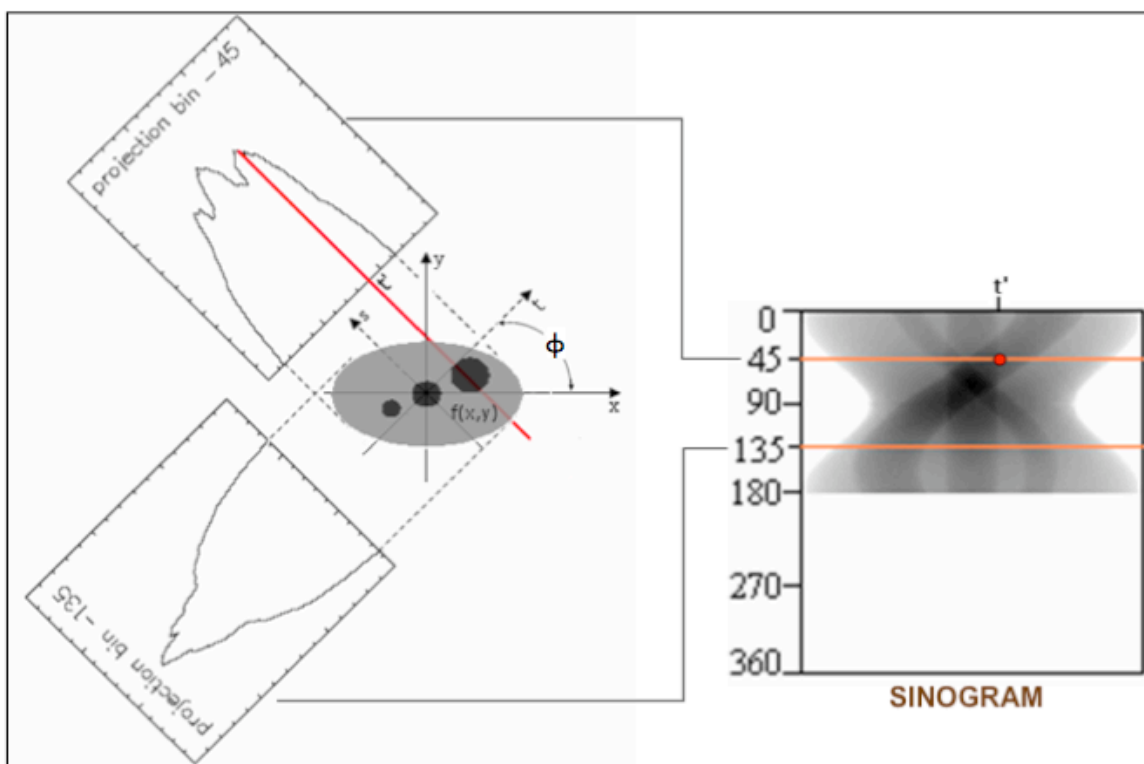
Figure 1 Examples of two projection bins (at angle 45° and 135°) obtained from an elliptical phantom: The three dark circles within the image f (x, y) represent higher values with respect to gray colored background values. A line integral of f (x, y) along the red line at t' and its corresponding pixel location in the sinogram is also shown.

The collection of these projection profiles forms the Radon transform[2], which is used to reconstruct the image through an analytical method, such as filtered backprojection (FBP) or an iterative approach. Both methods are based on the

---

[2] The projection data are often called sinogram because a point source traces out a sinusoidal path through the diagram.

backprojection of projection profiles where projection elements p(ϕ,t) at t, are integrated to produce image element b(x,y) as shown below:

$$b(x,y) = \int_0^\pi p(\phi,t)\,\mathrm{d}\phi \qquad (3)$$

The backprojection gives a blurred image of the actual object f (x, y). That is,

$$b(x,y) = f(x,y) * h(x,y) \qquad (4)$$

in which the object f (x, y) is convoluted by the point spread function h (x, y) = 1/r. Using the result of central section theorem[3] [18], this blurring can be eliminated either by deconvolving the projection files in the image space or by multiplying them with a ramp filter |k| in the 1-D spatial frequency domain. The backprojection is then applied, incorporating the modified projection files p^F in the integration to obtain the actual object, as shown below.

$$f(x,y) = \int_0^\pi p^F(\phi,t)\,\mathrm{d}\phi \qquad (5)$$

Although FBP accurately reconstructs the object in this noise-free mathematical model, in real applications the noisy nature of projections produces streak artifacts since ramp filter enhances these higher spatial frequencies.

Various iterative reconstruction methods [19] have been developed and are widely used in both clinical and research studies as an alternative to FBP. They are based on the iterative comparison of estimated and measured projections: The initial estimate is usually a mathematical projection (modeling the actual scanner acquisition) of a constant image (e.g., a uniform square). An "error projection" is obtained by the comparison (e.g., by dividing) of estimated and measured projections. This error projection is then

---

[3] 1-D Fourier transform of a projection at an angle theta is equivalent to the 2-D Fourier transform of the object evaluated along a radial profile at the same angle.

backprojected without using a filter to obtain an "error image", which is used to update (e.g., by multiplying) the previous estimate. As this process is repeated iteratively the estimated projection data approach to the measured projection data. The iteration is stopped when a certain predefined convergence criteria (e.g., number of iteration or an error threshold between the estimated and measured projections) is met. One advantage of iterative algorithms is that it is possible to incorporate the correction of various physical aspects of the imaging system. In addition, streak artifacts are largely eliminated when iterative algorithms are used [20]. These methods are computationally more demanding; however, today's computers and more efficient algorithms allow their use in clinical applications.

3D tomography is based on similar principles as explained above. These methods are implemented in both PET and SPECT. In the following sections, the instrumentation of emission tomography is reviewed, along with operational principles, major image degrading factors and their corrections.

Emission Tomography

Emission tomography (ET) is a well established, non-invasive functional imaging modality with many applications in a wide range of clinical and research areas such as oncology, cardiology, neurology, pharmacology, and others. The main objective of emission tomography is to obtain a volumetric image of radioactivity corresponding to the distribution of radiotracers (molecules labeled with unstable atoms, radionuclides) introduced into a subject to provide biologic information about the target of interest. While other volumetric imaging modalities such as magnetic resonance imaging (MRI) and x-ray computed tomography (CT) provide remarkable anatomical images, they are limited in their ability to provide functional information. Although MRI can provide functional images comparable to emission tomography [21, 22], its sensitivity limits measurements to the milimolar to molar (mol/liter) concentration range. In contrast,

emission tomography allows imaging between nanomolar and picomolar concentration ranges without altering any biological response because of the high specific activity of its radiotracers[4] [23, 24]. Availability of these different modalities offers complimentary imaging approaches and their combined use enhances diagnostic information.

Positron emission tomography (PET) and single photon emission computed tomography (SPECT) are two main modalities used in emission tomography. They both rely on the detection of high-energy photon emissions from radionuclides introduced into the object of interest (e.g., human, animal and phantoms). Arrays of gamma-detectors are placed or rotated around the object so that projections from many different angles are obtained. The collected projection data are then used to reconstruct images of selected planes within the object.

Because of the different decay modes of their radionuclides, SPECT and PET modalities differ in hardware (e.g., detectors and collimators), data acquisition and reconstruction software. The unique properties of these modalities render them advantageous for distinct applications. For clarity, the radionuclides employed and the operational principles of PET and SPECT are presented individually.

<u>PET Radionuclides</u>

The radionuclides can be employed in PET studies, ^{13}N, ^{11}C, and ^{15}O, are all biologically relevant elements, which enable the radiolabeling of a wide variety of organic molecules. These radiolabeled molecules are chemically equivalent to their stable ones, and follow the same metabolic path providing valuable information about biologic processes. The short half-life (1min-20min) of these radionuclides, however, necessitates a medical cyclotron on site. Moreover, the fast decay of ^{13}N (10 minutes) and ^{15}O (122 seconds) limits its labeling use to simple molecules.

---

[4] The ratio of radioactivity to the total mass of elements present in a radioactive sample.

Another approach in PET is to use analogs, which involves modifying the original compound and its biological role. For example, replacing the hydroxyl (OH) group on the second carbon in glucose with ^{18}F forms a glucose analog, fluorodeoxyglucose (FDG), which only undergoes the first step in the metabolic pathway of glucose, becoming trapped and accumulating in the cell in proportion to glucose metabolism [23]. Many disease conditions can be assessed using this information. For example, malignant cells reveal significantly higher-count density against the low-count density background of surrounding normal tissues, exhibiting abnormally increased glucose metabolism. ^{18}F-FDG is used for the majority of the clinical applications, because of this unique biological property and its relatively longer half-life (110 minutes), which allows its transportation to places without medical cyclotrons[5].

The instability of PET radionuclides comes from their excess number of protons relative to neutrons in the nucleus. In the decay process, a proton (p) in the nucleus is transformed into a neutron (n), and a positron (β^+) is emitted along with a neutrino (ν):

$$p \rightarrow n + \beta^+ + \nu + energy \tag{6}$$

The discrete transition energy of a particular radionuclide is shared between a neutrino and a positron in a continuous distribution of energies, with the positron receiving on average approximately of one-third the total energy [23].

Although PET radionuclides are referred to as "positron-emitters", decay through electron capture (EC) is also possible. With EC, an orbital electron is captured by the nucleus and combined with a proton to form a neutron. The excess energy appears in the form of characteristic x-rays, Auger electrons or γ-rays. Table-1 shows some of the properties of radionuclides commonly employed in PET studies. Among these, ^{18}F and

---

5 Another advantage of ^{18}F use comes from the low positron range, which provides higher image resolution compared to other PET radionuclides.

[82]Rb are routinely used in clinical studies and the remaining radionuclides are used primarily for research purposes.

PET Radionuclides	^{18}F	^{82}Rb	^{13}N	^{15}O	^{11}C
Compound	FDG, FLT	^{82}RbCl	^{13}NH$_3$, N^{13}N	H$_2$^{15}O, O^{15}O	^{11}C-acetate ^{11}CO, ^{11}CO$_2$
Examples of applications	FDG: Tumor diagnosis, staging, therapy follow up. FLT: tracking DNA proliferation	Myocardial perfusion	Cerebral and myocardial perfusion, pulmonary ventilation	Cerebral and myocardial perfusion, O$_2$ metabolism	Myocardial metabolism, blood flow
Production reactions	^{18}O(p,n)^{18}F ^{20}Ne(d,α)^{18}F	^{82}Sr-generator	^{16}O(p,α)^{13}N ^{13}C(p,n)^{13}N	^{14}N(d,n)^{15}O ^{15}N(p,n)^{15}O	^{14}N(p,α)^{11}C ^{10}B(d,n)^{11}C
Decay mode	β^+: 97% EC: 3%	β^+: 95% EC: 5%	β^+: ~100%	β^+: ~100%	β^+: ~100%
Half-life	110 min	78 s	9.96 min	122 s	20.4 min
Maximum positron energy (MeV)	0.63	3.35	1.19	1.72	0.96
Positron average range in water (mm)	0.64	4.29	1.32	2.01	1.03

Table 1 Radionuclides commonly used in PET imaging. Compounds based on ^{18}F are Fluorodeoxyglucose (FDG) and Fluoro-L-Thymidine (FLT). β^+ and EC stand for positron emission and electron capture decay modes, respectively [23, 25].

Basic Operation Principles of PET

After its emission, a positron travels a short distance (~1 mm average for 1 MeV in water), depending on its initial energy and the density of the medium, and eventually

combines with an electron forming a short-lived (~ 0.1 ns) state, called *positronium*[6] [26]. The total rest energy of the positronium, $2m_e c^2$, is converted into a pair of 511 keV annihilation photons, which are emitted nearly 180° apart from each other (with a 0.5° FWHM angular uncertainty due to the residual momentum of the positronium), preserving the approximately zero total momentum of the positronium. The images in PET rely on the coincidence detection of these annihilation photons within a predefined electronic window, called a coincidence-timing window (typically 4 − 12 ns depending on the detector material [23].

Coincidence detection gives valuable information, indicating the location of the annihilation event along the line between the two coincident detectors, also known as line of response (LOR[7]). This is also referred to as *electronic collimation* since emission of annihilation photons is naturally collinear without needing any physical collimator to restrict their direction. In contrast, systems using a physical collimator (e.g., SPECT) have fewer detected events for a given amount of radioactivity due to the absorption of photons by the physical collimator. For this reason, for a given detector surface area, PET systems are significantly more efficient (~100 times) than SPECT systems and provide less noisy imaging.

The accumulation of many such coincidence events creates approximate line-integrals through the radionuclide concentration, which then can be reconstructed to form

---

[6] Only the ground state positronium is observed with singlet and triplet states, called para-positronium (p-Ps) and ortho-positronium (o-Ps), respectively. Due to conservation laws (parity etc), p-Ps and o-Ps generate 2γ and 3γ photons. Although in vacuum the probability of each of these four spin configurations are equal, in tissue most of these o-Ps are converted to p-Ps giving rise to 2 annihilation photons. As a result, only 0.5% of the annihilation occurs in 3γ-mode, and thus PET imaging is based on solely on 2γ photons.

[7] To be more accurate, LOR is also called as volume of response (VOR) corresponding to the region between two detector surfaces.

images corresponding to the distributed radioactivity inside the tissues and organs. In reality, PET does not measure the actual location of the radionuclides where the positrons are emitted, but rather the location of an annihilation event, which occurs at a short distance from the radionuclide's position. This creates an inherent limit[8] in the spatial resolution of PET studies [27] . The impact on the resolution is more significant with increasing positron energies. In this respect also, ^{18}F is more advantageous than the other PET radionuclides since it has the lowest positron energy.

Coincidence Event Types

There are four types of coincidence events (counts) that can occur in PET: true, scatter, random (accidental) and multiple. These are shown in Figure 2 on a single PET detector ring. Among these, only the true event gives accurate information about the emission sources. The other three degrade the reconstructed image and their effects need correction. In the case of scatter coincidence, which is discussed in detail in the following section, the event is assigned to an incorrect LOR, as at least one of the annihilation photon deviates from its original emission direction after interacting with the surrounding material. In the random event case, photons from two independent annihilation events can be detected and registered within the same time window. These uncorrelated events do not carry any spatial information and produce undesired background in the final images

---

[8] The discrete width of detector elements, slight deviation from collinearity of annihilation photon pairs and the depth of interaction (DOI) are the other main spatial resolution limits in PET imaging.
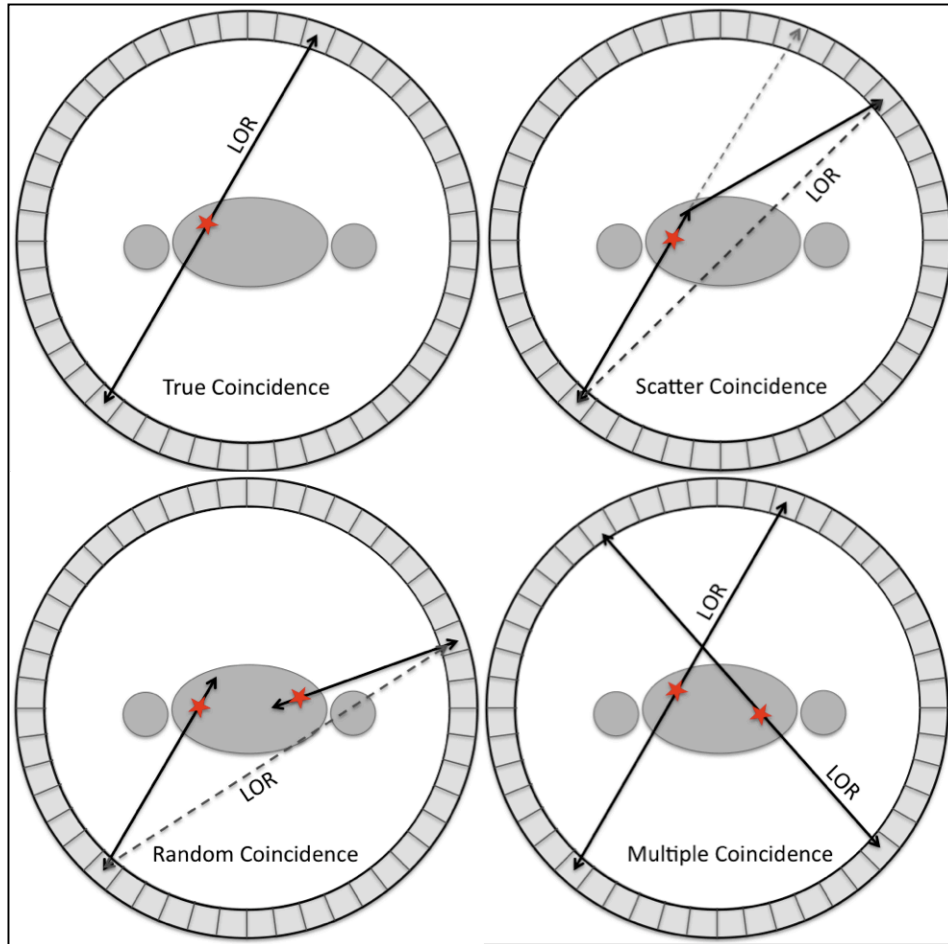
Figure 2 Coincident events in PET imaging shown on a single detector ring. In 3D-mode PET, similar events occur in oblique angles (i.e., between the detectors of different rings) as well.

[18]. The rate of these coincidences is proportional to the square of the activity in the field of view (FOV), and directly proportional to the coincidence time window (τ). For a given pair of detectors (i , j), the random rate (N_R) can be expressed as:

$$N_R = 2\,\tau\,N_i\,N_j \qquad\qquad (7)$$

where N_i and N_j are individual detection rates of the coincident detectors. Finally, multiple coincidences occur when two or more annihilation events are counted in the same coincidence window. In this case, it is not obvious whether the annihilation event is registered to the correct detector pairs. For example, in Figure 2, there are 6 possible

coincidences (only the correct ones shown) among 4 coincident detectors. Multiple coincidences are corrected by selecting the most probable detector pairs based on predefined rules.

SPECT radionuclides

Most of SPECT imaging is performed employing ^{99m}Tc (half-life of 6 hours), which is a decay product of ^{99}Mo (half-life of 67 hours). A device called ^{99}Mo - ^{99m}Tc generator is used to separate the daughter from the parent, where ^{99m}Tc is eluted with normal saline (0.9 % NaCl) [28]. Examples of ^{99m}Tc applications in areas such as cardiac, brain, bone and tumor imaging are briefly presented here:

Cardiac studies: Myocardial perfusion studies assess coronary artery disease and heart muscle damage following infarction. These studies are commonly performed under rest and stress (exercise or pharmacologically) conditions employing a ^{99m}Tc labeled agent[9] (sestamibi or tetrofosmin), which rapidly accumulates in cardiac cells in proportion to blood flow [23]. The stress images are used to identify regions of the heart that exhibit diminished perfusion, which is an indication of a disease. If these regions appear impaired in the stress images, yet normal during rest, then function may be restored [29].

Brain Studies: Cerebral perfusion studies assess cerebral blood flow by using ^{99m}Tc attached radiopharmaceuticals such as HMPAO (hexamethyl propyleneamine oxime) [30], which are able to cross the blood-brain barrier and distribute in the brain – presumably – in proportion to blood flow. This information can be used to diagnose cerebrovascular disease since blood flow abnormalities indicating ischemia (restriction in blood supply) or hyperemia (excess of blood flow) can be identified. In the early stages

---

[9] An alternative to this agent is ^{201}Tl, which is becoming increasingly important because of product shortage of ^{99}Mo due to outages at the main supply reactors.

of an acute stroke, SPECT perfusion studies are significantly more accurate in indicating abnormality than MRI and CT studies. Other applications of perfusion studies include diagnosing dementia, seizure disorders, brain tumors and psychiatric disease.

Bone Imaging: ^{99m}Tc-MDP (methylene diphosphonate) [31] scans are used to diagnose a variety of bone diseases. An abnormal bone scan exhibits foci having radiotracer uptakes that are above or below normal relative to neighboring bone. Higher focal uptake may indicate arthritis, a fracture or a metastasis, and lower focal uptake may indicate a necrotic tumor [32].

Tumor imaging: ^{99m}Tc-sestamibi (methoxy isobutyl isonitrile, MIBI) is used as a tumor imaging agent for parathyroid adenoma and breast cancer since often it shows accumulation in cancerous cells. Other radionuclides have been used to visualize both primary and metastatic lesions for various conditions including lung cancer, lymphomas, melanomas and brain tumors [33].

[99m]Tc radionuclides decay through isomeric transition (IT), where the decay of a metastable (isomeric) state results in the emission of discrete γ-rays. Other SPECT radionuclides decay through electron capture (EC), where an orbital electron is "captured" by the nucleus and combines with a proton to form a neutron, emitting a single γ-ray. The decay formula for EC:

$$p + e^- \rightarrow n + v + energy \tag{8}$$

In SPECT, γ-ray energies differ depending on the radionuclide used (e.g., ^{99m}Tc with 140 keV and ^{123}I with 159 keV photons) and the same radionuclide may emit photons with different energies (e.g., ^{67}Ga with 93, 185 and 300 keV photons). This allows simultaneous imaging of multiple radionuclides. In addition, SPECT radionuclides do not require a medical cyclotron on site since they typically have significantly longer half-lives. Their common applications and other general properties are summarized in Table 2.

SPECT Radio-nuclides	^{99m}Tc	^{123}I	^{111}In	^{201}Tl	^{125}I
Principal Photon Emission (keV)	140	159 (83%)	171 (89%) 245 (94%)	68-80 x-rays	27-30 x-rays 35 γ-rays
Production	^{99}Mo-generator	^{124}Te(p,2n)^{123}I	^{111}Cd(p,n)^{111}In ^{109}Ag(α,2n)^{111}In	^{201}Hg(d,2n)^{201}Tl	^{124}Xe(n,γ)^{125m}Xe →^{125}I
Decay Mode	IT	EC	EC	EC	EC
Half-Life	6.02 hr	13.22 hr	67.92 hr	73.2 hr	60 d

Table 2 Radionuclides commonly used in SPECT imaging. EC and IT stand for electron capture and isomeric transition decay modes, respectively [23, 25, 34].

Basic Operation Principles of SPECT

SPECT imaging is based on the external detection of γ-rays or x-rays emitted by internally distributed radiotracers in a subject. A typical clinical SPECT scanner is composed of one or more rotating gamma cameras to obtain multiple projections around the patient. The most popular scanners are based on two gamma cameras (dual-head) with a selectable variable angle between two cameras. In cardiac imaging, these cameras are positioned at right angles to each other and are rotated 90° (covering 180° of acquisition) to increase the sensitivity. In most other applications (e.g., brain perfusion studies), the cameras are opposed and are rotated 180° (covering 360° of acquisition) around the subject [32].

Unlike PET collinear annihilation photon pairs, most SPECT photons[10] [35] are emitted with no angular correlation. In order to constrain the direction of accepted photons, physical collimators (array of holes surrounded by thin lead walls) are placed in front of the detector faces to collect projections. There are four main collimator designs available: parallel-beam, fan-beam, cone-beam and pinhole collimators.

In most human SPECT scanners parallel-beam collimators (usually made of lead) are used. The parallel collimators are further classified depending on the photon emission energies and desired balance between spatial resolution and sensitivity. Fan-beam (converging) collimators are primarily used in brain imaging. In most small animal SPECT scanners single or multiple pinhole collimators (usually made of tungsten) are employed. Single pinhole versions provide increased spatial resolution (or magnification of image) reaching to sub-millimeter resolution for a reasonable efficiency when the source is distributed close to the aperture [20]. Cone-beam collimators do not have clinical applications in emission tomography.

Depending on the collimator choice, different data acquisition and reconstruction methods are applied. The principles of data acquisition and reconstruction from parallel beam data are explained in the tomography section. The same method can be used for fan-beam data if the projection files are sorted in parallel-ray data sets prior to reconstruction. Another alternative is to use a modified FBP algorithm, which incorporates fan-beam data. Reconstruction of cone-beam and pinhole based data is more complex. An approximate analytical method was developed by Feldkamp et al. [36] which directly reconstructed 3D cone-beam data reducing them to fan-beam data. However, in practice, iterative algorithms are employed for direct reconstruction of the 3D pinhole data [23].

---

10 Although ^{111}In emission photons have angular correction, this has not been successfully exploited.

As explained above, the use of collimators is essential in the operation of SPECT but not PET. This significantly decreases the sensitivity[11] and resolution of SPECT (~ sensitivity of 0.02% for two camera heads and resolution of ~10 mm) [20] as compared to PET (~0.6% and ~ 5 mm) [37] due to absorption of already limited counts of emitted photons.

Basic operation principles and radionuclides in emission tomography are presented above. To summarize, PET imaging generally offers better sensitivity and resolution than SPECT. However, PET applications cost is usually a significant concern due to cyclotron-produced radionuclides. PET and SPECT are preferred for different applications: SPECT predominately uses ^{99m}Tc and focuses on myocardial, bone and renal scans, whereas PET clinical studies are focused on tumor imaging employing ^{18}F-FDG and PET is an alternative to SPECT myocardial perfusion.

<u>Photon Interactions with Matter</u>

The majority of primary emission photons (γ-photons from SPECT radionuclides and PET annihilation photons) are either completely absorbed without reaching the detectors, or deviate from their original emission directions due to attenuating media (i.e. body, detector, shielding, etc.). This causes events to be either lost or misplaced, distorting the projection files and degrading the quantitative accuracy of images. The amount of image degradation is highly dependent on the nature and magnitude of the photon attenuation. It is therefore important to have a thorough understanding of photon interactions taking place in emission tomography and their impact on the images. In the range of nuclear medicine (~30-511 keV) emission photon interactions with matter occur in three different ways:

---

[11] Percentage of detected to emitted photons

i. Photoelectric effect: The incident photon is completely absorbed by an atom and its energy (hν) is transferred, usually to an inner shell electron (80% K-shell) [38], ejecting it from the atom with the energy,

$$T = h\nu - B_e \tag{9}$$

where B_e is the binding energy of the ejected electron (photo-electron). Consequently, an outer orbital electron occupies this vacancy, giving rise to either a characteristic X-ray or an Auger electron due to the binding energy differences between two electron shells.

The photoelectric absorption probability increases rapidly with lower incident photon energies (below ~0.1MeV) and higher atomic number, Z of a material (i.e., $\sim Z^3/E^3$) [23]. For PET annihilation photon energy (511 keV), the photoelectric effect is insignificant in tissue, but contributes to more than 50% of the interactions within the scintillation detectors (e.g., BGO and LSO). The effect in tissue becomes more significant for low-energy SPECT imaging (e.g., ^{125}I, emitting γ-rays and characteristic x-rays at ~30 keV) and x-ray CT imaging (~70 keV).

From an imaging standpoint, the absorption of photons results in event losses, particularly from locations deeper in the body. This contributes to the image noise and non-linear representations of the radioactivity distribution.

ii. Compton (incoherent) Scattering: In this process, the photon imparts some of its energy to an electron (typically loosely bound in the outer shell) and deviates from its original direction. Compton scattering is the dominant interaction in the body, particularly for higher energy photons. For example, Compton interactions in water form over 99.7% and 97.4% of the total attenuation coefficients at 511 and 140 keV, respectively.

The conservation of momentum and energy impose a simple relationship (Compton equation), between the scattering angle (θ) and the photon energies before (E_i) and after (E_s) scattering:

$$E_s = \frac{m_e c^2}{1 - \cos\theta + \frac{E_i}{m_e c^2}} \tag{10}$$

where $m_e c^2$ is the rest energy of the electron (511 keV). For annihilation photons, the equation reduces to,

$$E_s = \frac{511 \text{ keV}}{2 - \cos\theta} \tag{11}$$

Another useful relation is the Klein-Nishina equation, which gives the probability of a Compton interaction (in terms of differential scattering cross section, dσ/dΩ) of a photon with incident energy (E_i) and scatter angle θ,

$$\frac{d\sigma}{d\Omega} = \frac{r_e^2}{2}(1 + \cos^2\theta)\left[\frac{1}{1 + \alpha(1 - \cos\theta)}\right]^2 \left[1 + \frac{\alpha^2(1 - \cos\theta)^2}{[1 + \alpha(1 - \cos\theta)](1 + \cos^2\theta)}\right] \tag{12}$$

where r_e is the classical electron radius and $\alpha = E_i / m_e c^2$. For the annihilation photons of PET, the equation takes a simpler form [9].

$$\frac{d\sigma}{d\Omega} = \frac{r_e^2}{2}\left[\frac{1}{2 - \cos\theta)^2}\right]\left[1 + \cos^2\theta + \frac{(1 - \cos\theta)^2}{2 - \cos\theta}\right] \tag{13}$$

Klein-Nishina distribution, plotted in Figure 3, implies that for higher energy photons forward scattering (small angle scattering) is favored, and thus for these energies the spatial information of the images is less distorted. In addition, Figure 4 shows the dominant photon interactions in body and common scintillation materials used in PET and SPECT imaging.
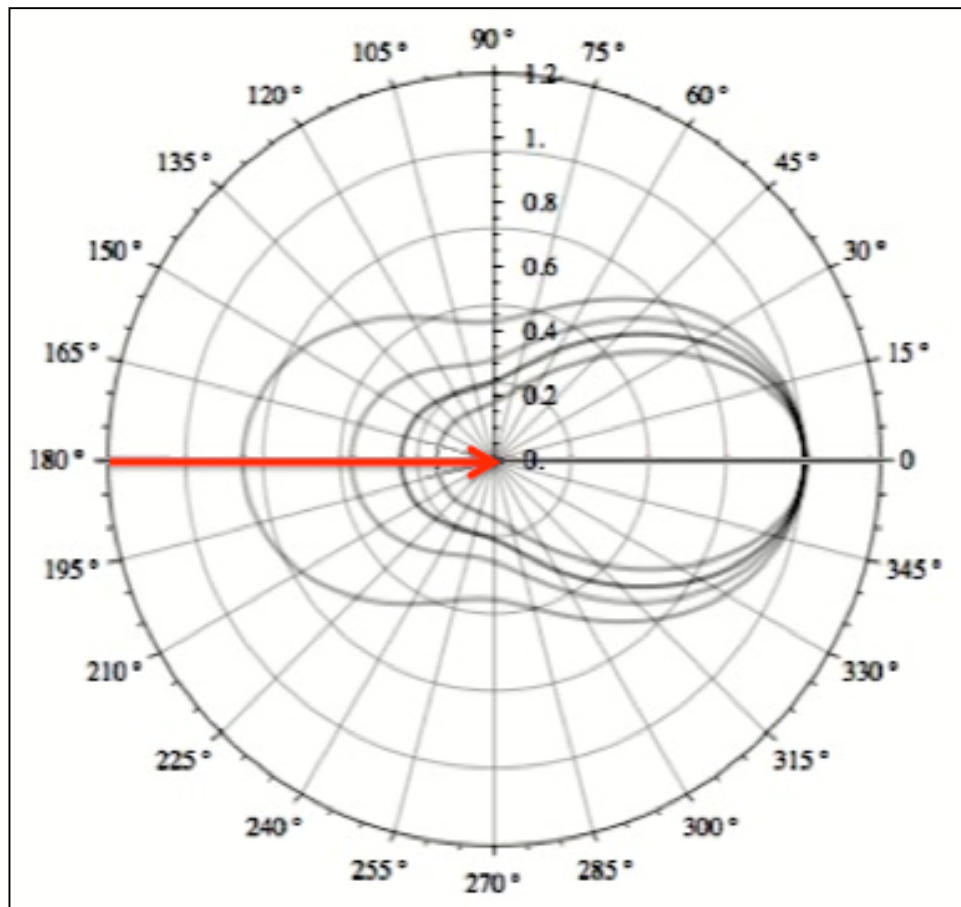
Figure 3 Klein-Nishina probability distributions plotted[12] for different PET (511 keV) and SPECT energies: 245, 140 and 30 keV from inner to outer contour. The red arrow indicates the direction of incident photon interacting with an electron at the center of the diagram.

---

[12] http://demonstrations.wolfram.com/KleinNishinaFormulaForPhotonElectronScattering/
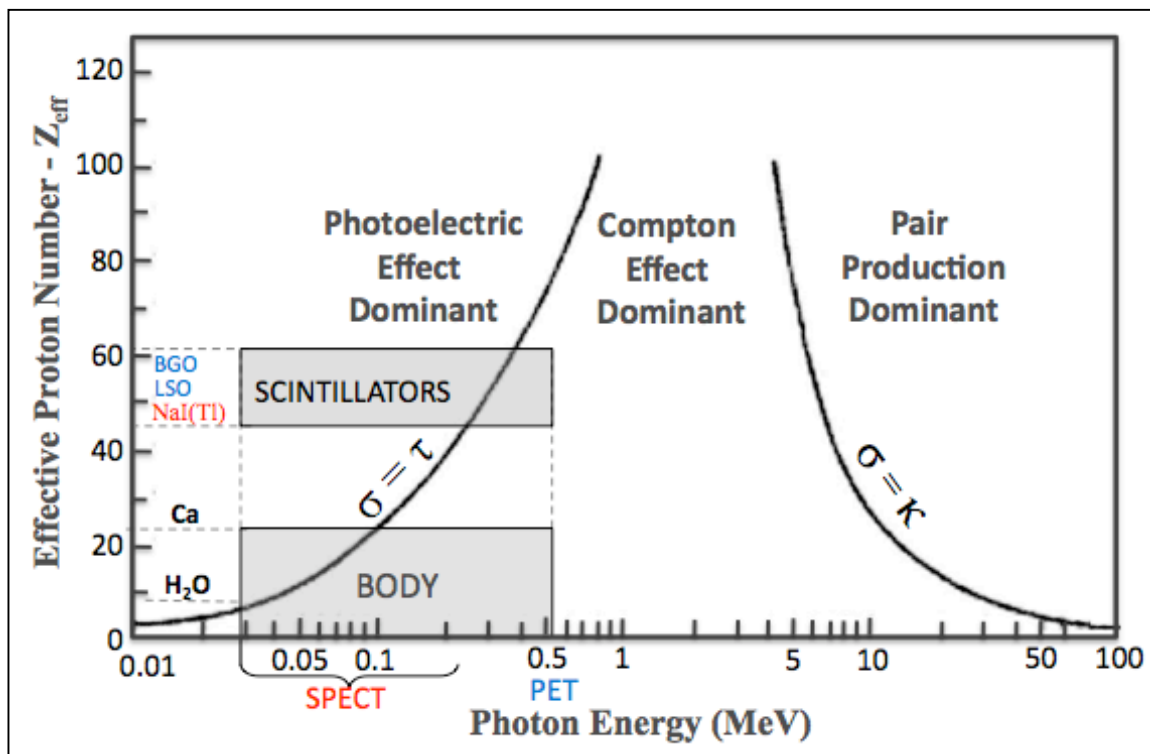
Figure 4 Dominant interactions depending on Z (atomic number) and incident photon energies are shown, where τ, σ and κ represent attenuation contributions from photoelectric effect, Compton effect and pair production, respectively. Compton effect is the dominant interaction in nuclear tomography, as most of the biological structures have low Z (i.e. water Z_{eff} ~7.9) and photon energies typically are in the range of 30 keV–511 keV. Although pair production is included here, in diagnostic nuclear medicine photon energies never reach the minimum energy required (1022 keV) for pair production.

iii. Rayleigh (coherent) Scattering: Photons interact with the entire atom without imparting their energy. Although it is not possible to eliminate coherently scattered counts by energy-based discrimination, Rayleigh scattering has a very low probability of occurrence at photon energy levels and low Z materials (e.g., tissue) encountered in emission tomography. Moreover, the scatter angle is typically small. Therefore, its effect on images is negligible compared to the impact from the Compton scatter.

Because of these interactions, the intensity of an incident photon beam, I_o, decreases exponentially as it travels in the attenuation medium. Assuming "good

geometry" (or narrow beam) condition (i.e., photons are mono-energetic and excluded from the counts as soon as they undergo an interaction) [39], this can be described with a simple equation:

$$I(x) = I_o \exp(-\mu x) \qquad (14)$$

where the exponential term describes the probability of total attenuation, I(x) represents the intensity of the transmitted photon beam after traveling x-thickness in the material and μ is the total linear attenuation coefficient:

$$\mu = \mu_{Photoelectric} + \mu_{Compton} + \mu_{Rayleigh.} \qquad (15)$$

That is, the total attenuation probability is equal to the product of individual interaction probabilities. The probability of each interaction and its contribution to the total attenuation coefficient depends on the photon energy, material density and the atomic number (Z)[13]. Table 3 shows the mass (μ/ρ) and linear (μ) attenuation coefficient values obtained from XCOM photon cross section library from the National Institute of Standard and Technology (NIST) [40, 41] for various photon emission energies and attenuating media encountered in emission tomography. These values are plotted for the energy range of 10-1000 keV in Figure 5 through 9.

---

[13] A more fundamental value is the mass attenuation coefficient, which is directly related to the cross sections per atom and is independent of the actual density and the physical state (gas, liquid, or solid) of the absorber. For Compton interaction, in particular, the mass attenuation coefficient is nearly independent of Z for all elements except hydrogen.

Material	Radio-nuclide	Photon Energy (keV)	Scattering attenuation coefficient		Photoelectric attenuation coefficient	Total Attenuation coefficient	
			Rayleigh	Compton		cm²/g	cm⁻¹
WATER $Z_{eff}=7.89$ $\rho=1$ g/cm³	¹²⁵I	27.5	0.054	0.182	0.194	0.430	
	⁹⁹ᵐTc	140	0.003	0.150	0.000	0.154	
	PET	511	0.000	0.096	0.000	0.096	
LEAD $Z_{eff}=82$ $\rho=11.35$ g/cm³	¹²⁵I	27.5	1.550	0.079	36.3	37.9	393
	⁹⁹ᵐTc	140	0.119	0.096	2.18	2.39	27.1
	PET	511	0.011	0.067	0.078	0.156	1.77
NaI(Tl) $Z_{eff}=50$ $\rho=3.67$ g/cm³	¹²⁵I	27.5	0.473	0.122	5.24	5.84	21.4
	⁹⁹ᵐTc	140	0.032	0.117	0.332	0.481	1.76
	PET	511	0.003	0.077	0.009	0.089	0.33
BGO $(Bi_4Ge_3O_{12})$ $Z_{eff}=74$ $\rho=7.13$ g/cm³	¹²⁵I	27.5	0.439	0.136	0.108	11.4	81.3
	⁹⁹ᵐTc	140	0.032	0.124	0.497	0.652	4.65
	PET	511	0.003	0.081	0.018	0.101	0.72
LSO (Lu_2SiO_5) $Z_{eff}=66$ $\rho=7.4$ g/cm³	¹²⁵I	27.5	0.376	0.140	6.34	6.85	50.7
	⁹⁹ᵐTc	140	0.027	0.126	0.379	0.532	3.93
	PET	511	0.002	0.082	0.012	0.096	0.71

Table 3   Individual attenuation contributions and total attenuation coefficients (mass and linear) for various materials and energy levels. Water constitutes the majority of the body material and most tissue attenuation is near to that of water. Lead is usually used in shielding. NaI(Tl) is a common SPECT scintillator crystal used in detectors. BGO and LSO are commonly used scintillator material used in PET detectors. The values smaller than 10^{-3} are neglected.
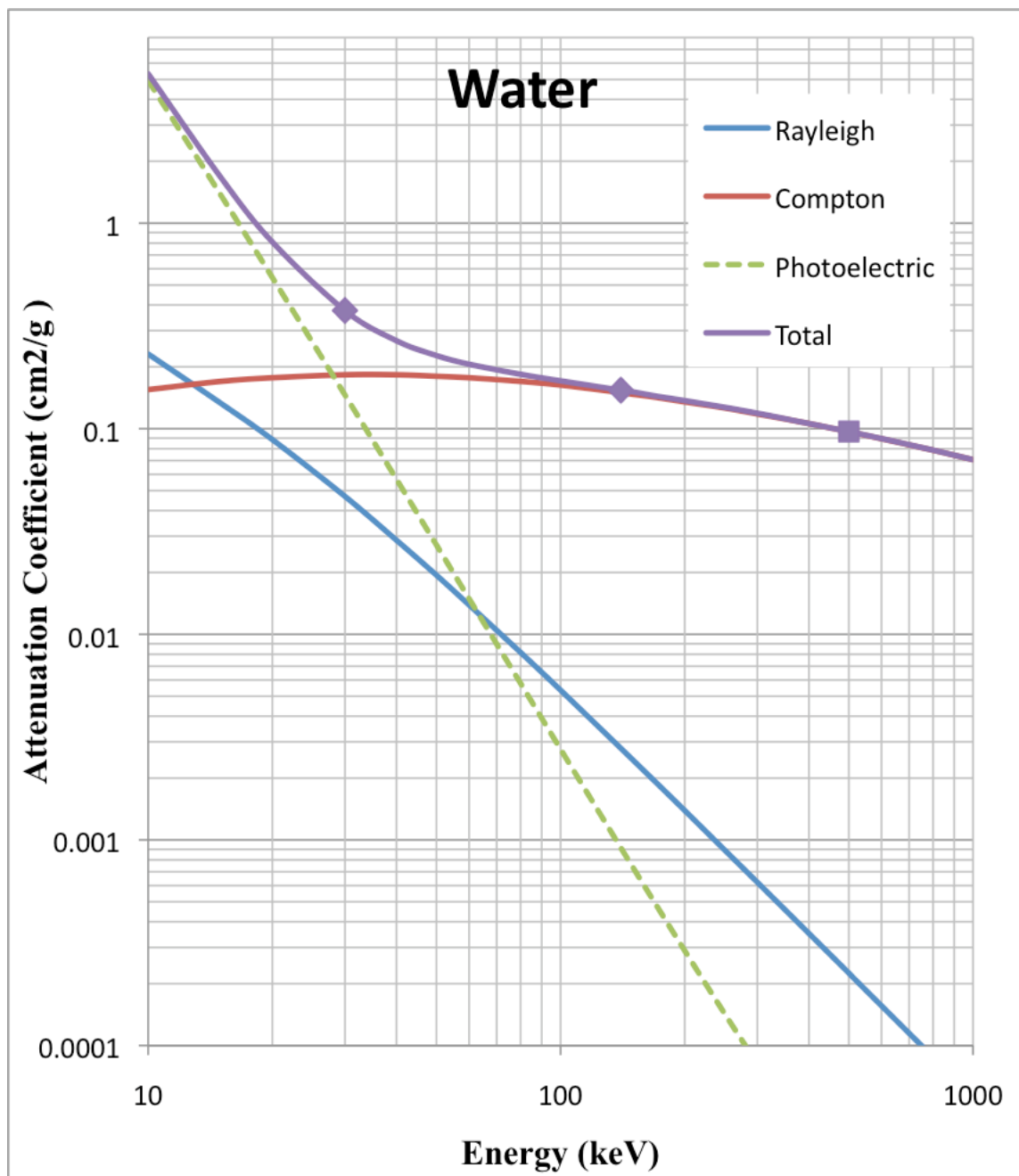
Figure 5 Individual contributions from different attenuation factors to the total attenuation coefficient shown for a range of incident photon energies (10- 1000 keV) in water. Example data points for SPECT (30 and 140 keV) and PET (511 keV) emission energies are marked on the total mass attenuation coefficients plot. In water, at energies above ~100 keV the contribution from Rayleigh scatter and photoelectric effects are negligible.
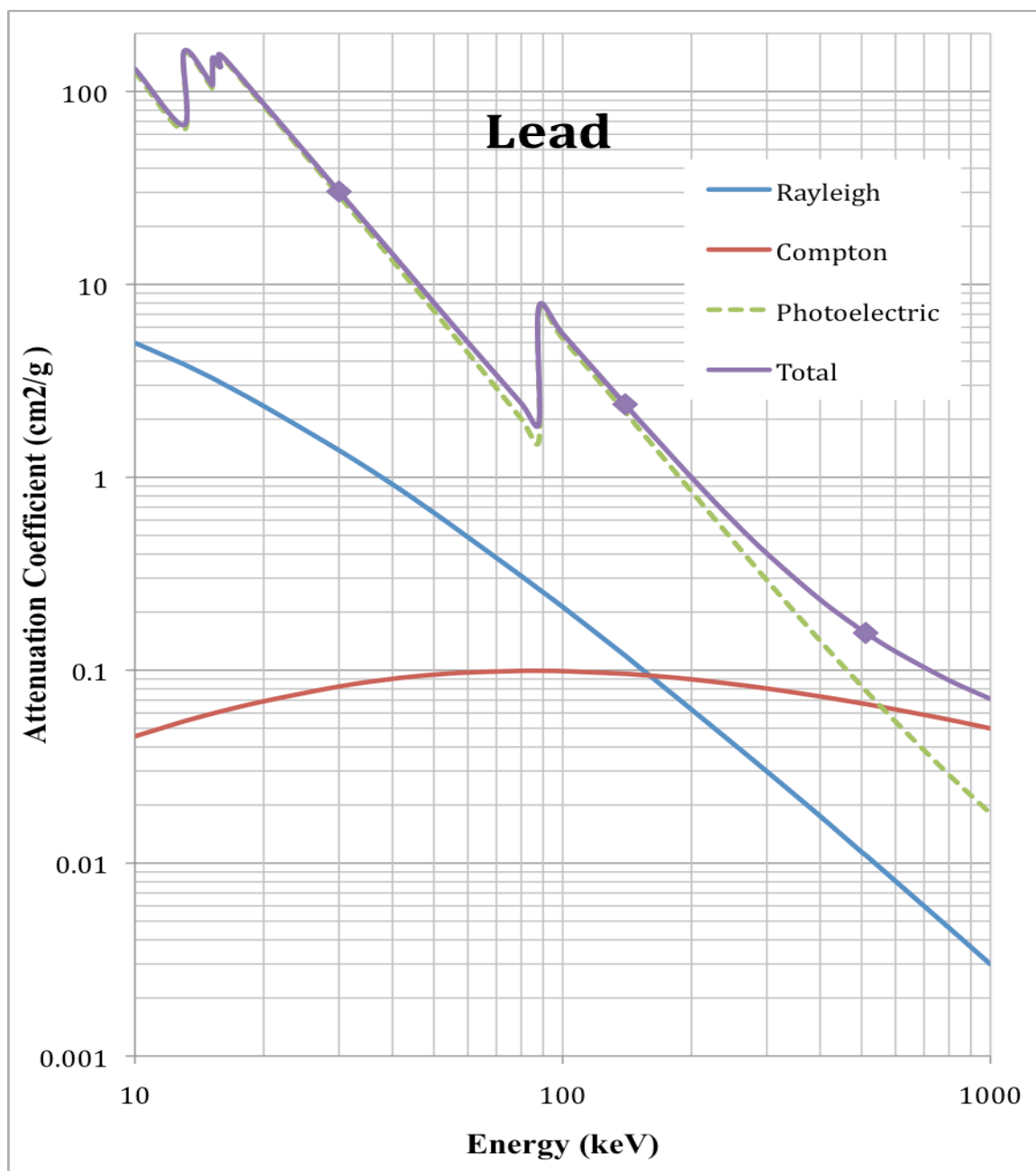
Figure 6 Individual contributions from different attenuation factors to the total attenuation coefficient shown for a range of incident photon energies (10-1000 keV) in lead. Example data points for SPECT (30 and 140 keV) and PET (511 keV) emission energies are marked on the total mass attenuation coefficients plot.
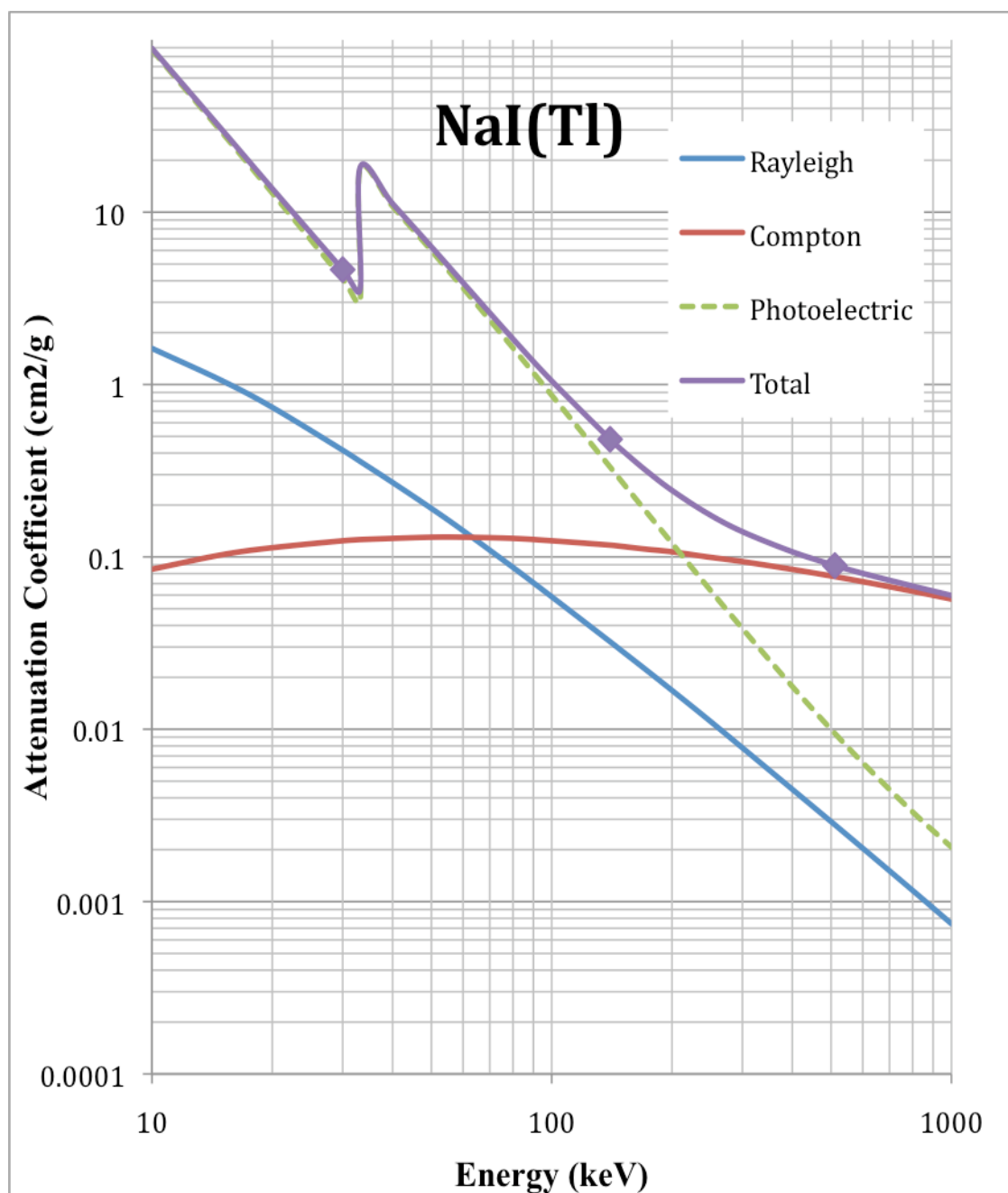
Figure 7 Individual contributions from different attenuation factors to the total attenuation coefficient shown for a range of incident photon energies (10- 1000 keV) in NaI(Tl) crystal used in SPECT detectors. Example data points for SPECT (30 and 140 keV) and PET (511 keV) emission energies are marked on the total mass attenuation coefficients plot.
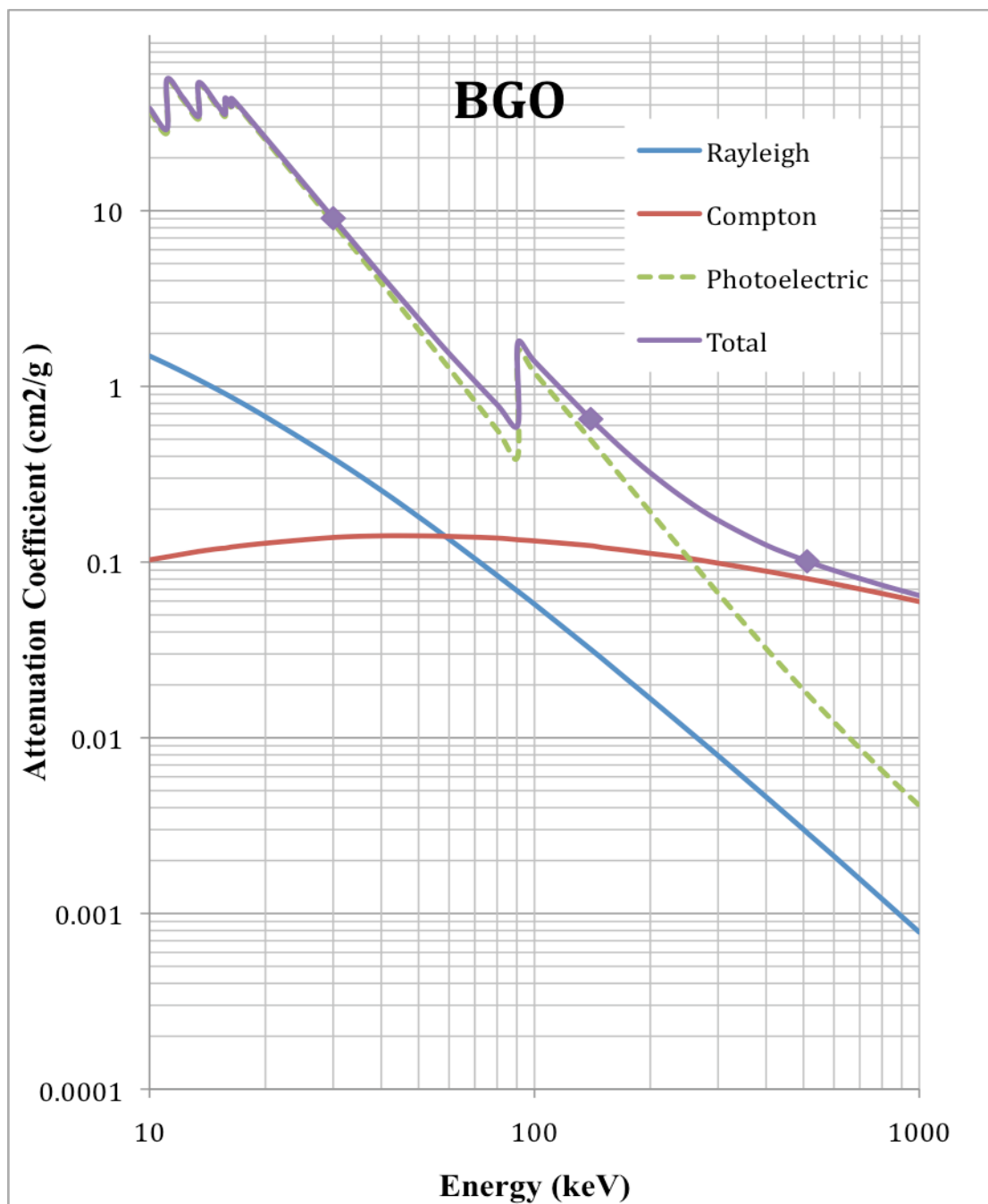
Figure 8 Individual contributions from different attenuation factors to the total attenuation coefficient shown for a range of incident photon energies (10-1000 keV) in BGO crystal used in PET detectors.. Example data points for SPECT (30 and 140 keV) and PET (511 keV) emission energies are marked on the total mass attenuation coefficients plot.
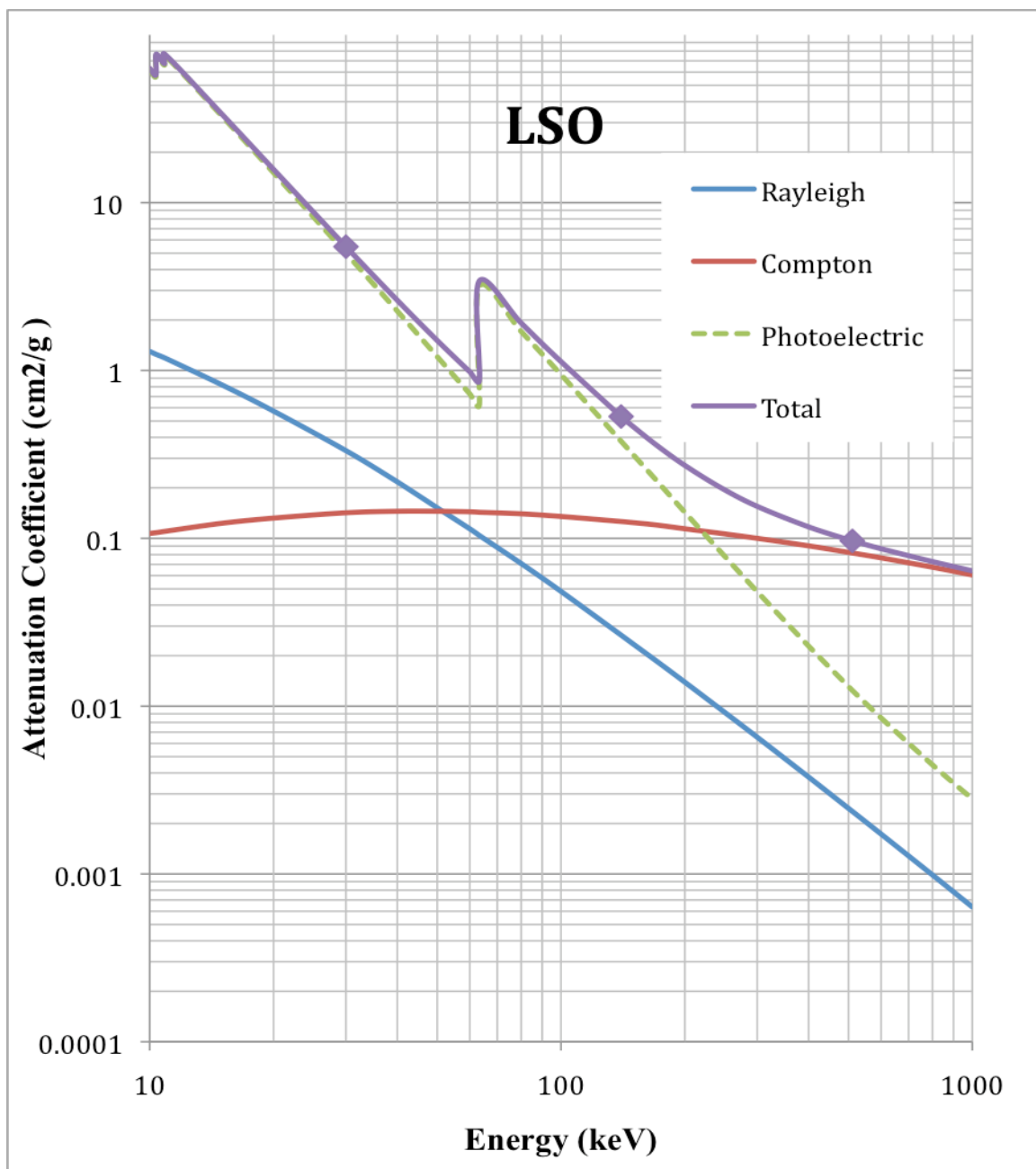
Figure 9   Individual contributions from different attenuation factors to the total attenuation coefficient shown for a range of incident photon energies (10- 1000 keV) in BGO crystal used in PET detectors. Example data points for SPECT (30 and 140 keV) and PET (511 keV) emission energies are marked on the total mass attenuation coefficients plot.

Various correction methods have been developed to compensate for the effects of photon interactions. These are classified separately as attenuation correction and scatter

correction, although scattering is really part of the attenuation phenomena: Attenuation in emission tomography refers to count losses (through absorption or scatter) from a line integral. The goal of attenuation correction, then, is to recover these lost events. Scatter, on the other hand, occurs when an event is removed from its original line integral and detected as an additional count in a different LOR. The goal of the scatter correction, then, is to remove these additional false events (scatter counts) from LORs. In the following sections, various attenuation and scatter correction methods are presented.

<u>Attenuation Correction</u>

The model that describes data acquisition in the absence of physical effects was previously shown in (1) and (2). With the addition of attenuation phenomena, SPECT and PET data acquisition models require different modifications on the line integral equation. Assuming the narrow-beam condition, PET and SPECT data acquisitions can be modified with the inclusion of the local attenuation coefficient μ(t, s), as follows, where the integral boundaries for PET (denoted as "LOR") include the full length of the LOR and for SPECT (denoted as "lor") is located between a point "s" and the detection point along the LOR.

PET:
$$p(\phi,t) = \int_{LOR(s,\phi)} f_\phi(t,s)\, ds \times \exp\left(-\int_{LOR(s',\phi)} \mu(t,s')\, ds'\right) \qquad (16)$$

SPECT:
$$p(\phi,t) = \int_{lor(s,\phi)} f_\phi(t,s)\, \exp\left(-\int_{lor(s',\phi)} \mu(t,s')\, ds'\right) ds \qquad (17)$$

In SPECT, the magnitude of attenuation depends on the thickness and type of the material photons meet along their path between emission and detection points. Hence, in full 360° SPECT imaging, two directly opposing detectors – generally – acquire different amount of counts. The dataset from opposing views are combined into a single dataset

forming approximate projection files of a 180° scan. On the other hand, the attenuation in PET is independent of the emission location, as the total pathlength traveled by annihilation photons is constant for a given LOR. This also means the attenuation effect is large in PET (maximum attenuation for each LOR). However, because of these constant factors, attenuation can be simply corrected by multiplying each line integral with the reciprocal of the exponential function in equation 16, provided the attenuation map $\mu(t, s)$ is known or estimated with sufficient accuracy. In contrast, in SPECT the exponential function is embedded in the integral and an analytical correction is not possible even if the attenuation map is known.

Attenuation correction is particularly important for larger objects since the probability of interaction increases with the thickness of the material as the photons transverse the body. In a typical clinical emission tomography study, attenuation effect is taken into consideration and appropriate corrections are applied in order to improve the accuracy of the reconstructed image. Attenuation correction methods are divided into two broad classes: transmission-based and transmissionless [42]. The common goal of these methods is to incorporate the anatomical information of the object, given by the attenuation coefficients, into the reconstruction algorithm in order to recover the information lost from attenuated photons.

In transmission-based corrections, an external source is used to obtain the attenuation map for attenuation correction. One approach for this method is to employ external γ-ray emitting sources that can be rotated around the object, creating transmission projection images at each angle of the emission scan. Transmission scans can be performed before, during (simultaneous) and after the emission scan. While non-simultaneous data acquisition increases the scan time (~2-10 minutes for bed position) [43] and creates registration problems due to subject motion, simultaneous acquisition introduces errors due to the cross-talk in the same bed position between the transmission and emission data. In addition, the low activity of the transmission source and low count

sensitivity of scintillation detectors limit the accuracy of the attenuation map acquired with this method.

Often, x-ray CT transmission data is employed to obtain attenuation maps with enhanced quality, as CT scans, due to their high count rates (~10^4 times higher than nuclear emission scans), reveal noise free and high resolution anatomical information. However, a separate CT scan is time consuming and requires extra effort from both personnel and the subject. In addition, maintaining the exact same subject position between CT and PET scans is difficult at best, negatively affecting the quality of coregistered images. While combined PET/CT and SPECT/CT scanners facilitate the scanning process, coregistration is still problematic (e.g., due to the organ motion) since emission and transmission data acquisition procedures continue to be temporally separated. In addition, combined scanners are expensive and not all tomography facilities posses them. Other challenges of this method must also be addressed, such as: beam hardening [44] effect due to multienergetic x-rays (as the photon beam travels in the object, the lower energy photon components are attenuated more, and the average photon energy of the beam progressively increases); scaling attenuation coefficients to the emission of photon interest (e.g., CT x-rays are in 80 keV range whereas PET annihilation photons are 511 keV); the requirement of specialized technologists trained in both nuclear medicine and x-ray tomography; and the additional radiation dose from CT scan.

A recent approach is to use PET/MRI [45] or SPECT/MRI [46] systems. MRI provides anatomical images without introducing any radiation dose, however, these data do not carry information about attenuation. Atlas methods are limited in their ability to correct for attenuation, because the material density of areas such as lungs changes dramatically both regionally and between subjects.

In addition to these transmission-based attenuation corrections, transmissionless methods are also available [47]. The most practical transmissionless method is to assume

uniform attenuation coefficients and apply these for the attenuation correction, provided the body contour could be determined by emission data [48, 49]. Although this approximation works well in relatively homogenous areas such as the brain and abdomen, it leads to large errors in imaging areas such as the chest due to the high variability of tissue density (up to 30%) in such regions [50]. Nevertheless, these correction methods might be convenient to use for smaller objects such as mouse or rat since the magnitude of attenuation is significantly low.

<div align="center">Scatter Correction</div>

Scatter is part of the attenuation phenomena, wherein photons deviate from their original directions and contribute to inappropriate LORs[14]. This results in false counts. The goal of the scatter correction is the removal of these false counts. The removal of scatter approximates a narrow beam geometry, which is the condition assumed for the attenuation correction. Therefore, it is important that scatter correction should be performed before correcting for attenuation.

The magnitude of scatter and the level of correction needed strongly depend on the size of the object and the mode of acquisition[15] (2D or 3D operation) [51]. For example, in 2D-mode PET the scatter is either compensated by using approximate methods based on the existing emission data or ignored altogether as the magnitude of the scatter fraction (SF) is within an acceptable range (10-20%) [52]. In clinical emission tomography, however, the impact of photon interaction is significantly larger (30-50% for SPECT and 40-60% for 3D-PET) [53]. For clinical PET studies, attenuation and sophisticated scatter correction methods are often required along with x-ray CT or

---

[14] Some of the scatter photons escape from the gantry without being detected resulting in count losses.

[15] In 2D acquisition, the detection of photons is physically and electronically restricted to a single plane (or including adjacent planes). 3D-mode utilizes oblique angle detection in addition to the direct planes of 2D mode. A few scanners can operate selectively in 2D or 3D mode using retractable septa.

radionuclide transmission scans. Although most small animal emission tomography is performed in 3D mode, the scatter fractions reported for mouse and rat studies are significantly low (5% - 25%) [54, 55] and an additional transmission scan may not be necessary (as in the case of 2D-PET).

A scatter event can be distinguished from a true event only on the basis of the energy. However, this is not very effective due to the insufficient energy resolution of the detectors (e.g., 20% BGO used in PET and 10% NaI(Tl) used in SPECT). In addition, a significant portion of the annihilation photons deposits only part of their energy within the detector. In a typical clinical PET scanner, a 350-650 keV acceptance window is set for primary 511 keV photons in which scattered photons up 57° counted as true events. The acceptance energy window setting is narrower in SPECT (e.g., 126-154 keV for 140 keV primary photons of Tc-99m) due to better energy resolution of the NaI(Tl) detector. Scatter events in PET and SPECT illustrated in Figure 10.

Many scatter correction methods have been developed to compensate for the scatter effect While their implementations and effectiveness differ, the common goal of all these approaches is the estimation and removal of the scatter from the recorded events. Some of the broad scatter correction approaches in emission tomography are presented here. Among these, the first three approaches do not require transmission scans and are considered simpler approaches. The last two, are sophisticated methods that employ an additional transmission scan.
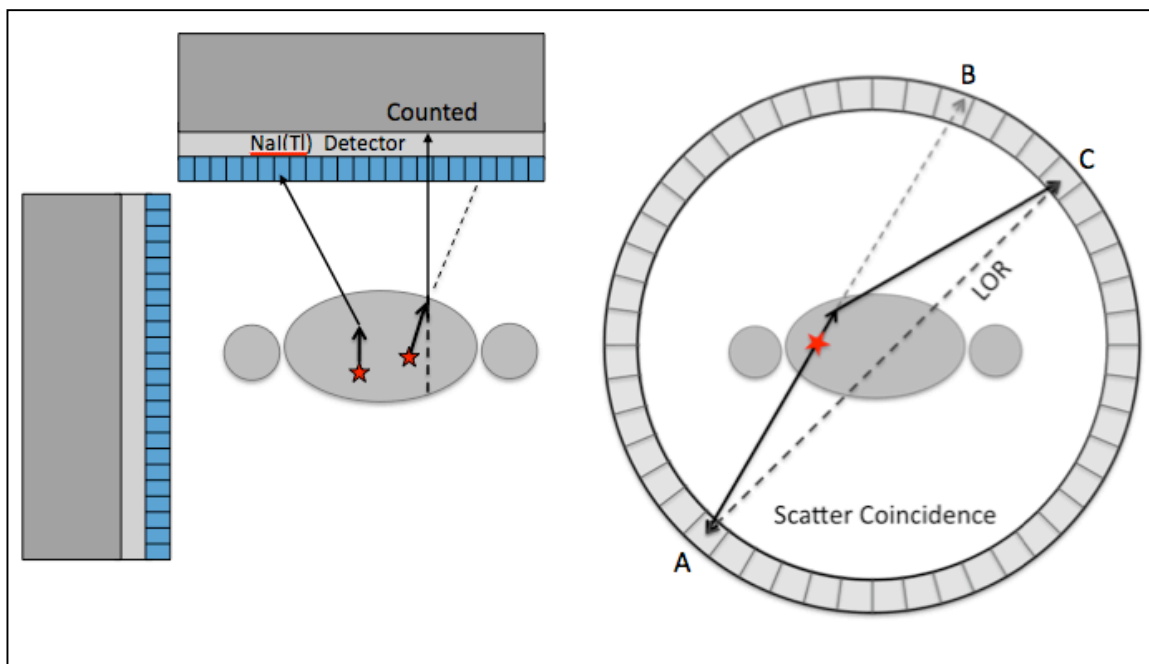
Figure 10 Cross sectional views of a dual-head SPECT scanner with parallel collimators (blue) and a PET scanner. Emission photons are scattered in the body and counted as if they had originated from different locations. In the SPECT example, the scattered photon on the left is absorbed in the collimator without being detected and the photon on the right is counted. In the PET example, the detection of the scattered photon at detector C causes the coincidence count be recorded between the detectors A and C instead of A and B.

Energy-Window (Spectral Analysis) Based Methods:

Energy-window method is commonly used in clinical SPECT practices. Among many different energy-window based scatter correction approaches in SPECT [56], the simplest implementation is the Dual Energy Window (DEW), In this method γ-rays are acquired with a photopeak and a lower-energy scatter window. For example, the photopeak window of ^{99m}Tc is usually set to 126-154 keV (20% spectral window centered on 140 keV) and the scatter window to 92-125 keV. The projection profiles obtained in scatter window is multiplied with an experimentally defined weight factor, and subtracted from the photopeak projection files to obtain unscattered projection data [4]. Another member of this category is the triple-energy-window, which employs two narrow sub-windows on both sides of the photopeak window. The scattered photons in

the photopeak window are estimated by these two sub-windows and then subtracted from the photopeak window as in the DEW method [57]. The equation (18) shows the calculation of scattered photons, which form a trapezoidal region, where W and W_s are photopeak window and sub-window widths; C_L and C_R are counts (ideally, scatter counts only) on the left and right sub-windows, respectively.

$$C_{scat} \cong \left(\frac{C_L}{W_s} + \frac{C_R}{W_s} \right) \cdot \frac{W}{2} \tag{18}$$

Energy-window based methods are far less successful in PET than in SPECT. Predominant Compton interactions taking place in PET scintillators makes it impossible to distinguish whether a photon scattered in the body or in the detector. The main drawback of these methods is that scatter estimates are derived from auxiliary windows, which provide limited count, thereby increasing the noise further when the scatter is subtracted from total count distribution.

Convolution/Deconvolution approaches:

These correction methods were originally applied to SPECT and 2D PET. Later, the method was adapted to 3D PET scatter corrections as well. Unlike the energy-window methods, the scatter is estimated by using the photopeak window only. This eliminates the additional noise introduced by the use of auxiliary windows.

The convolution-based approach assumes that the scatter counts can be estimated by iteratively convolving unscattered events with an exponential kernel (scatter response function), κ [58], and subtracting from the observed projection (P_o) as shown in equation

$$P_u^{(n)} = P_o - k\left(P_u^{(n-1)} \otimes \kappa \right) \tag{19}$$

where $P_u^{(n)}$ is the unscattered projection of nth iteration. Since $P_u^{(0)}$ is not known a priori, as a first approximation it is taken equal to C_o. Both parameters κ (scatter response

function) and k (scatter fraction) are obtained experimentally. In this model, the value of κ decreases exponentially as the radial distance from the source increases. That is, $\kappa\,(r) = e^{-\alpha\,r}$. On the other hand, the scatter fraction is calculated from:

$$k = \left(P_{water} - P_{air}\right)/P_{water} \tag{20}$$

where the P_{air} and P_{water}, represent the sinograms of a needle type [68]Ge (positron emitter) source obtained in air (scatter is negligible) and in a cylindrical water phantom, respectively.

The deconvolution method is also based on the assumption that scatter projection (S) could be represented as the convolution of unscattered projection (U). Hence,

$$T = U + S = U + U \otimes \kappa = U \otimes \left(\delta + \kappa\right) \tag{21}$$

where T is the total projection and δ is the Dirac delta function. Taking Fourier Transform (the operator is denoted with Γ) of the equation (7) and rearranging the terms, the unscattered projection can be obtained as follows [59]:

$$U = \Gamma^{-1}\left[\frac{\Gamma[T]}{\Gamma[\delta + \kappa]}\right] \tag{22}$$

Projection profile examination immediately outside the body

This method is used only for PET scatter correction. An event detected outside the body can be related either to random or scatter coincidence. After random coincidences are corrected, data from the tails (outside the object boundary) of the projection profiles is fitted with a smoothly varying function, such as a second order polynomial [60] or Gaussian [61]. This function then is interpolated to estimate the scatter distribution inside the object. The method relies on the assumption that scatter is a low-frequency

phenomenon and relatively insensitive to the radioactivity distribution. In fact, it represents a reasonable approximation in a large variety of conditions, including the case of a highly asymmetric source distribution in the object [62]. The accuracy of the method depends on the proper choice of starting points for the fitting function and the number of points used.

This method has several advantages over other approaches. The fact that it does not use an auxiliary window and does not require transmission data simplifies the procedure and reduces the demand for large computer resources. Moreover, it takes into account the scatter arising from outside the detection area. Finally, the information of scatter outside the field of view can be employed to further refine the sophisticated approaches.

<div align="center">Simulation based Correction Algorithms:</div>

Scatter correction methods presented thus far are useful in estimating and removing the scatter component; however, they are rather elementary approaches. More sophisticated approaches have been developed that incorporate in their algorithm physics of photon interactions in matter, thus estimating the scatter contribution with higher accuracy. These methods require an accurate attenuation map (through CT x-ray or external radionuclide scan) and an initial estimate of the reconstructed emission data. The latter can be obtained through simpler scatter correction methods or by employing direct plane data only [63]. Simulation corrected approaches can be divided into analytical and numerical (e.g., Monte Carlo) methods.

Analytical Simulation Based Scatter Correction:

This method requires both emission and transmission scans and it is commonly used for PET clinical imaging in the 3D mode. This technique is based on the assumption that single scatter forms the majority of the total scatter (~75% of the detected scattered

events) and that multiple scatter components can be approximated from the integral transformation of the single-scatter distribution [64-66] The single scatter coincidence rate between coincident detectors pairs is calculated incorporating the Klein-Nishina distribution and various scanner properties (e.g., energy resolution, geometry, and energy window settings). The multiple-scatter distribution (S_M) is estimated by the convolution of single-scatter function with a Gaussian kernel κ, as shown in equation (23).

$$S_M(r,\theta,z) = \int_{-\infty}^{\infty} S_S(r-u,\theta,z)\kappa(u;\theta)du \tag{23}$$

Here, the coordinate z lies along the axis of the scanner and represents the sinogram number (slice number); r is the radial coordinate (radial distance from the origin); and θ is the polar angle. This method takes into account scatter arising from activity outside the field of view [63].

A faster version (30 sec/bed position for adult thorax) of this method, which works on a single CPU computer, makes the clinical whole-body scatter correction more practical than previous approaches [67]. Similar methods are applicable to SPECT.

Monte Carlo Based (numerical) Scatter Correction:

Like analytical simulation-based corrections, Monte Carlo-based corrections employ the physics of photon interaction in matter, and require both transmission and initial estimates of emission data. The measured transmission and emission data are used to model the attenuation medium and distribution of photon emission, respectively. Photons are tracked along their path and the interactions with the attenuating medium are recorded, allowing the distinction between scatter and true counts (which is not possible in real applications). The scatter component obtained through these realistic simulations is removed from the sinogram data.

The drawback of these methods is the requirement of additional transmission data, advanced computers with large amount of memory and speed, and increased procedure time. These methods are often used for research purposes, and various Monte Carlo based simulation packages have been developed, as reviewed briefly in the next section.

Monte Carlo Simulation Tools in Emission Tomography

Monte Carlo methods are computer algorithms used in a broad area of science, in which physical processes are simulated with their known probabilities using random numbers. These methods are very suitable to simulate many applications in nuclear medicine. One common use in emission tomography, is to simulate the radiation transport of photons or charged particles from a given source distribution and evaluate their trajectories based on the physical interaction probabilities as they travel through the system (e.g., object of interest, collimators and scintillators) [68]. There are numerous publicly available Monte Carlo packages developed for both general purpose (including high-energy physics) and dedicated emission tomography simulations [69]. General-purpose simulation software is not suitable for emission tomography use because many of the interactions occur in high-energy physics does not appear in emission tomography, and inclusion of these adds unnecessary complexity. Among all the software in the latter group only SimSET (Simulation System for Emission Tomography) [70] includes both SPECT and PET simulations, whereas the rest simulate either SPECT or PET only. While SimSET doesn't include simulation of detector dead time, discrete detector blocks, dynamic source distribution etc., the package is sufficiently realistic for the purpose of this study, particularly with the recent inclusion of positron range and non-collinearity simulations of PET [31]. However, another drawback of SimSET is its relatively low amount of support material. Another alternative is GATE (Geant4 Application for Tomographic Emission) [10], a dedicated emission tomography simulation package based on the general purpose simulation platform Geant4 [71]. GATE performs more

realistic simulations and has a large amount of documentation and support availability. However, in order to fully take advantage of simulation capabilities of GATE a large amount of CPU resource is required.

CHAPTER III

IDL SIMULATIONS: EVALUATION OF

ATTENUATION CORRECTION

IDL, an array programming language, has found wide usage in medical imaging. Throughout this project we developed many IDL[16] routines for simulation, data manipulation, image analysis, and visualization purposes. However, our main focus was on tomographic simulations: We modeled data acquisition and reconstruction for both PET (at 511 keV) and SPECT (at 140 keV) in the presence of attenuation.

We developed IDL codes for both filtered back projection (FBP) methods (in spatial and frequency domains) and simple iterative algorithms for the reconstruction of 2D objects. Poisson noise and Gaussian blurring were modeled but not implemented in the simulations presented here, as the main objective of the IDL simulations was to analyze the role of attenuation correction.

In this simulation work we employed two different types of objects: A mathematical emission and attenuation phantom approximating a slice through the thorax, and chest slices selected from a real PET/CT study as shown in Figure 11 and Figure 12, respectively. The emission phantom represented the unknown radioactivity distribution, which is attenuated by its associated unknown attenuation phantom. Similarly, the PET slices represented the unknown radioactivity distributions and the CT slices their unknown attenuation media.

---

[16] Open source version GDL (GNU Data Language) is also used for various applications in this work. http://gnudatalanguage.sourceforge.net/
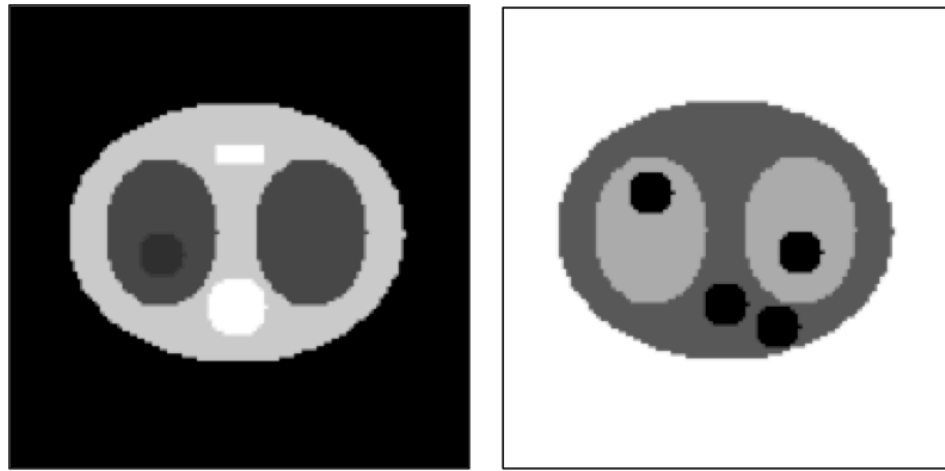
Figure 11 The unknown attenuation phantom on the left and the unknown emission phantom on the right are shown. Brighter colors on the attenuation map represent the larger attenuation coefficients. Darker colors in the emission data represent the higher radioactivity counts
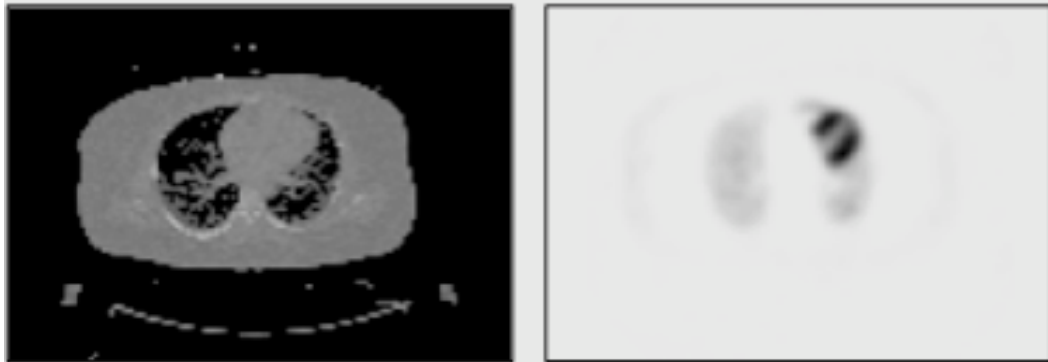
Figure 12 The unknown attenuation distribution from a real CT slice (on the left) and the unknown emission distribution from the associated PET slice (on the right) are shown. Brighter colors on the attenuation map represent the larger attenuation coefficients. Darker colors in the emission data represent the higher radioactivity counts.

Projections through these objects and their reconstruction were simulated. The objective of the reconstruction is to obtain (or estimate) the unknown radioactivity distribution. The details of these simulations are presented here.

The objects (phantom and real CT slice) were scaled to correspond to 5 different sizes (length of the main axis): human (36 cm), dog (18 cm), rabbit (9 cm), rat (4.5 cm)

and mouse (2.25 cm). Scaling was done through adjusting pixel sizes, which simplified the visual comparison since the displayed sizes remained the same.

The elliptical attenuation phantom contained several structures representing biological materials such as tissue (lungs) and bones (sternum and vertebrae), and their approximate average linear attenuation coefficient values at 511 keV and 140 keV energies. The sternum and vertebrae consist of cortical bone (PET: 0.170 cm^{-1} and SPECT: 0.282 cm^{-1}) and trabecular bone (PET: 0.110 cm^{-1} and SPECT: 0.182 cm^{-1}) types. In the attenuation phantom a single attenuation coefficient, approximating a weighted average of cortical bone and trabecular bone values derived from a human CT slice, is used[17]. Similarly a single value is used to represent lung areas, except an additional structure added to one of the lungs. The rest of the phantom is defined as water.

Linear Attenuation Coefficients (cm^{-1})				
Material $\Rightarrow$	Bone Structures	Water/Tissue	Lungs	Arbitrary Structure
511 keV	0.125	0.096	0.035	0.025
140 keV	0.196	0.155	0.056	0.040

Table 4 Linear (μ) attenuation coefficients for PET and SPECT (^{99m}Tc, 140 keV) photons for various biological materials approximated for the phantom study.

Similar to the mathematical phantom, the real PET slice represented the radioactivity distribution attenuated by its real CT slice. The real CT slices, originally in Hounsfield units (HU), were converted into linear attenuation coefficients of x-ray beam

---

[17] An open source medical imaging software OsiriX (Mac OS X application only) is used for identification of the anatomy and reading HU values.

(effective energy ~70 keV), using the following equation;

$$\mu^{70keV} = \mu_{water}^{70keV}(1 + HU/1000) \tag{24}$$

in which the attenuation coefficient of water is 0.184 cm^{-1} at 70 keV. Consequently, these values were scaled to the attenuation coefficients at 511 keV and 140 keV photons of PET and SPECT, respectively. The bone and the rest of the material were segmented by using a threshold value[18] to scale bone and other regions, separately [72]: A single conversion factor (different for PET and SPECT) was applied to transform the attenuation coefficients of all the low Z materials such as tissue, water and lungs since Compton scattering is the only dominant interaction in the energy range of 70 keV-511 keV. However, for the bone region a different conversion factor was used since photoelectric effect forms a significant portion of the attenuation in the bone at 70 keV, but is negligible at 140 keV and 511 keV.

The discrete implementation of the attenuated line integrals (i.e., ray sum) for PET and SPECT are shown below. Here, μ_{CT} represents the linear attenuation coefficients for both phantom and real data simulations, f(n) is the image (radioactivity) value at pixel n, τ is the pixel size in cm, and N is the total number of pixels along the projection line.

PET:
$$p_\theta = \sum_{n=0}^{N} f(n) \cdot e^{-\tau \sum_{a=0}^{N} \mu_{CT}(a)} \tag{25}$$

SPECT:
$$p_\theta = \sum_{n=0}^{N} \left(f(n) \; e^{-\tau \sum_{a=0}^{n} \mu_{CT}(a)} \right) \tag{26}$$

---

[18] Alternatively, a threshold can be applied in HU units prior to conversion into linear attenuation coefficients.

The simulated projections were reconstructed using FBP (in spatial domain) in three different ways:

- Perfect correction: This represents the ideal reconstruction of the true radioactivity distribution, where projection files are obtained in the absence of attenuation material. This is equivalent to the attenuation correction using an accurate attenuation map. This serves as the reference image for the comparison of reconstructed images.

- Uniform attenuation correction using body contour: The projections are obtained in the presence of attenuation effect. This correction is performed using the emission data only, obtained through acquisition. The emission data is employed to specify the boundaries of the image. For the uniform attenuation map inside these boundaries, the water attenuation coefficient is assumed (0.096 cm^{-1} and 0.155 cm^{-1} for PET and SPECT) and incorporated in the reconstruction algorithm.

- Without attenuation correction: The projections obtained in the presence of attenuation effect are directly reconstructed without applying any attenuation correction.

For the reconstruction with attenuation correction, the uniform attenuation maps in PET and SPECT simulations were incorporated in the acquisition of the projection files, as shown below.

PET:
$$p_\theta = \sum_{n=0}^{N} f(n) \cdot e^{-\tau \sum_{a=0}^{N} (\mu_{CT}(a) - \mu_{water})}$$
(27)

SPECT:
$$p_\theta = \sum_{n=0}^{N} \left(f(n) \; e^{-\tau \sum_{a=0}^{n} (\mu_{CT}(a) - \mu_{water})} \right)$$
(28)

This is equivalent to attenuation of the emission data, f(n), by incorporating the difference between the original attenuation data and the uniform attenuation map in the projections. This effectively creates a resultant attenuation media that attenuates less. However, when the material attenuation coefficient is originally less than water attenuation coefficient, such as projection through the lungs, the correction overestimates the values introducing artifacts.

The reconstructions with and without attenuation correction were compared to the perfect reconstruction for various regions selected on both the mathematical phantom (9 regions) and the real slice (6 regions). The regions of mathematical phantom represented hot and cold lesions in tissue, bond and lung areas. The regions of the real phantom included lung, tissue and heart with different radioactivity. Lung and non-lung areas were compared separately since the behavior was different in these regions. For each region, the absolute percent error ratios were obtained by applying:

PET:
$$Error\% = 100 \left(\frac{perfect - attenuated}{perfect} \right)$$
(29)

where "perfect" denotes reconstructions in the absence of attenuation, and "attenuated" represent attenuated reconstructions with or without correction. Consequently, the average of these error values from 4 regions of lung area and 5 regions of non-lung area were calculated. For the real data, a similar method was followed for four different slices, which are then averaged.

Results

The mean error percent values were calculated for 5 different sizes of both digital phantoms and real data for lung and non-lung regions. These values are presented in Tables 5 and 6, respectively. Results indicated that reconstruction with uniform attenuation correction significantly improved the quantitative accuracy of both PET and SPECT for all object sizes within non-lung regions. The mean errors in the uniform AC images for non-lung regions in digital phantoms and real data were as follows: less than 1.0% and 1.8% for mouse size, 2.5% and 3.8% for rat size, and 6.0% and 8% for rabbit size. However, in the lung area the AC overestimated the activity (error values were negative), increasing the absolute error values of phantom data but decreasing the absolute error in real data. Percent errors are plotted in Figures 13 and 14 (including negative values) for PET and SPECT phantom data, respectively. Similarly, the results for PET and SPECT real data are presented in Figures 15 and 16.

In addition to the quantitative analysis, an image-based comparison is also presented. Attenuation corrected (AC) and not corrected (NC) reconstructed images from these simulations are displayed for the digital phantom in Figure 17 and for real data in Figure 18. In these figures, the images on the 2nd and 3rd rows show the reconstructed PET images without (NC) and with (AC) uniform attenuation correction, respectively. Similarly, the 4th and 5th rows show the reconstructed images from the SPECT simulations. As expected, with decreasing object size (from left to right), the reconstructed images visually approach the accurate reconstruction (1st row 4th column). For the smallest sizes the difference on the images are negligible.

Discussion

We performed a series of PET and SPECT simulations to assess the value of the attenuation correction for various sizes of objects in the absence of scatter effect. We presented reconstructed images for both digital phantom and real data. Through visual

assessment, the progress of the reconstruction can be seen qualitatively as object size decreases. However, our evaluation was based on quantitative analysis of selected ROIs. Although a limited number of slices were included in the simulations, slices chosen were representative of clinical studies. Moreover, regions of interest were selected to sample different emission and attenuation areas. We observed similar behavior for both the digital phantom and real data simulations. In all cases, the absolute error percents decreased regularly with decreasing object size. In addition, the orders of magnitude were within the same range (except in the attenuation corrected lung regions) for these two independent data sets.

Although these 2D simulation studies did not include scatter effect, they allowed us to obtain reasonable preliminary results on a personal computer before conducting more sophisticated simulations. We then performed more realistic simulations of 3D PET and SPECT, including scatter and other physical effects, using the Monte Carlo based software package GATE. These are presented in the next chapter.

Conclusion

These results suggest that, in quantitative PET and SPECT studies requiring 5 -10 % accuracy, uniform attenuation correction is sufficient up to rabbit size animals for regions excluding the lungs. However, if accurate results are required throughout the body, it appears that transmission studies are necessary.

PHANTOM DATA									
	PET - LUNG AREA					PET – NON LUNG AREA			
Size	Human	Dog	Rabbit	Rat	Mouse	Human	Dog	Rabbit	Rat	Mouse
NC	77.6	51.2	29.3	15.6	8.0	95.4	77.6	51.8	30.4	16.5
AC	-430.5	-150.8	-63.8	-29.5	-14.1	71.6	17.8	5.9	2.4	1.0
	SPECT- LUNG AREA					SPECT– NON LUNG AREA			
Size	Human	Dog	Rabbit	Rat	Mouse	Human	Dog	Rabbit	Rat	Mouse
NC	64.7	41.8	23.8	12.6	6.5	79.6	61.5	40.8	23.9	13.0
AC	-434.7	-133.5	-53.7	-24.2	-11.5	68.1	15.2	5.1	2.1	0.9

Table 5 Absolute values of the mean error percents for the attenuation corrected (AC) and not corrected (NC) reconstructions for phantom data. The emission values in the lung-area were overestimated (i.e. negative errors)

REAL DATA									
	PET - LUNG AREA					PET – NON LUNG AREA			
Size	Human	Dog	Rabbit	Rat	Mouse	Human	Dog	Rabbit	Rat	Mouse
NC	86.2	63.5	40.0	22.7	12.1	89.2	67.2	42.8	24.4	13.0
AC	-50.4	-23.2	-11.1	-5.5	-2.7	17.9	8.3	3.7	1.7	0.8
	SPECT- LUNG AREA					SPECT– NON LUNG AREA			
Size	Human	Dog	Rabbit	Rat	Mouse	Human	Dog	Rabbit	Rat	Mouse
NC	77.5	53.6	32.3	17.8	9.4	78.6	55.4	34.0	18.9	10.0
AC	-47.1	-21.5	-10.0	-4.8	-2.4	40.6	17.8	8.0	3.8	1.8

Table 6 Absolute values of the mean error percents for the attenuation corrected (AC) and not corrected (NC) reconstructions for real data. The emission values in the lung-area were overestimated (i.e. negative errors)
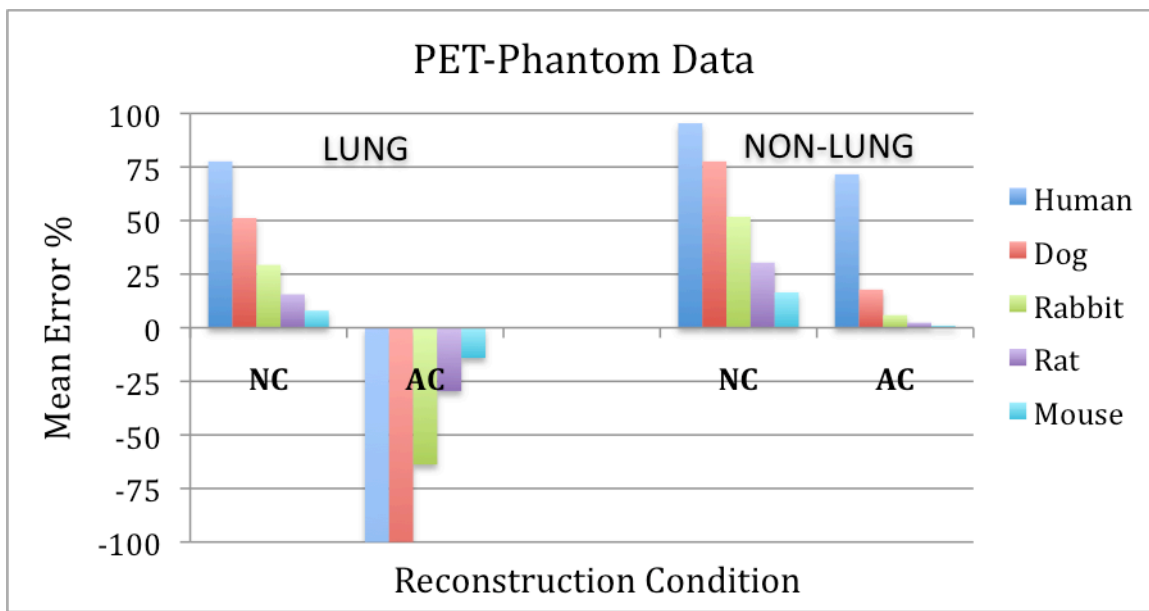
Figure 13 PET-phantom study mean error percents for lung and non-lung regions for 5 different sizes with and without attenuation corrections. Negative values indicate overestimation.
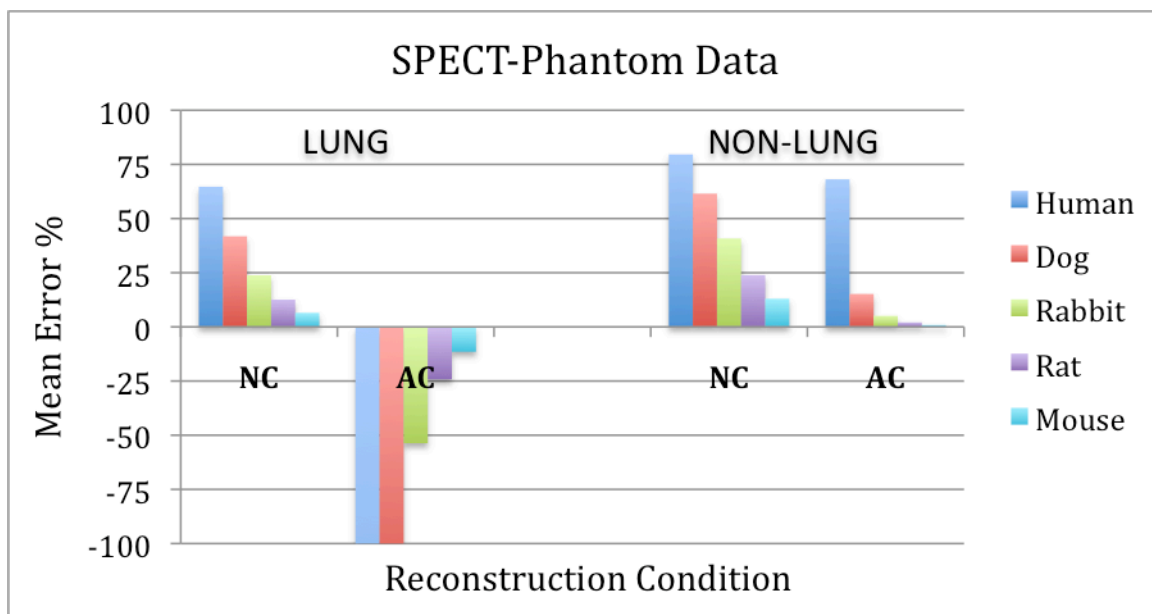
Figure 14 SPECT-phantom study mean error percents for lung and non-lung regions for 5 different sizes with and without attenuation corrections. Negative values indicate overestimation.
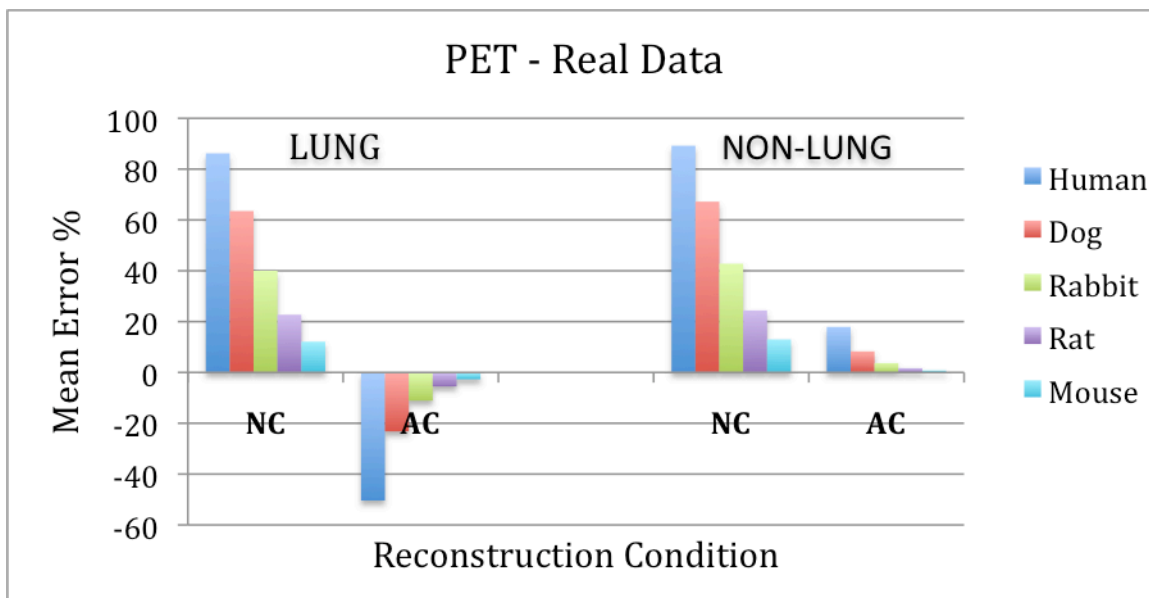
Figure 15 PET-real data study mean error percents for lung and non-lung regions for 5 different sizes with and without attenuation corrections. Negative values indicate overestimation.
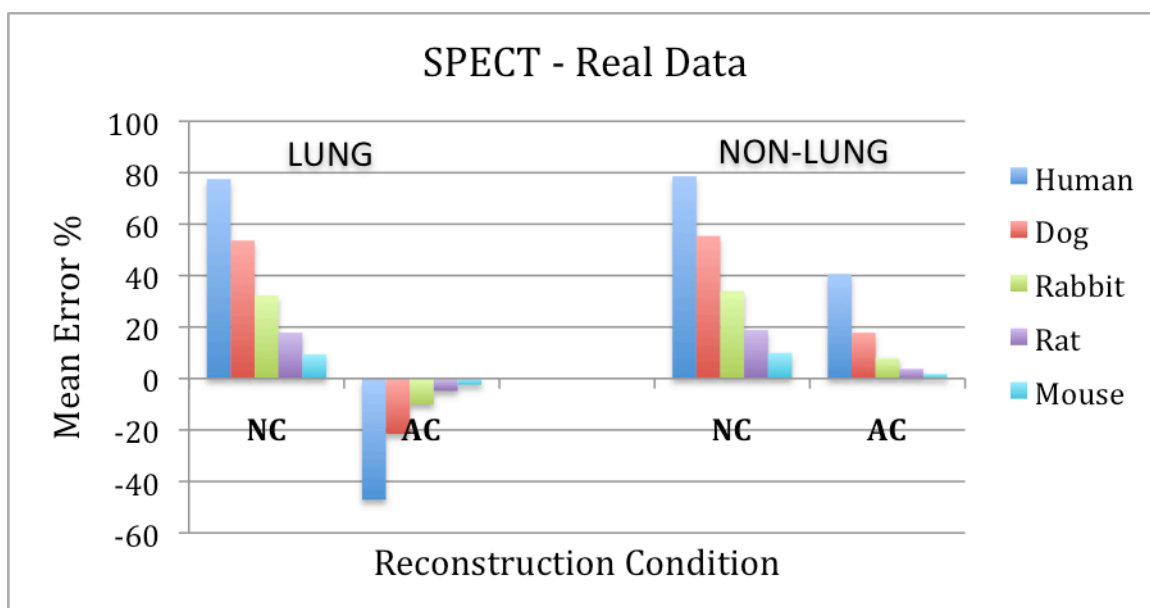
Figure 16 SPECT-real data study mean error percents for lung and non-lung regions for 5 different sizes with and without attenuation corrections. Negative values indicate overestimation.
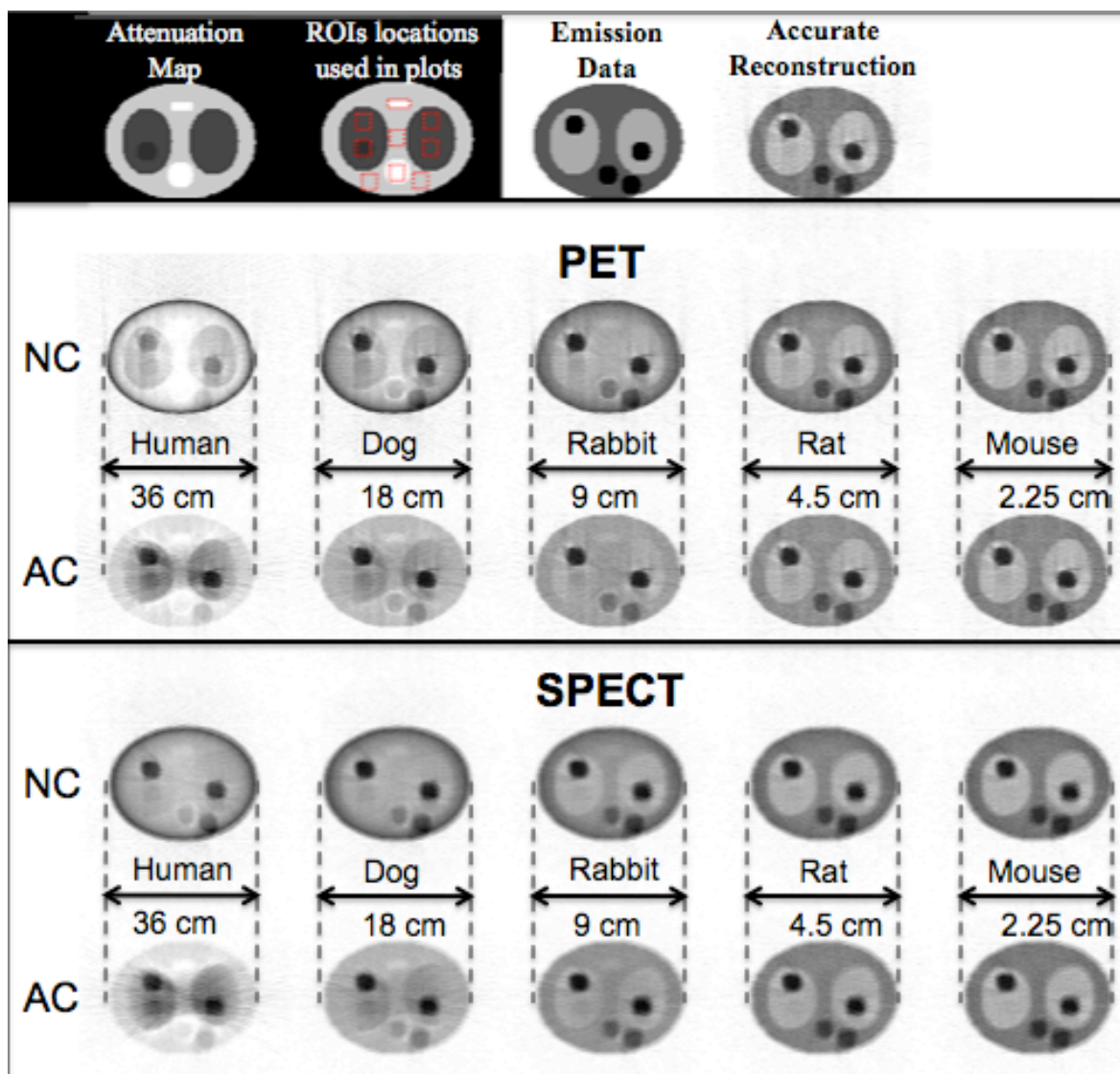
Figure 17 Images from mathematical phantom simulations. ROIs are indicated in the image located in 1st row of the 2nd column. Attenuation corrected (AC) and not corrected (NC) images are shown for various phantom sizes. Brighter colors on the attenuation map represent larger attenuation coefficients in cm^{-1}: 0.125, 0.096, 0.35 and 0.25 for PET; 0.196, 0.155, 0.56 and 0.40 for SPECT). Darker colors in the emission data represent regions of higher radioactivity counts and are identical for PET and SPECT (155, 100 and 55).
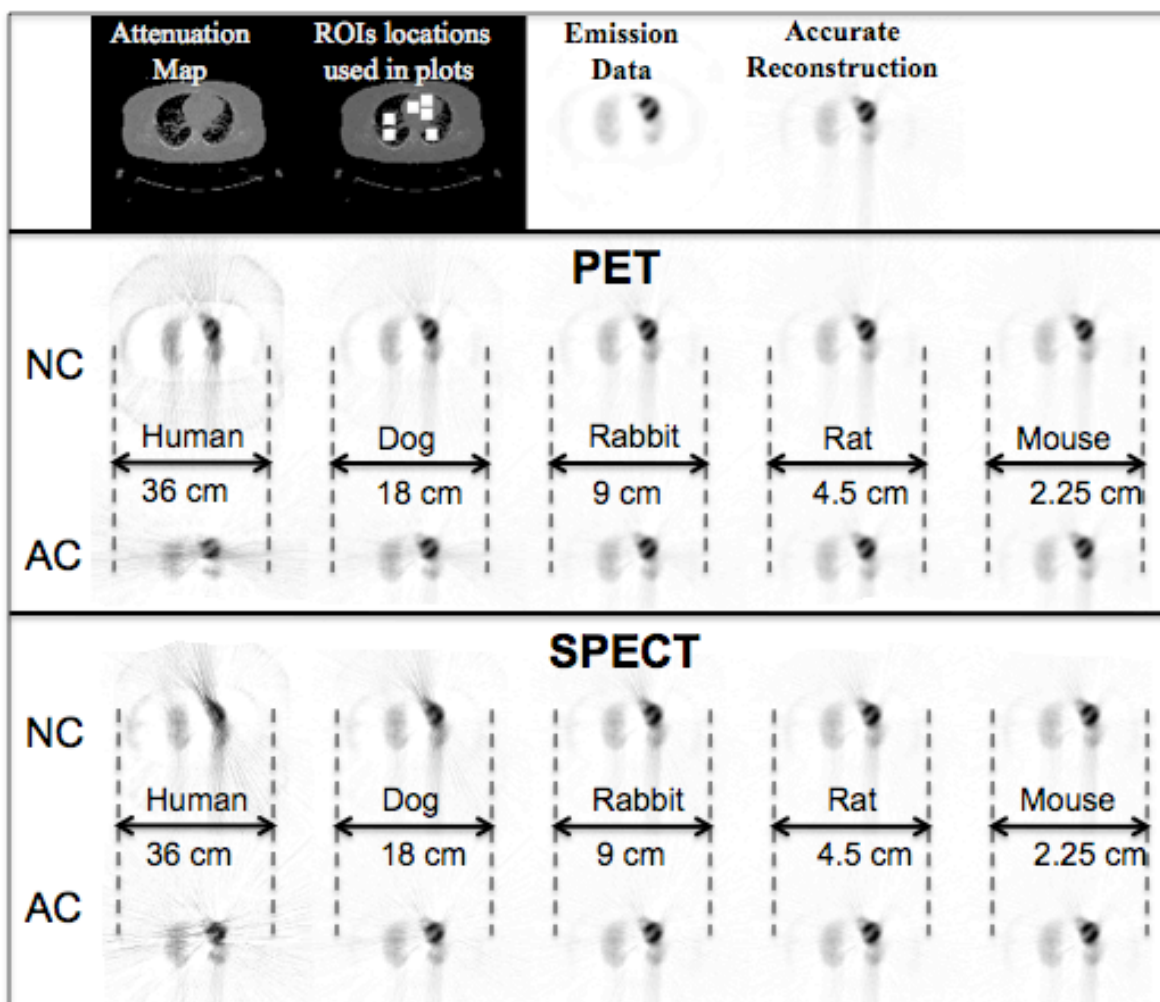
Figure 18 Images from mathematical phantom simulations. ROIs are indicated in the image located in 1st row of the 2nd column. Attenuation corrected (AC) and not corrected (NC) images are shown for various sizes of chest data. Brighter colors on the attenuation map represent larger attenuation coefficients values. Darker colors in the emission data represent regions of higher radioactivity count density.

CHAPTER IV

GATE SIMULATIONS: SCATTER FRACTION

MEASUREMENTS

Experiments involving radioactivity and expensive instruments of emission tomography can limit research due to operational costs and radiation exposure. Monte Carlo methods present an attractive solution to overcoming these difficulties encountered in real experiments. There are open-public Monte Carlo software packages such as Simset and GATE dedicated to emission tomography. GATE was more suitable for this research because of increasing popularity and available support [73]. It allows the user to model detailed scanner geometries and radiation interactions with matter, track events (recording position, time, energy, momentum information and nature of events), and create various types of output files including sinograms. This is achieved through macro files where the details of a simulation are listed by command lines.

GATE simulations often require a large amount of computer resources, although performing short experiments is possible on personal computers. We installed the GATE package (following the installation of Geant4 and other libraries) on a LINUX computer cluster with 48 CPU capacity provided by the University of Iowa Information Technology Service (UI ITS) and two personal computers. The use of these two personal computers allowed us to develop the necessary macros and testing of our models before submitting lengthy simulations to the cluster computers.

We used three different scanner models in our simulations: Siemens ECAT HR+ clinical PET scanner [74], Siemens Inveon small animal PET [75] and small animal SPECT scanners [76]. The ECAT clinical scanner model, already included in the GATE package, has been well validated and widely used in many other simulation studies [77]. Using a scripting mechanism available in GATE, we generated our own models of the other two small animal scanner geometries in accordance with the original scanner

specifications given by Siemens[19]. The specifications of all three scanners are summarized in Table 7.

Specifications	SCATTER FRACTION %		
	ECAT HR+	Inveon PET	Inveon SPECT
Crystal Material	BGO	LSO	NaI (Tl)
Crystal Size (mm^3)	4.39 x 4.05 x 30	1.5 x 1.5 x 10	2 x 2 x 10
Crystal pitch (mm)	6.5417	1.59	2.2
Crystal array (mm)	8 x 8	20 x 20	68 x 68
Number of detector blocks	72	64	2 Detector Heads 15 x 15 cm^2
Number of rings	32	80	–
Number of crystal elements	18432	25600	4624 / head
Transaxial FOV (cm)	58.5	10	–
Axial FOV (cm)	15.5	12.7	–

Table 7 General specifications of the real PET and SPECT scanners modeled for GATE simulations.

Our GATE simulations consisted of 2 main parts: Scatter Fraction measurements (presented in this chapter) and analysis of reconstructed images (presented in the next chapter).

Scatter Fraction Measurements

Scatter Fraction (SF), the ratio of scatter to the total[20] counts, is a useful parameter in estimating the impact of scatter on images and is measured in most scanner

---

[19] www.medical.siemens.com

[20] Total counts in PET formed by the sum of true, scatter, random, and intrinsic (when the crystal material itself is radioactive as in LSO) counts. In SPECT, total counts are the sum of scatter and true counts.

performance studies. It depends predominantly on the object size and the mode of acquisition (2D versus 3D) for a given emission energy and scanner geometry. Therefore, the magnitude of scatter fraction can be a good indication of whether scatter correction is needed and to what level it is necessary. In 2D-mode clinical PET scanners scatter correction is either performed with algorithms based on emission data (e.g. Gaussian curve-fitting method) [54] or ignored altogether as the magnitude of the scatter fraction was within an acceptable range (10-20%). However, in 3D clinical whole body SPECT and PET the impact of scatter is significantly larger (35-60%). Scatter fraction of this magnitude requires more accurate approaches employing an additional transmission scan from either an x-ray CT or external gamma source [63, 78]. In contrast, although small animal imaging is performed exclusively in 3D mode, scatter fraction values reported for these studies are significantly lower [75, 79] (mouse 5.7- 10% and rat 14.6- 24%)[21], and thus they may not need transmission-based corrections as in the case of 2D-mode PET.

Scatter fraction measurements are typically done as part of a scanner performance study. There are many scatter fraction values reported in the literature for various simulated or real scanners either part of a scanner performance study, which explored only limited type and size of phantoms [80-82] or focused on various aspects such as energy windows [55]; however, none of these studies appeared to have investigated the scatter fraction for an extended range of object sizes. Thus, the objective of this simulation study was to determine the scatter fraction values over a wide range of phantom sizes with both clinical and small animal tomographs.

Because these measurements should be made at low count rates to minimize random coincidences, the amount of imaging time to perform such imaging studies for a wide range of object sizes is impractical with real scanners. Another time consuming

---

[21] SF values vary depending on the geometry, energy window and the method is used.

procedure is derivation of the scatter component indirectly through a tail fitting method. These difficulties can be overcome using GATE, which provides direct measurements of scatter component in a much shorter time, provided there are sufficient CPU resources.

Concurrent simulations for different object sizes were submitted on individual processors of the cluster. The system scatter and true counts were directly obtained from the ROOT[22] output, and the scatter fraction values were calculated from these outputs without needing to follow lengthy NEMA procedure. In the case of the Inveon PET scanner, the intrinsic radioactivity from its LSO crystals[23] [83] was not incorporated in the simulations since that correction was already assumed.

All the scatter fraction measurements of PET (Inveon and ECAT) and SPECT (Inveon single-pinhole) scanners were performed in 3D acquisition mode. Since the scatter fraction is highly dependent on photon energies, emissions from various radionuclides were simulated, including 511 keV annihilation photons for PET[24] and emission of three different SPECT radionuclides: ^{99m}Tc, ^{111}In and ^{125}I. In addition, as commonly applied in real studies, we performed the Inveon PET simulations using both narrow (350-650 keV) and wide (250-750 keV) energy windows. While a narrow window decreases the scatter, it limits the count and results in noisier images. A large window, on the other hand, increases the detection sensitivity at the expense of elevated scatter counts.

We applied the procedures explained above for a wide range of sizes of several different digital phantoms including NEMA (mouse type, rat type and human type) cylindrical phantoms, MOBY (mouse/rat) and XCAT (human) realistic phantoms.

---

[22] ROOT is an object oriented framework for large scale data analysis: http://root.cern.ch/drupal/

[23] LSO crystals contains 2.6% of ^{176}Lu (with a half-life of 3.5 x 10^{10} years), which decays through β$^-$ emission and cascade of γ-rays.

[24] Positron emission is not included in the simulations to reduce the computational times.

NEMA-Type Phantoms Scatter Fraction Measurements

NEMA phantoms are cylindrical objects made of polyethylene (~0.96 g/cm^3) with a radially offset line source inside. They are designed to approximate the scatter fraction of the same size cylindrical water phantoms with homogeneous radioactivity distribution [84]. The diameter and length of these phantoms are designed to simulate scatter distribution in human or different types of animals (e.g., mouse and rat). The standard NEMA mouse, rat and human type phantoms are 2.5, 5, and 20 cm in diameter and 7, 15 and 70 cm in length. A screenshot of PET simulations for the standard sizes are shown in Figure 15.

The geometry commands available in GATE allows the user to create simple objects such as cylindrical phantoms as used in NEMA studies. For our scatter fraction measurements, we incorporated a shell script controlling GATE macro parameters, which allowed the simulations of NEMA phantoms for a range of diameters including the standard sizes: 2-5 cm (mouse type), 3-9 cm (rat type), and 10-56 cm (human type). This corresponded to 13 different sizes of mouse and rat-sized phantoms, and 24 different sizes of human-sized phantoms[25]. The phantom and line-source lengths were kept unchanged, as specified in NEMA. In addition, the ratios between the radius and the line-source distance to the phantoms' center held constant. Mouse and rat sized phantoms were simulated in small animal Inveon PET and SPECT scanners, and human sized phantoms in ECAT PET scanner. The relevant data acquisition parameters for these scanners are shown in Table 8.

---

[25] For SPECT simulations, the diameters up to 5 cm were measured due to the limited field of view of the scanner.

Scanner	Inveon PET Inveon SPECT		ECAT PET
Phantom	Mouse	Rat	Human
Phantom material	Polyethylene (~ 0.96 g/cm³)		
Phantom length	7 cm	15 cm	70 cm
Line source length	6 cm	14 cm	70 cm
Crystal Energy resolution %	PET: 14.6 (LSO) SPECT: 10 NaI (Tl)		20 (BGO)
Coincidence Window	3.43 ns N/A for SPECT		10 ns
Photopeak Energy Window (keV)	**PET:** 350-650 and 250-750		350-650
	SPECT: ⁹⁹ᵐTc: 126-154 ¹¹¹In : 154-188 and 220-288 ¹²⁵I: 25-32		

Table 8 The ratio between the radius and the line-source distance to the phantoms' center was also kept constant as in NEMA: 0.8, 0.7 and 0.45 for mouse, rat and human phantoms, respectively.

We performed the simulations for relatively low acquisition times obtaining sufficient counts ($\sim 10^5$ - 10^6) for the purpose of this work. At these count levels, the maximum variation of scatter fraction % values did not exceed ±1%. For all sizes of a NEMA phantom, a single random seed is used to limit the variations to the change of size and source location. The scatter fraction values reported in the literature are based on the NEMA procedure, where events originating 8 mm outside the phantom boundary, are ignored and set to zero on the projection profiles prior to measurement. This significantly reduces the number of scatter counts. Our small animal PET simulation results reported here are based on both raw data, directly obtained from simulations and modified data as explained in NEMA procedure [13]. For the latter, the boundaries are determined from the PET sinogram data.
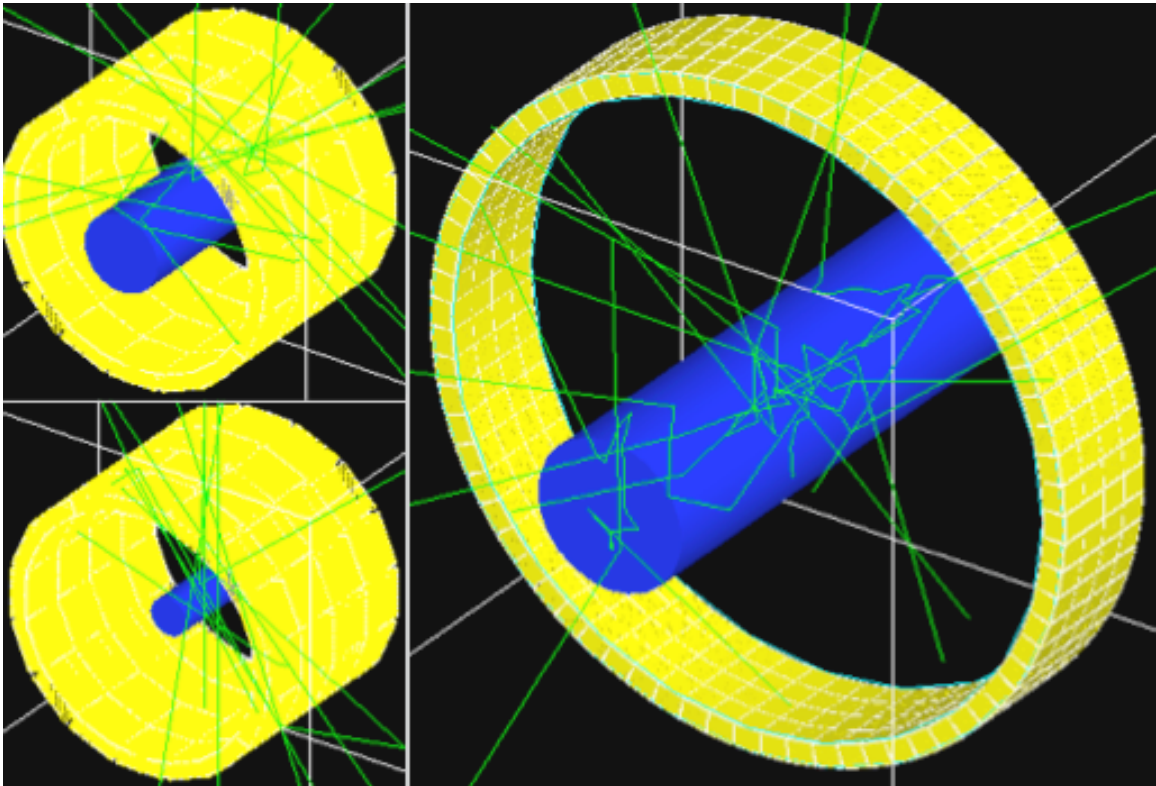
Figure 19 GATE simulations of Inveon small animal PET scanner for rat (top left) and mouse (lower left), and ECAT PET scanner for human (right) sized NEMA phantoms. Standard phantom sizes are shown. The green lines represent the photon emissions, which are detected by the surrounding detectors (yellow).
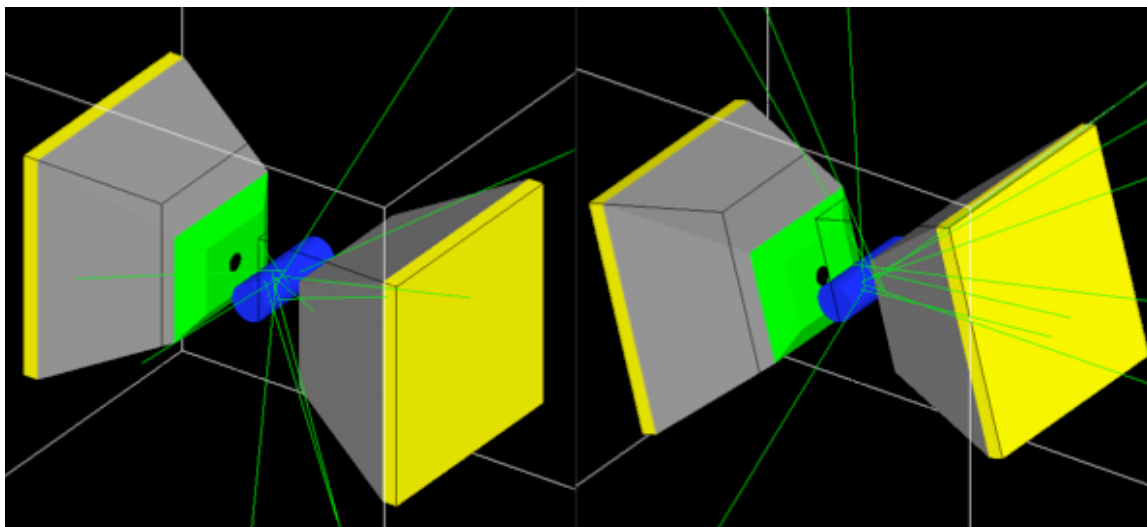
Figure 20 Inveon small animal SPECT simulations shown for the standard NEMA mouse size. Two camera heads, each consisting of a single-pinhole collimator (green), shield (gray) and detector arrays (yellow), rotate around the phantom to collect photons.

Our scatter fraction results obtained for standard NEMA phantoms of PET simulations were: 4.9% (9.4% for the raw data) and 17.5% (21.2% for the raw data) for mouse and rat-sized NEMA phantoms (Inveon at 350-650 keV photopeak window) and 56.5% for human-sized NEMA phantom (ECAT). These findings are consistent with standard NEMA results found in other studies using the same scanner and similar acquisition parameters (e.g., energy window) [75, 85, 86]. When diameter sizes were varied, scatter fraction values (based on NEMA procedure) were found to range between 3-13% for mouse (2-5 cm); 8-32% for rat (3-9 cm) and 35-85% for human phantoms (10-56 cm). These results are presented in Figure 17 through 21, for mouse, rat and human type NEMA phantoms, respectively.

The SPECT results were limited to 5 cm diameter mouse and rats. For this largest size, the scatter fraction of SPECT using ^{99m}Tc radionuclide was 3-4% lower than the values obtained in small animal PET. On the other hand, scatter fractions were significantly higher for relatively lower energy photons of ^{125}I (~30 keV): ~15 - 24% for mouse and ~27 - 35% for rat. At this energy level, the contribution from Rayleigh scatter

was about 0.4 that of Compton scatter. In addition to these radionuclides, we simulated two emission photons 171 keV (90%) and 245 keV (94%) of the ^{111}In in separate photopeak windows. The downscatter from 245 keV photons is also included in the scatter fraction measurement of the 171 keV photopeak window (154-188 keV) using the equation:

$$SF_{171keV} = \frac{90 \times Scatter(171keV) + 94 \times Downscatter(245keV)}{90 \times Total(171keV) + 94 \times Downscatter(245keV)} \qquad (30)$$

The results from the SPECT scanner simulations of mouse and rat type NEMA phantoms are given in Figure 24 and Figure 25, respectively.
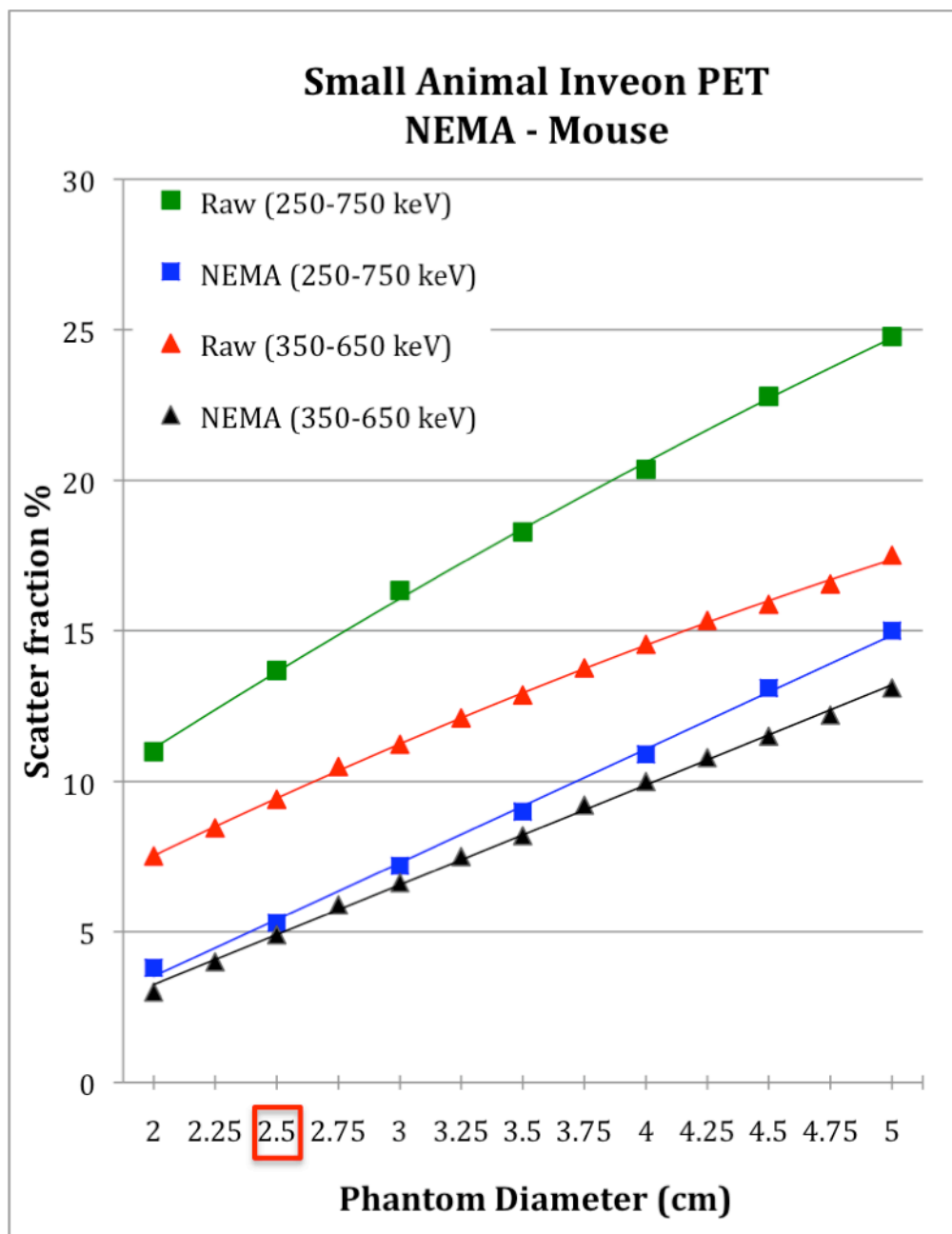
Figure 21 SF % for different diameters of mouse-like NEMA phantoms (7 cm long). The standard NEMA size is indicated on the horizontal axis (red box). Results are based on the simulations of Siemens Inveon small animal PET scanner at two different energy windows (square data points represent the 250-750 keV window; triangular points represent the 350-650 keV window). The SF values dropped significantly when projections 8 mm outside of the object boundary were set to zero (NEMA procedure).
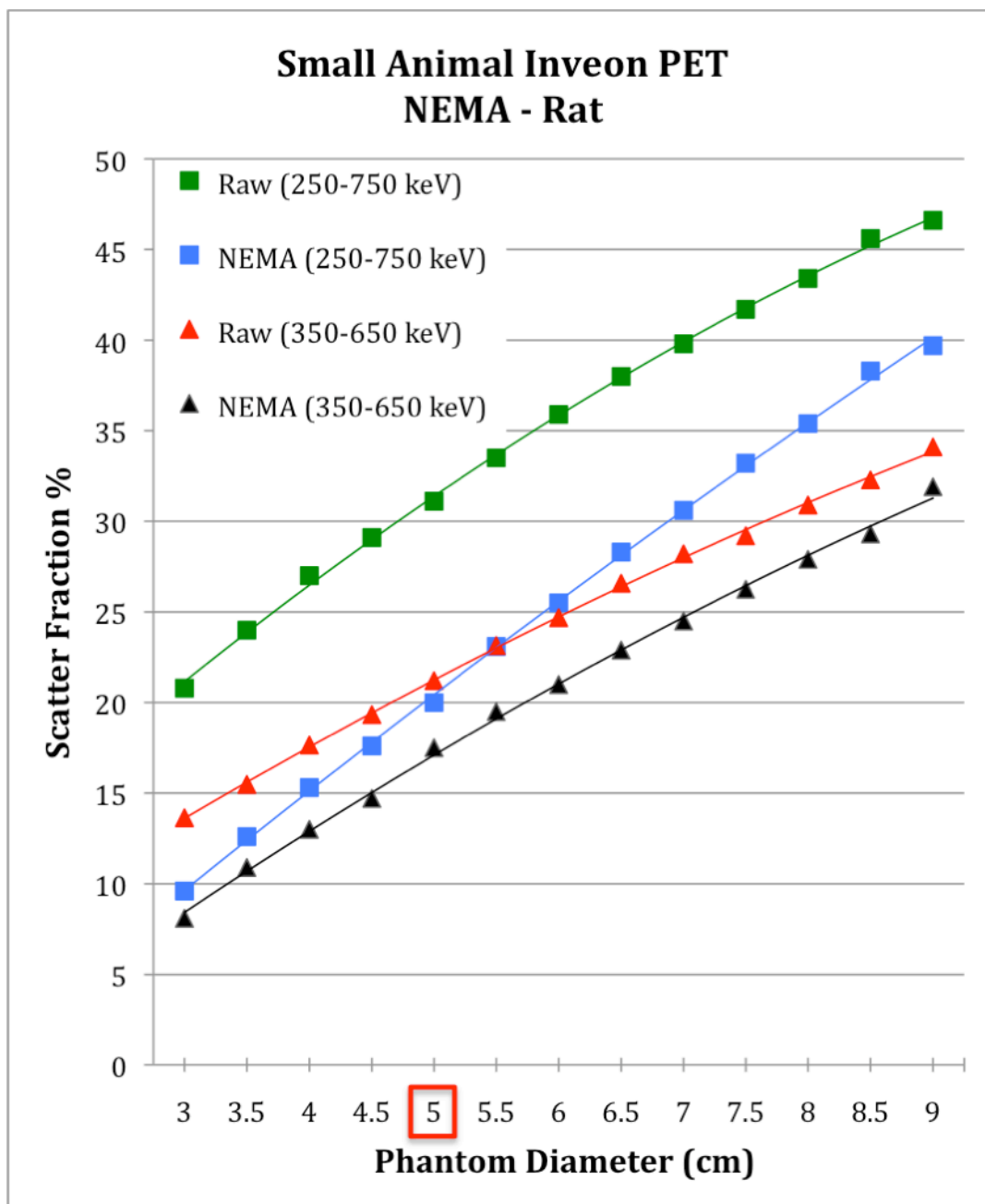
Figure 22 SF % for different diameters of rat-like NEMA phantoms (15 cm long). The standard NEMA size is indicated on the horizontal axis (red box). Results are based on the simulations of Siemens Inveon small animal PET scanner at two different energy windows (square data points represent the 250-750 keV window; triangular points represent the 350-650 keV window). The SF values dropped significantly when projections 8 mm outside of the object boundary were set to zero (NEMA procedure).
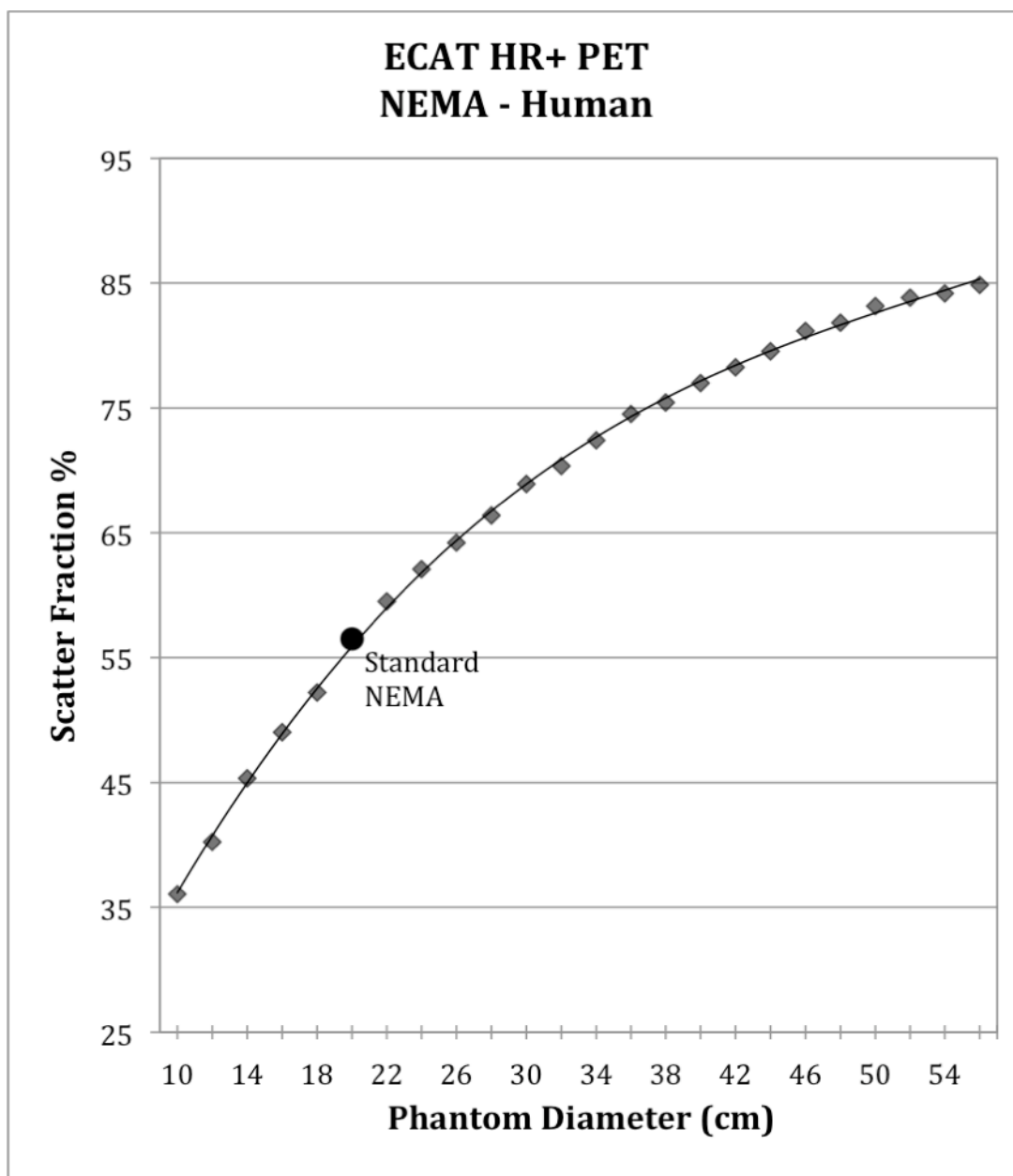
Figure 23 Scatter fraction values for human-like NEMA phantoms (70 cm long).The Scatter fraction value for the standard NEMA size is shown with the circular data marker. The results are based on the simulations of Siemens ECAT HR+ clinical PET scanner and were obtained from raw data.
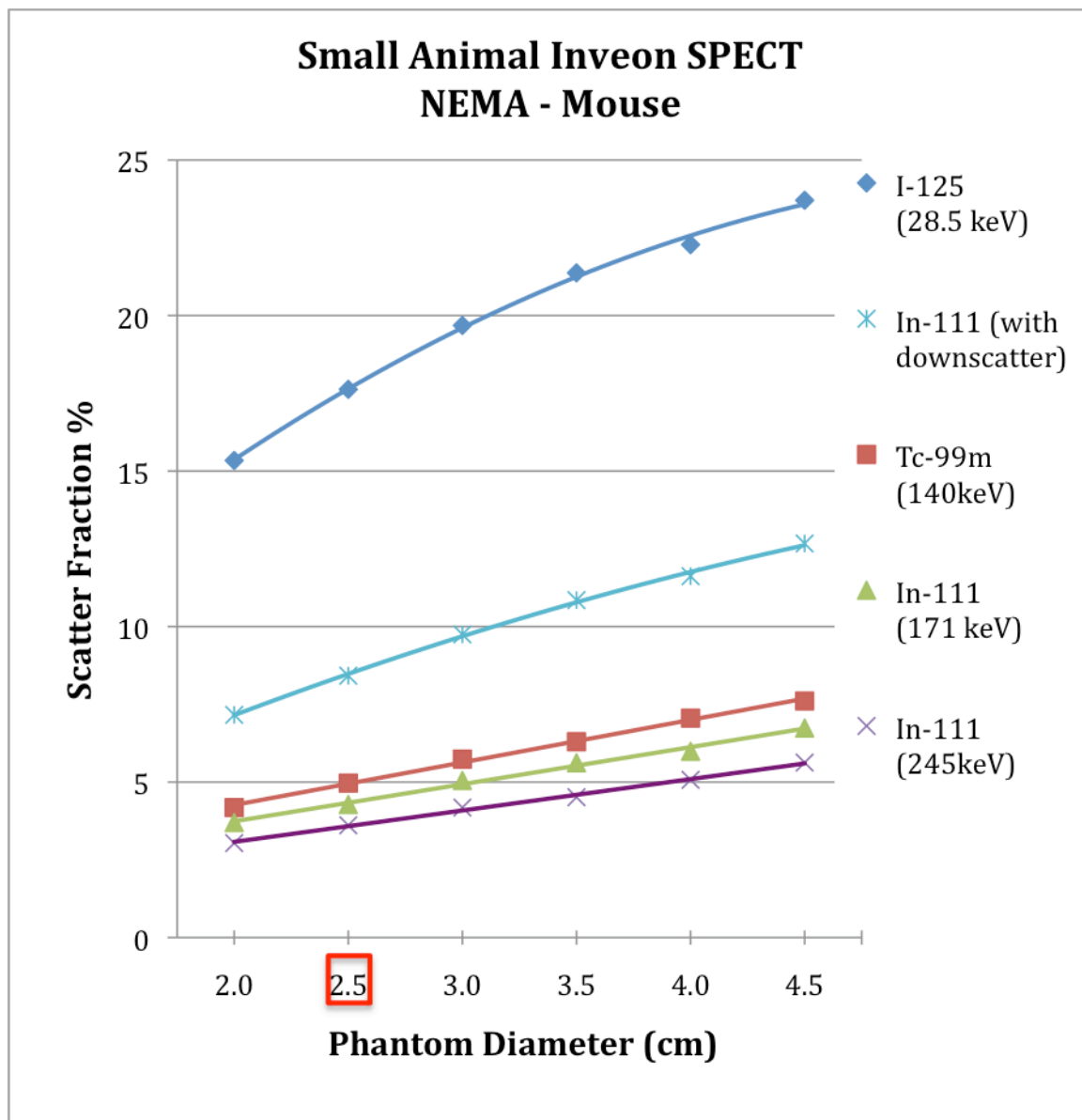
Figure 24 Scatter Fraction % values for different diameters of mouse-like NEMA phantoms (7 cm long), where the standard NEMA diameter size is 2.5 cm. Results are based on the simulations of Siemens Inveon small animal SPECT scanner. An effective emission energy is used for [125]I. SF for ^{111}In are presented for 2 separate photopeak windows. SF for the 171 keV photopeak window (154-188 keV) are shown with and without 245 keV downscatter.
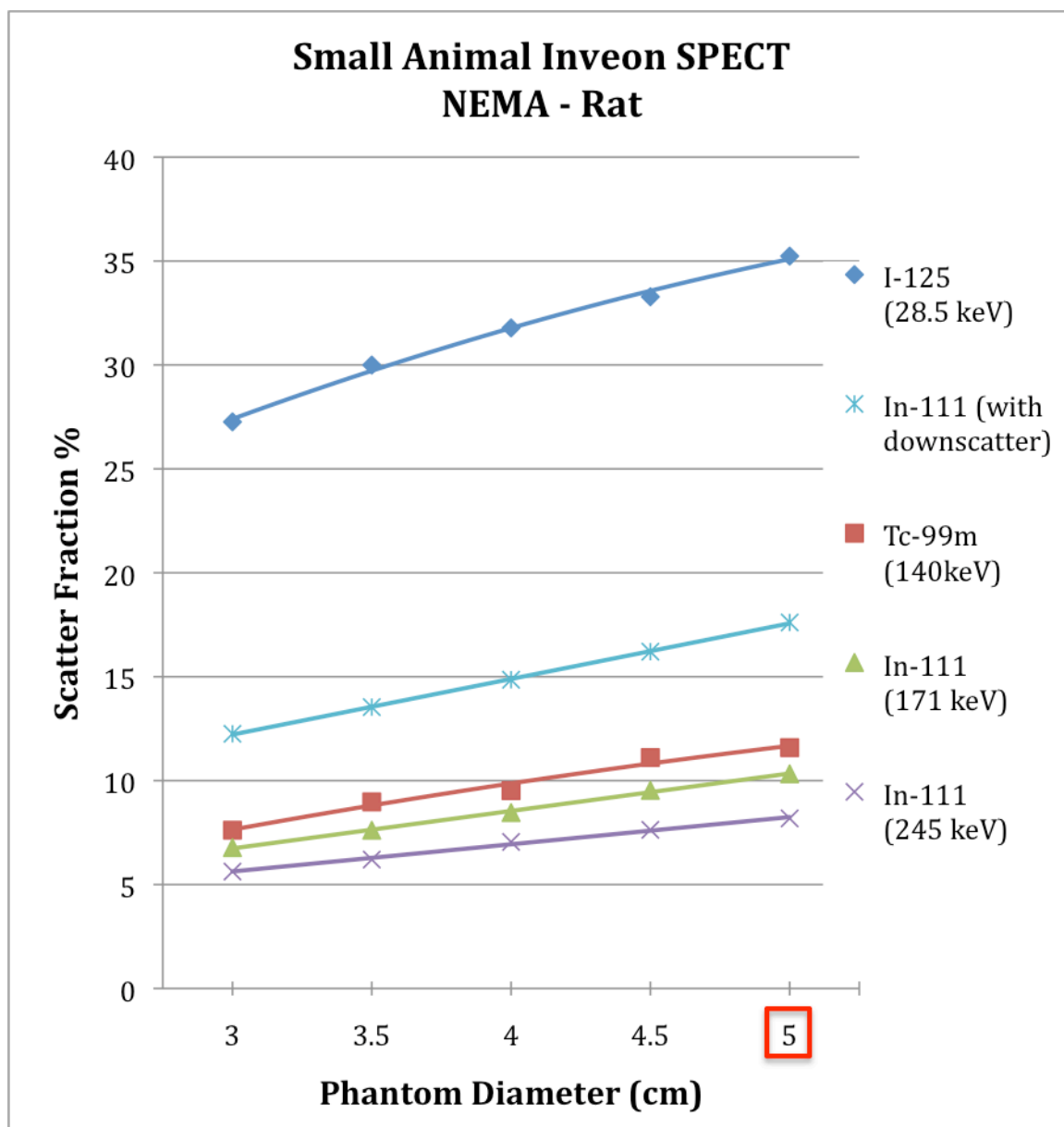
Figure 25 SF % values for different diameters of rat-like NEMA phantoms (15 cm long), where the standard NEMA diameter size is 5 cm. Results are based on the simulations of Siemens Inveon small animal SPECT scanner. An effective emission energy is used for [125]I. SF % for the ^{111}In are presented for 2 separate photopeak windows. SF% for the 171 keV photopeak window (154-188 keV) are shown with and without 245 keV downscatter.

These results were obtained prior to a recent study in which a single ratio of 0.8 (radius to the line-source displacement from the center) for all NEMA phantom sizes was suggested. This implied that our results for human-like NEMA phantoms might have

been overestimated compared to a cylindrical water phantom with homogenous activity distribution; however, this would not significantly change our mouse and rat NEMA results [84].

The NEMA phantom measurements provided scatter fraction estimations for respective sizes of animals and humans. In the next section, we present similar type of measurements for more realistic phantoms modeling small animal and humans.

<div align="center">XCAT and MOBY Phantoms Scatter Fraction</div>

<div align="center">Measurements</div>

XCAT and MOBY are computer-generated phantoms based on real human and mouse anatomies, respectively. Each of these digital phantoms consists of voxelized anatomical data and associated emission data. The implementation of these voxelized phantoms is different than the use of analytical data created within GATE environment, and requires additional work: Prior to performing GATE simulations, the phantoms were created with their default parameters, and the original 32-bit file format was converted into 16-bit since GATE does not support 32-bit format. These image data were then incorporated into the GATE simulation using corresponding header files, which included information such as image size, number of image slice and pixel size. Unlike the analytical sources generated within the GATE environment, the default origin of the voxelized source is not in the center of the coordinate system, but in the 1st quadrant of the image space (world). The voxelized phantom, on the other hand, is created in the center. Therefore, the voxelized source needs to be translated towards the center by half the size of its dimensions on each axis. This translation and other parameters changing with pixel sizes were incorporated in our controlling script.

Ten different sizes of XCAT and six different sizes of MOBY[26] digital phantoms were simulated in the ECAT and Inveon scanners. The scanner acquisition parameters shown in Table 8 were kept the same for XCAT and MOBY simulations. The anatomical data were segmented into 5 different attenuation regions (i.e., air, lung, water, spine bone and rib bone), while the emission data were linearly transformed into radioactivity distributions. The scatter fraction values for an XCAT human phantom (chest FOV) with a fixed height of 180 cm and varying diameter of 21 - 45 cm were measured; as well, the values for the MOBY mouse/rat phantoms of lengths 3.5-10.5 cm and diameters 2.1-6.4 cm were obtained. Figure 22 and Figure 23 show screenshots from small animal PET simulations of the MOBY phantom.

---

[26] 5 sizes are simulated in SPECT due to the limited field of view.
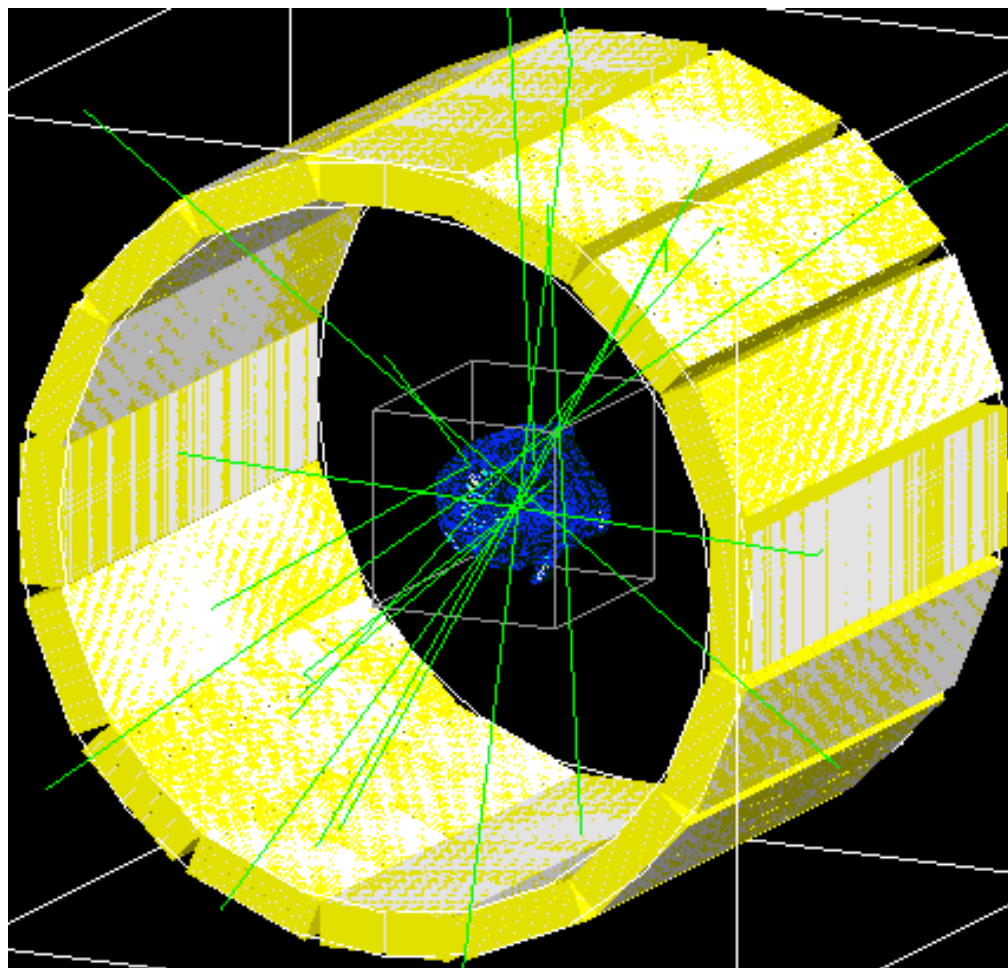
Figure 26 A MOBY phantom (diameter of ~3 cm and length of ~5 cm) is simulated in Inveon small animal PET scanner.
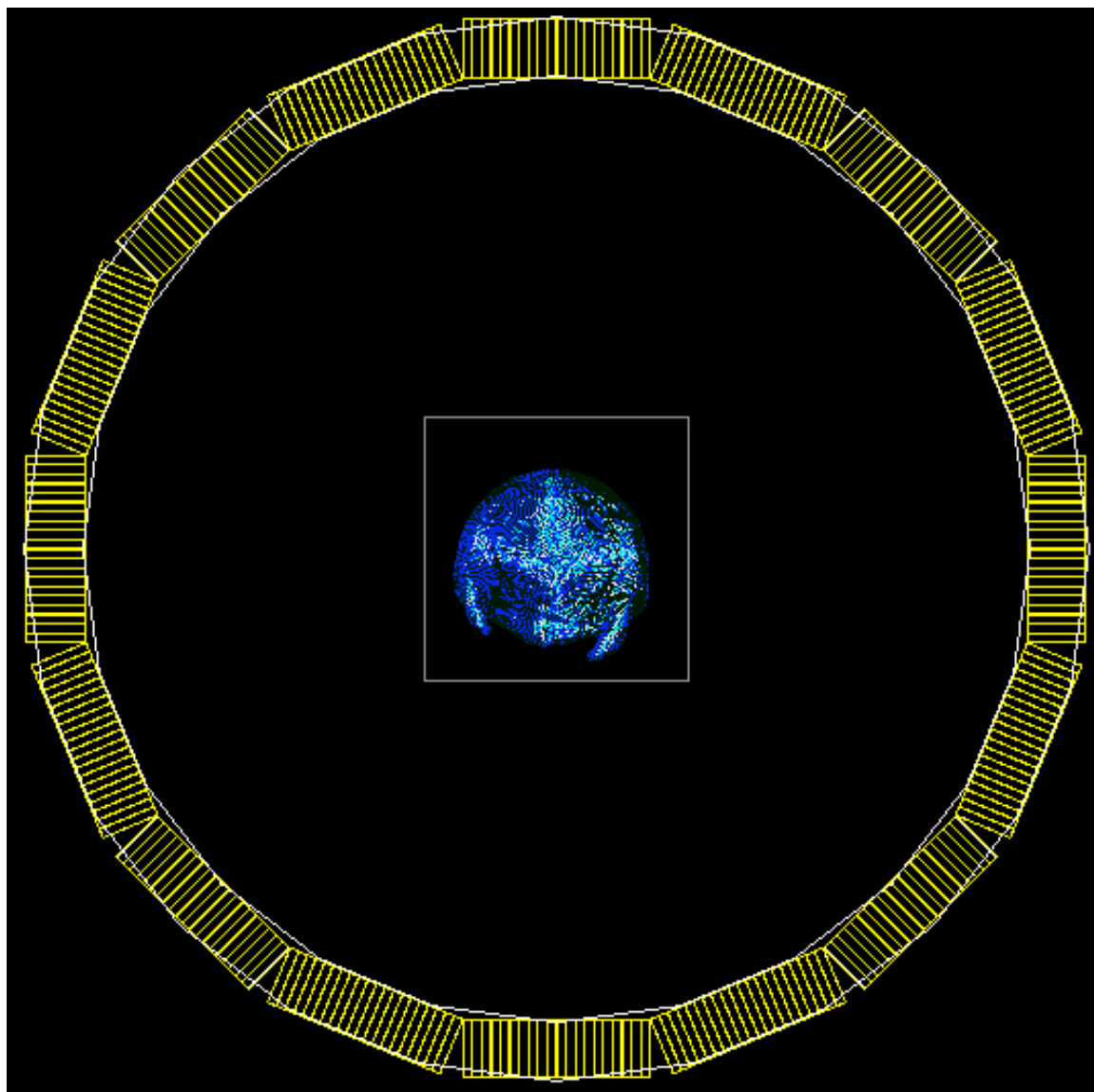
Figure 27 Cross sectional view of the small animal PET scanner: Details of detector blocks and their crystals (1.51 mm wide and 10 mm thick) are shown.

Figure 28 and Figure 29 show screenshots from small animal SPECT simulations of the
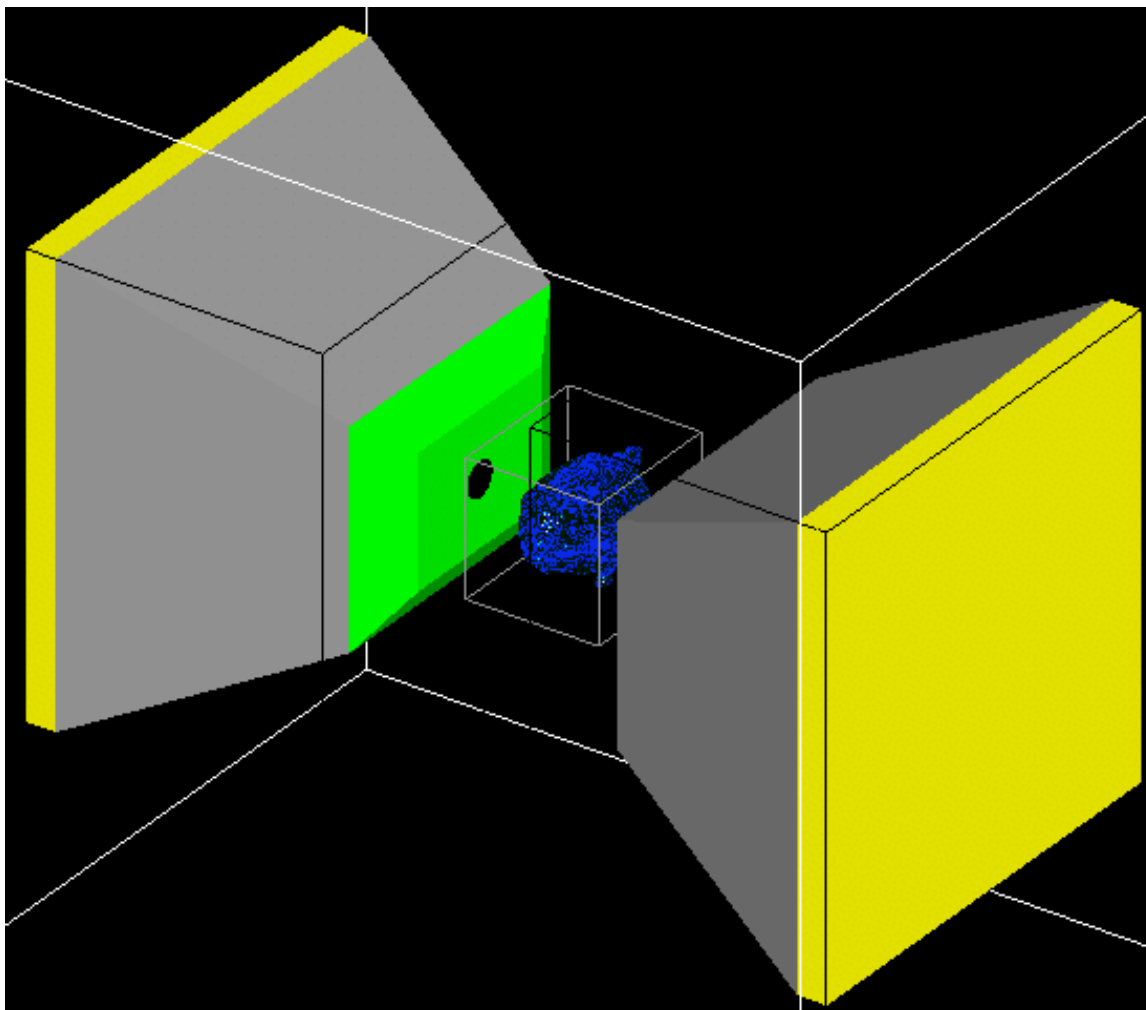
MOBY phantom.

Figure 28 A MOBY phantom (diameter of ~3 cm and length of ~5 cm) is simulated in
Inveon small animal SPECT scanner.
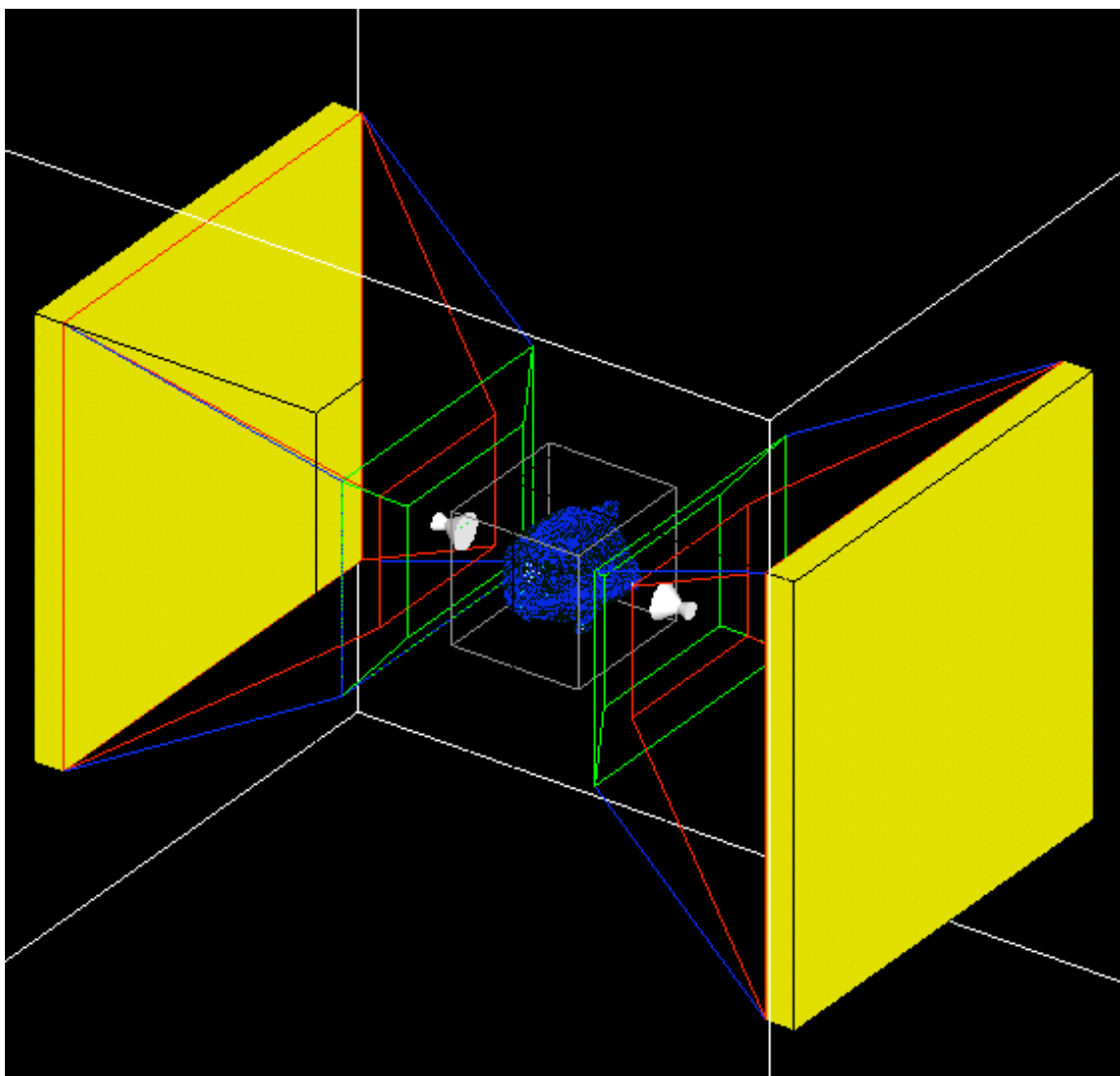
Figure 29 Detailed view of the small animal SPECT scanner geometry. The volume between the red and blue lines represent the lead shield. The region between the shield (red trapezoidal volume) and the detector arrays is defined as air. The pinholes consist of two cones placed back-to-back allowing photons enter into the detector area. Because of the aperture shape photons reach the detector in a cone-beam configuration.

Figure 30 shows a screenshot from ECAT HR+ PET simulations of the XCAT phantom.
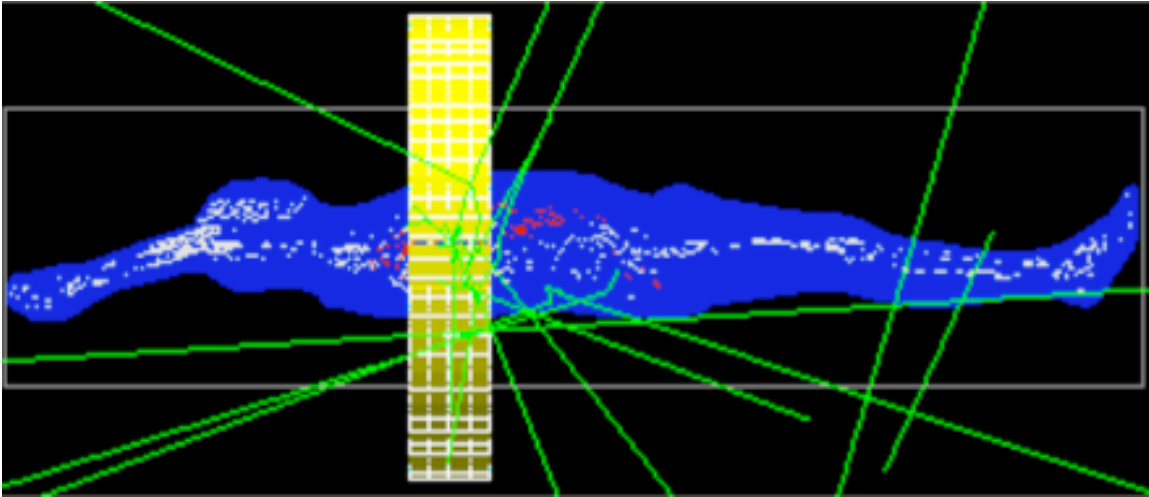
Figure 30 XCAT human phantom simulated in ECAT HR + PET scanner.
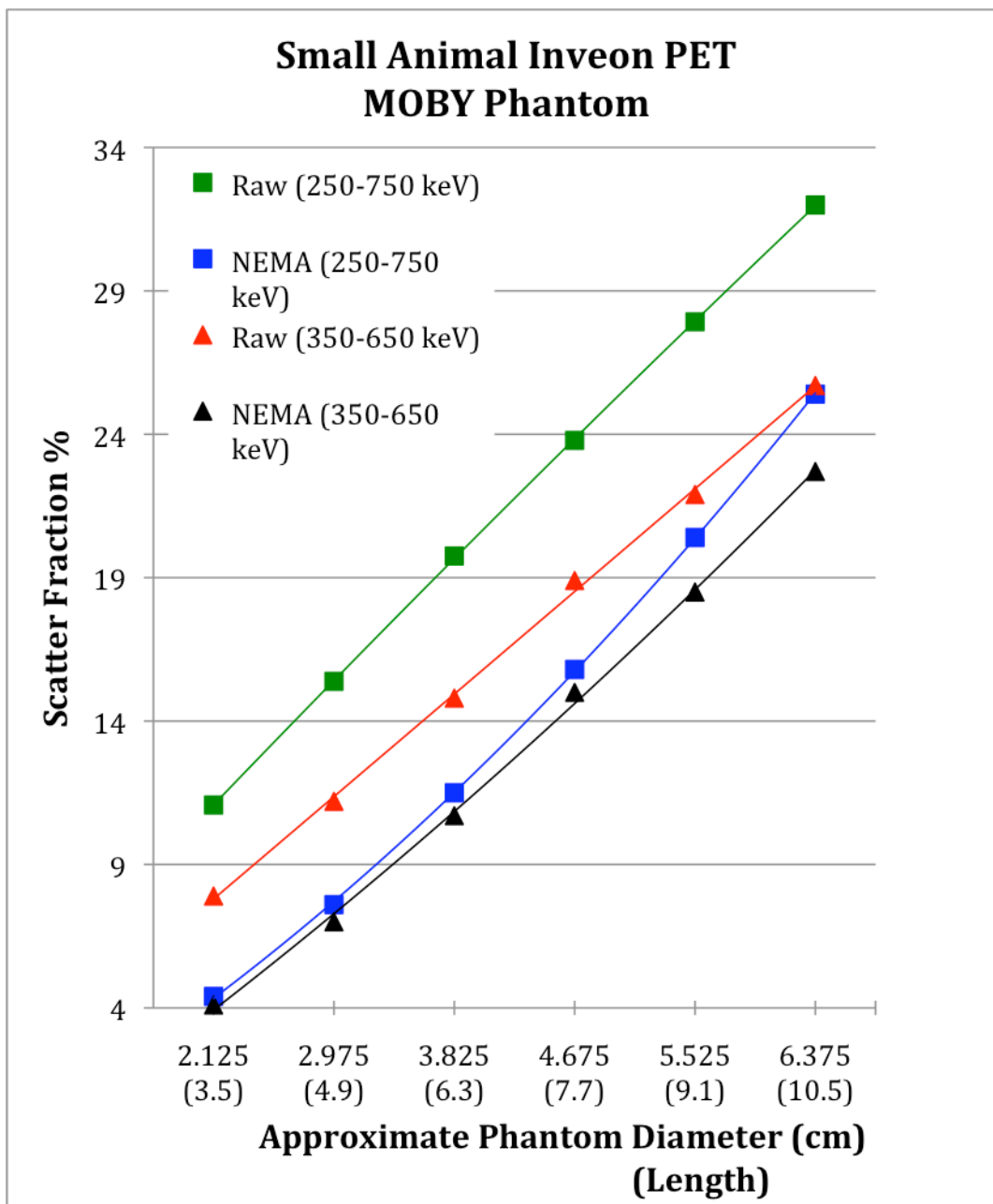
Figure 31 Scatter Fraction % values for different sizes of MOBY phantoms. Results are based on the simulations of Siemens Inveon small animal PET scanner at two different energy windows (square data points represent the 250-750 keV window; triangular points represent the 350-650 keV window). SF values dropped significantly when projections 8 mm outside of the object boundary were set to zero (NEMA procedure).
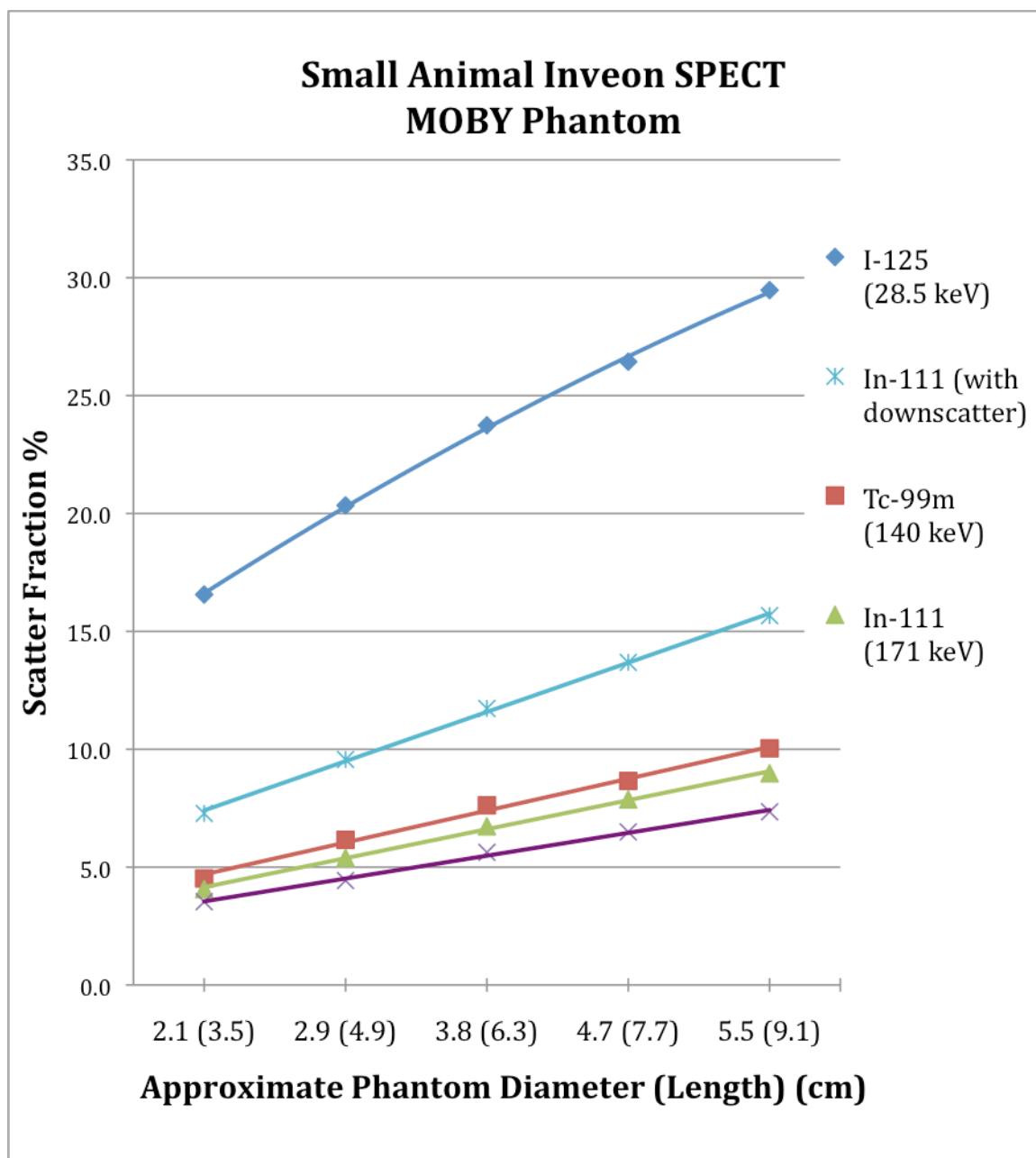
Figure 32 SF % values for 6 different sizes of MOBY phantoms for 3 different SPECT radionuclides. Results are based on the simulations of Siemens Inveon small animal SPECT scanner. An effective emission energy is used for x-ray and γ-ray emissions of the [125]I. SF % for the ^{111}In are presented for 2 separate photopeak windows. SF% for the 171 keV photopeak window (154-188 keV) are shown with and without 245 keV downscatter.
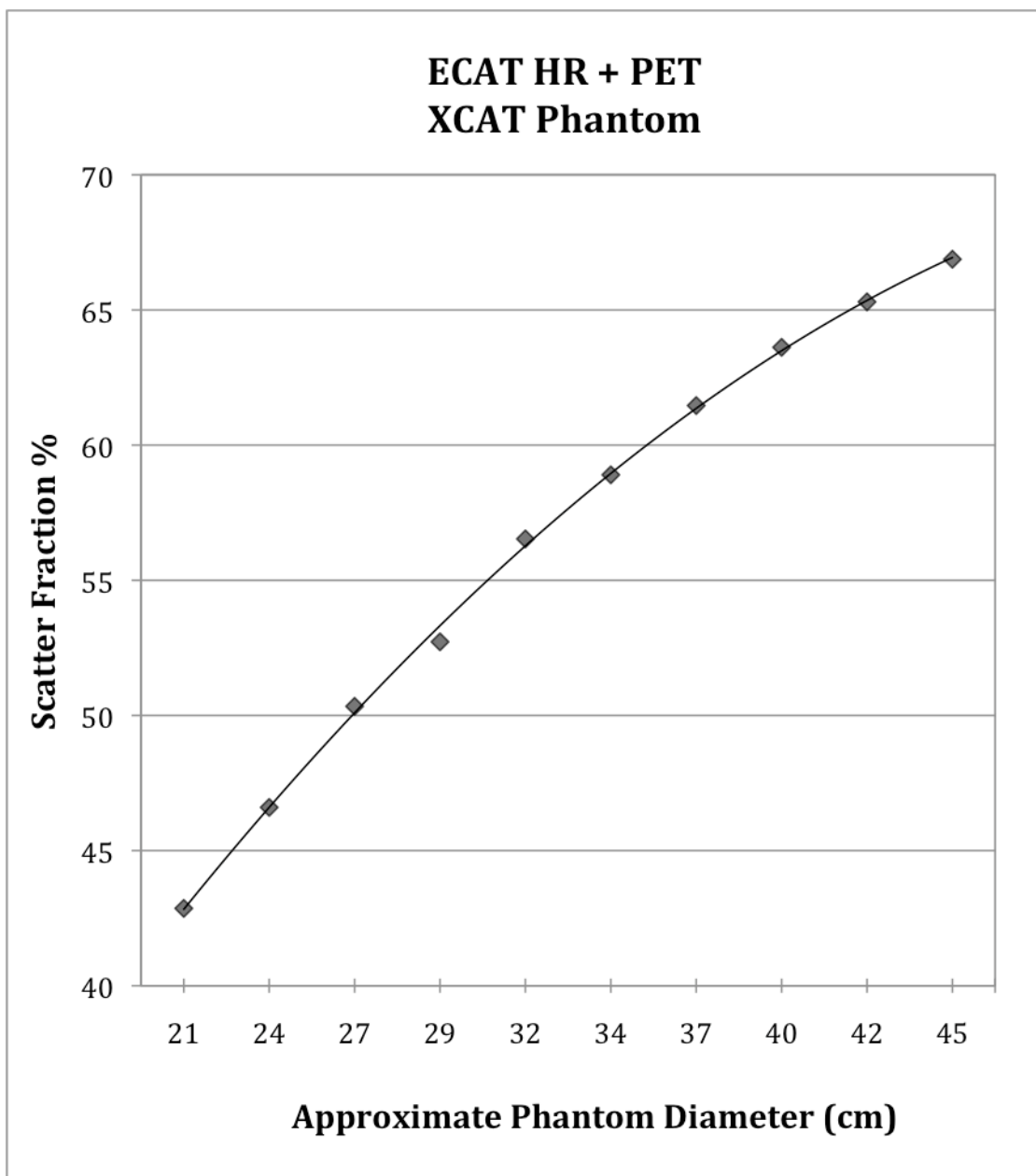
Figure 33 Scatter Fraction % values for different chest diameters of XCAT phantoms. Results are based on the simulations of Siemens ECAT HR+ PET scanner and were obtained from raw data.

<u>Results</u>

The range of scatter fraction values found for MOBY and small animal NEMA phantoms are presented in Table 9.

SCATTER FRACTION %			
PET	**NEMA – Mouse** Diameter: 2-5 cm Length: 7 cm	**NEMA – Rat** Diameter: 3-9 cm Length: 15 cm	**MOBY** Diameter: 2.1-6.3 cm Length: 3.5-10.5 cm
350-650 keV	8.5 – 17.5 4.0 –13.1*	13.6 – 34.1 8.1 – 31.9*	7.9 – 25.7 4.1 – 22.7*
250-750 keV	11.1 – 24.7 3.8 –15.0*	20.8 – 46.6 9.6 – 39.7*	11.1 – 32.0 4.4 – 25.4*
SPECT	**NEMA – Mouse** Diameter: 2-4.5 cm Length: 7 cm	**NEMA – Rat** Diameter: 3-5 cm Length: 15 cm	**MOBY** Diameter: 2.1-5.5 cm Length: 3.5-9.1 cm
^{99m}Tc (140 keV)	3.6 –7.4	7.6 – 11.6	4.5 – 8.7
^{111}In (245 keV)	2.1 – 5.0	5.6 – 8.2	3.5 – 7.3
^{111}In (171 keV) (with downscatter)	3.3– 6.5 7.0 – 13.1	6.8 – 10.3 12.3 – 17.6	4.0 – 9.0 7.3 – 15.7
^{125}I (28 keV)	12.2 – 20.6	27.3 – 35.2	16.6 – 29.5

Table 9   The range of scatter fraction results from Inveon PET and SPECT simulations for corresponding NEMA and MOBY phantom diameters. Values with a * indicate that the counts 8 mm outside the object were removed, as in the NEMA procedure.

The effect of scatter and correction requirement was estimated by the magnitude of scatter fractions for various sizes of phantoms. In the next chapter the effects of scatter and attenuation corrections will be evaluated on the reconstructed images for the same MOBY phantoms.

Discussion

We performed PET and SPECT simulations to measure scatter fraction values for various sizes of NEMA, MOBY and XCAT phantoms. We used two energy windows for PET Inveon simulations. As expected, the wider energy window (250-750 keV) included more scatter counts than the narrow window (350-650 keV). However, when projections 8 mm outside of the object boundary were set to zero (NEMA procedure), the SF values dropped significantly, in particular for smaller objects. Most scatter photons detected in 250-350 keV formed LOR outside of the object boundaries because of larger scatter angles, particularly for smaller object sizes. When these counts are set to zero, most of the scatter originally present in the raw data was removed. For example, after applying this procedure even for the largest mouse size the SF difference between the acquisition obtained by two windows was only ~2%. As the object sizes increased this difference became more significant since additional scatter LORs remained within the object boundaries.

Theoretically, dependence of scatter fraction on object size can be approximated by 1- exp(-μx) [38], where μ is the linear attenuation coefficient (μ_{water}= 0.096 cm^{-1} for 511 keV photons) and x is the total thickness of material which both annihilation photons traverse. For mouse and rat sizes this formula behaves linearly (equation 31) as higher order terms are negligible for small μx values. This is consistent with our results for small animal sizes presented in Figures 21, 22, 24, 25, 31 and 32.

$$1 - \exp(-\mu x) \approx \mu x \tag{31}$$

For human sizes, the scatter follows a non-linear trend because of the larger μx values, as shown in equation 32. This is also consistent with our results from human simulations shown in Figures 23 and 33, where a second order polynomial fit was used.

$$1 - \exp(-\mu x) \approx \mu x - \frac{(\mu x)^2}{2} \tag{32}$$

The SPECT simulations were performed for different photon energies and their respective photopeak windows. As expected, the scatter magnitude was larger for lower energy photons. The impact on the images is expected to be more significant for lower energy photons. In addition, because lower energy photons scatter with larger angles, the images are further distorted.

The SF % obtained from small animal PET simulations were typically higher than that of SPECT, since in PET the probability of scatter is determined by the total path traveled in the object by the two coincident annihilation photons. Although, on average, the scatter angle is larger for SPECT, the impact on images is expected to be less significant since the NaI(Tl) scintillation detectors provide a better scatter discrimination than PET detectors.

Conclusion

Both NEMA and MOBY simulation results for small animal PET using 350-650 keV energy window showed that for rats with diameters up to ~ 6 cm and for all mouse sizes, scatter fraction was less than 20%. When a wider energy window was used (250-750 keV), the scatter fraction was still less than 20% for all mouse sizes and rats with diameters up to ~5 cm. On the other hand, the scatter fractions in small animal SPECT were less than 17.6% for all mouse and rats sizes, except for [125]I. These values are less than the scatter fraction values reported in 2D PET (20%), in which scatter was either ignored or simple scatter correction methods were applied. Therefore, these simulation results suggest that for most small animals up to 5-6 cm in size, scatter correction might not be necessary or scatter correction methods based on emission data alone may be sufficient. In particular, for small animal SPECT imaging energy window based scatter correction methods should be sufficient because of better energy resolution of the detectors and a lower magnitude of scatter.

On the other hand, the scatter fraction for human PET was more than 25% for even the smallest size NEMA (human type) and XCAT phantoms. These studies require more accurate scatter correction methods employing an additional transmission scan.

CHAPTER V

PET SMALL ANIMAL IMAGING: REGION OF

INTEREST MEASUREMENTS

Our IDL simulations of PET and SPECT scanners provided preliminary results for the evaluation of attenuation correction for various sizes of objects, from human to mouse, in the absence of scatter effect. Scatter fraction measurements allowed us to assess the need for scatter corrections. From these results, we concluded that for sizes larger than a rat, more accurate correction methods using an additional transmission scan were required. For this reason, we focused specifically on mouse and rat sizes in this study. In this chapter, we present our analyses of regions of interest (ROIs) on the reconstructed images from GATE simulations and real small animal PET data.

GATE Simulations: ROI measurements

We performed small animal PET simulations (at 350-650 keV energy window) of the same MOBY phantoms used in the scatter fraction measurements, using longer acquisition times to obtain sufficient counts (~20 million) for the reconstructions. Separate prompt (scatter + true) and scatter sinogram files were obtained for the MOBY phantom scaled to six different sizes. Due to the length of simulations, these were split into smaller pieces (typically 20-30 separate jobs) and submitted to different processors, each using an independent random seed. Simulations produced 3D raw sinogram data (160 x 160 x 6400 pixels, 16 bit integer and ~313 Mb size) consisting of direct and oblique sinograms (6400 in total). The sinogram data are organized by the detector ring differences, where the first 80 planes are reserved for the direct sinograms (ring difference of 0) and the next 158 for the absolute ring difference of 1 (starting with +1 and ending with -1 ring differences), and so forth.

Using an IDL code, scatter and prompt sinograms obtained from different processors were summed into one set of scatter and prompt sinogram data for each

phantom size. True sinograms, which represented scatter-corrected projections, were obtained from the difference of the prompt and scatter sinograms. The prompt and true sinograms were then converted into the format of the real Inveon PET scanner (128 x 160 x 4319, 32 bit float). Then, the true and prompt sinogram data were reconstructed using an iterative algorithm, which optionally incorporated attenuation correction, created by Thomas Kösters[27]. Reconstructions were obtained in six different conditions as listed below:

- Accurate attenuation correction and scatter correction (Accurate AC+SC)
- Simple attenuation correction and scatter correction (Water AC+SC)
- Accurate attenuation correction only (Accurate AC)
- Simple attenuation correction only (Water AC)
- Scatter correction only (SC only)
- No correction.

The "simple attenuation correction" used a uniform attenuation map (water attenuation coefficients in the object boundary), and the "accurate attenuation correction" employed actual attenuation coefficient distribution of the MOBY phantom. The scatter-corrected images were obtained from the reconstruction of the true (scatter-free) sinograms.

For attenuation corrected reconstruction conditions, attenuation maps are needed. These were obtained from the original MOBY phantom data and scaled to 6 appropriate sizes (~2.1 - 6.4 cm diameters and 3.5 - 10.5 cm lengths). To do this, we determined the arbitrary size of the MOBY phantom by matching (overlaying and zooming) it with our reconstructed image sets, which differed in size.[28] These attenuation maps were used for

---

[27] A Ph.D. student in mathematics at the European Institute for Molecular Imaging, Muenster, Germany.

[28] We found that the pixel sizes of the smallest and largest size reconstructions were ~3.6 and ~1.2 times smaller than that of the original MOBY phantom, respectively.

the "accurate attenuation correction" of prompt and true sinogram data. For the uniform attenuation correction, the water attenuation coefficient value is used within the same object boundaries.

Using the reciprocal of the same scale factors, all the reconstructed images were scaled to a single size (that of MOBY phantom) to facilitate visual comparison, as in our IDL-based simulations presented in Chapter III. This also allowed us to use the same ROIs for all data sets (6 different sizes) and 6 different reconstruction conditions for each size. We performed our ROI measurements using the image analysis software Amide[29]. In our analyses we assumed reconstructions with accurate attenuation correction of the true sinogram data (i.e., scatter corrected) represented the perfect reconstruction. This was labeled as "accurate AC + SC". The mean error percents of the remaining 5 different reconstructions were calculated against this reference reconstruction.

The 8 ROIs presented here were selected from high (hot) and low (cold) radioactivity regions in different tissues and at various depths. In the following Figures 34 through 41, the mean error percents for highlighted ROIs (boxes, 2D and 3D contours) are presented for the indicated diameter sizes and reconstruction conditions. The transaxial, coronal and sagittal slices shown in these figures were obtained by overlaying the MOBY analytical phantom and its corresponding reconstructed images. The labels R (right), L (left), P (posterior) and A (anterior) show the orientation of these slices.

In these figures, positive errors indicate underestimation and negative errors indicate overestimation of the radioactivity in a given region. A summary of these results is given at the end of this chapter.

---

[29] Amide is a free medical image analysis software that available for major operating systems such as Linux, Mac and Windows.
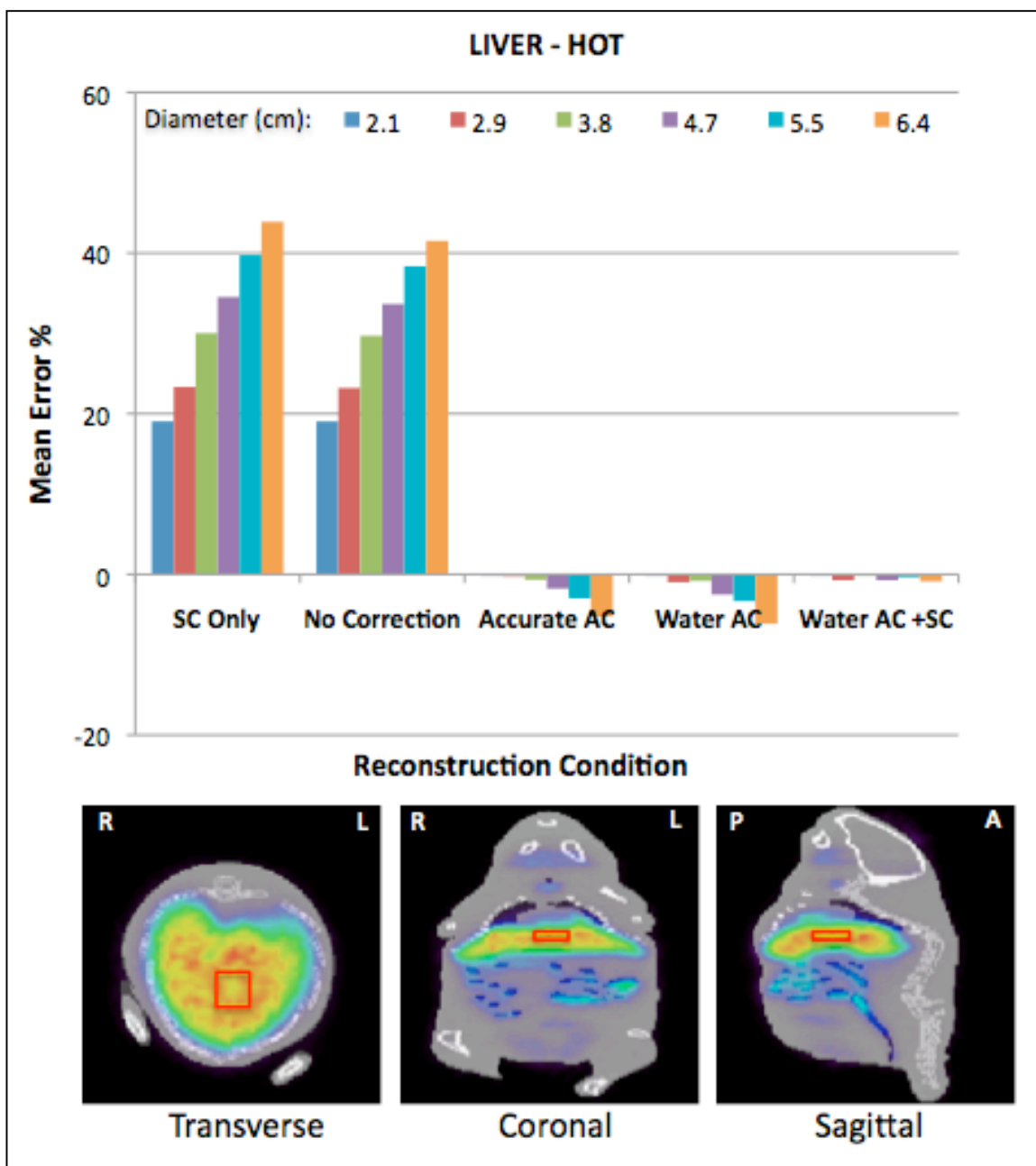
Figure 34 Mean error percents for the ROI (red box) in the liver for different phantom sizes. In this region, the attenuation coefficient of the MOBY phantom was 0.096 cm^{-1} and its corresponding activity level was 75 (unitless). Even for the smallest-sized phantom, the error percent was 19% when attenuation was not corrected. When AC was performed, the error percent dropped below 1% for sizes up to 3.8 cm diameter. The additional SC decreased the error for larger sizes below 1%, as well.
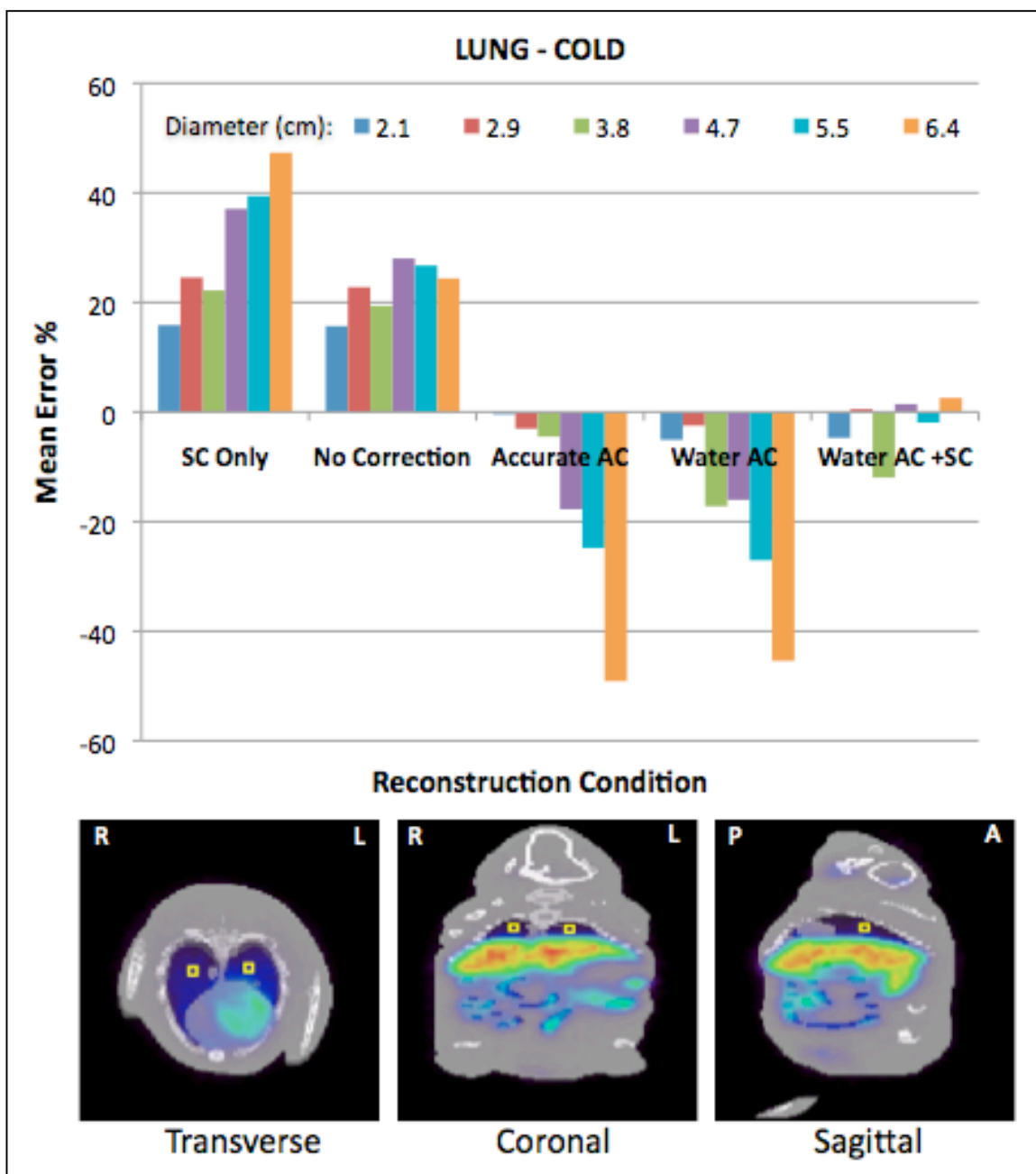
Figure 35 Mean error percents for the ROIs (yellow boxes) in the lungs. . In this region, the attenuation coefficient of the MOBY phantom was 0.035 cm^{-1} and its corresponding activity level was 4 (unitless). The error values did not follow a regular increasing trend with sizes. When only AC was performed the smallest 2 sizes for "water AC" and smallest 3 sizes for "accurate AC" had significant improvement. For other sizes, the error percents were close to that of without AC. In addition, "water AC + SC" significantly improved the error.
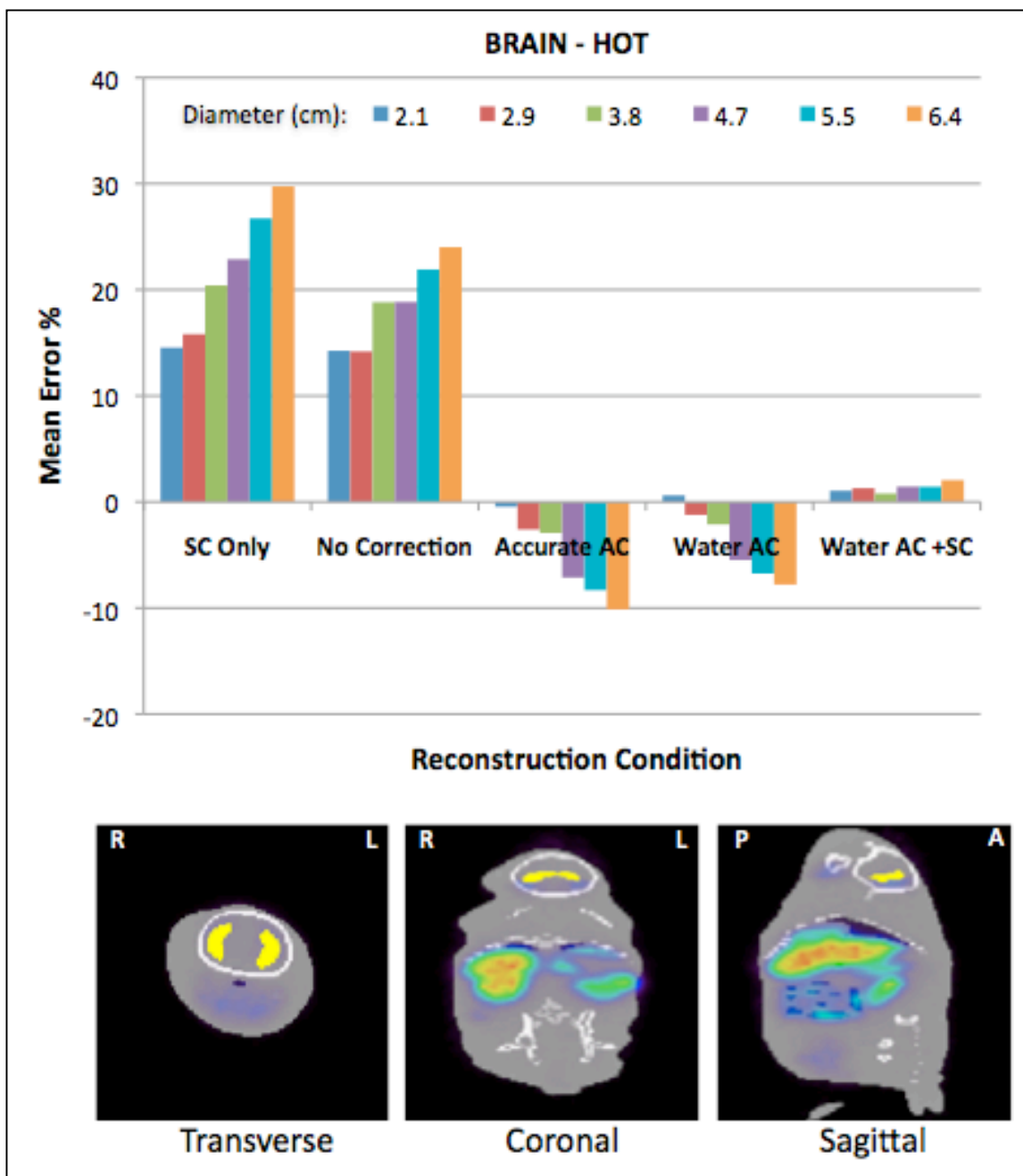
Figure 36   Mean error percents for the ROI (yellow 3D contour) in the brain. In this region, the attenuation coefficient of the MOBY phantom was 0.096 cm^{-1} and its corresponding activity level ranged between 25 - 40 (unitless). For the smallest size phantom, the error percent was 14% when attenuation was not corrected. Whereas when AC was performed the error percent was below 5% up to 3.8 cm diameter. The additional SC decreased the error for even larger sizes to 2% only.
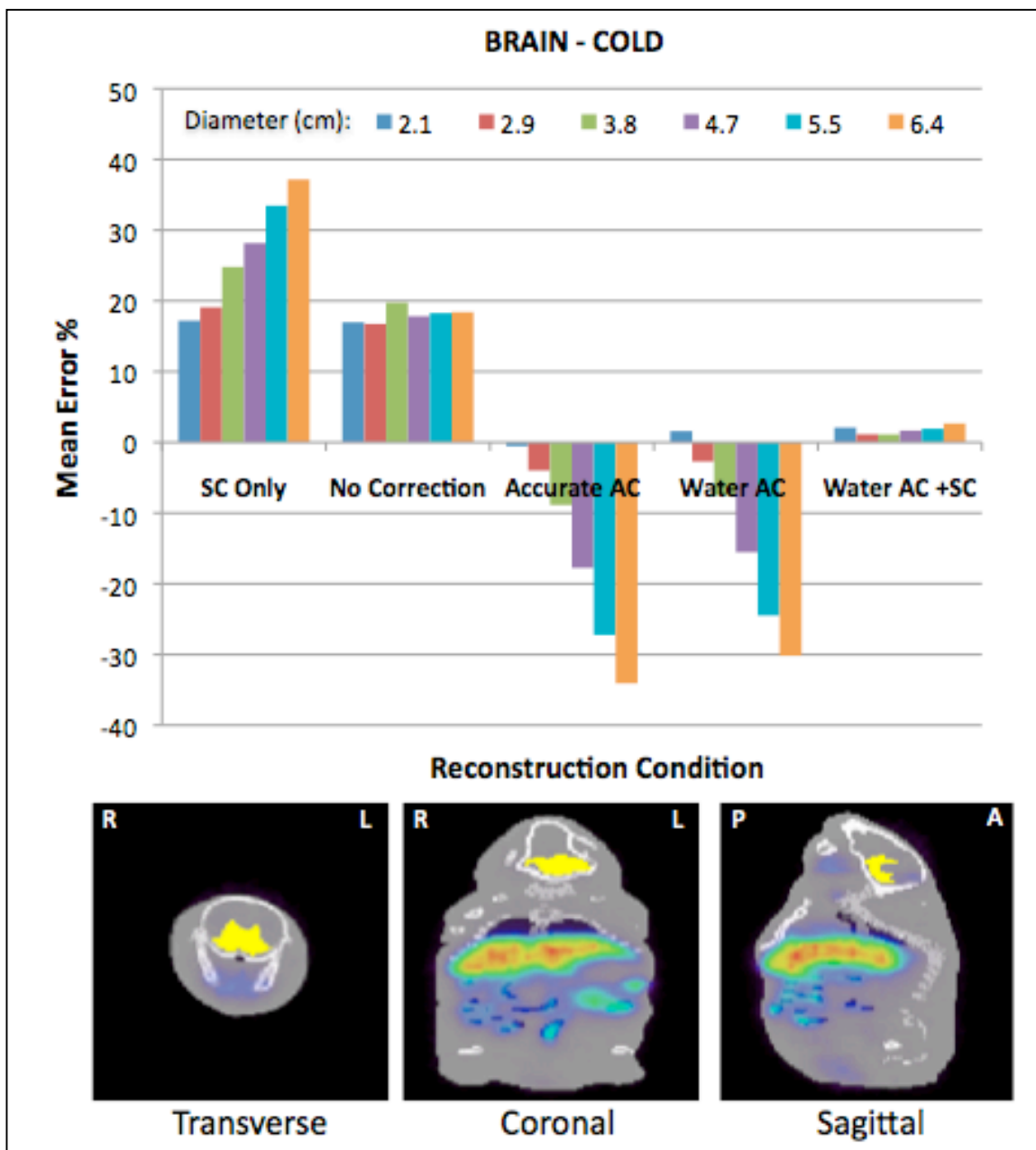
Figure 37 Mean error percents for the ROI (yellow 3D contour) in the brain. In this region, the attenuation coefficient of the MOBY phantom was 0.096 cm^{-1} and its corresponding activity level was 5 (unitless). Compared to hot ROI in the brain, cold ROI had higher error percents for all correction methods. When AC was performed the error percent was 9% for 3.8 diameter size and the additional SC decreased the error to 2.5%.
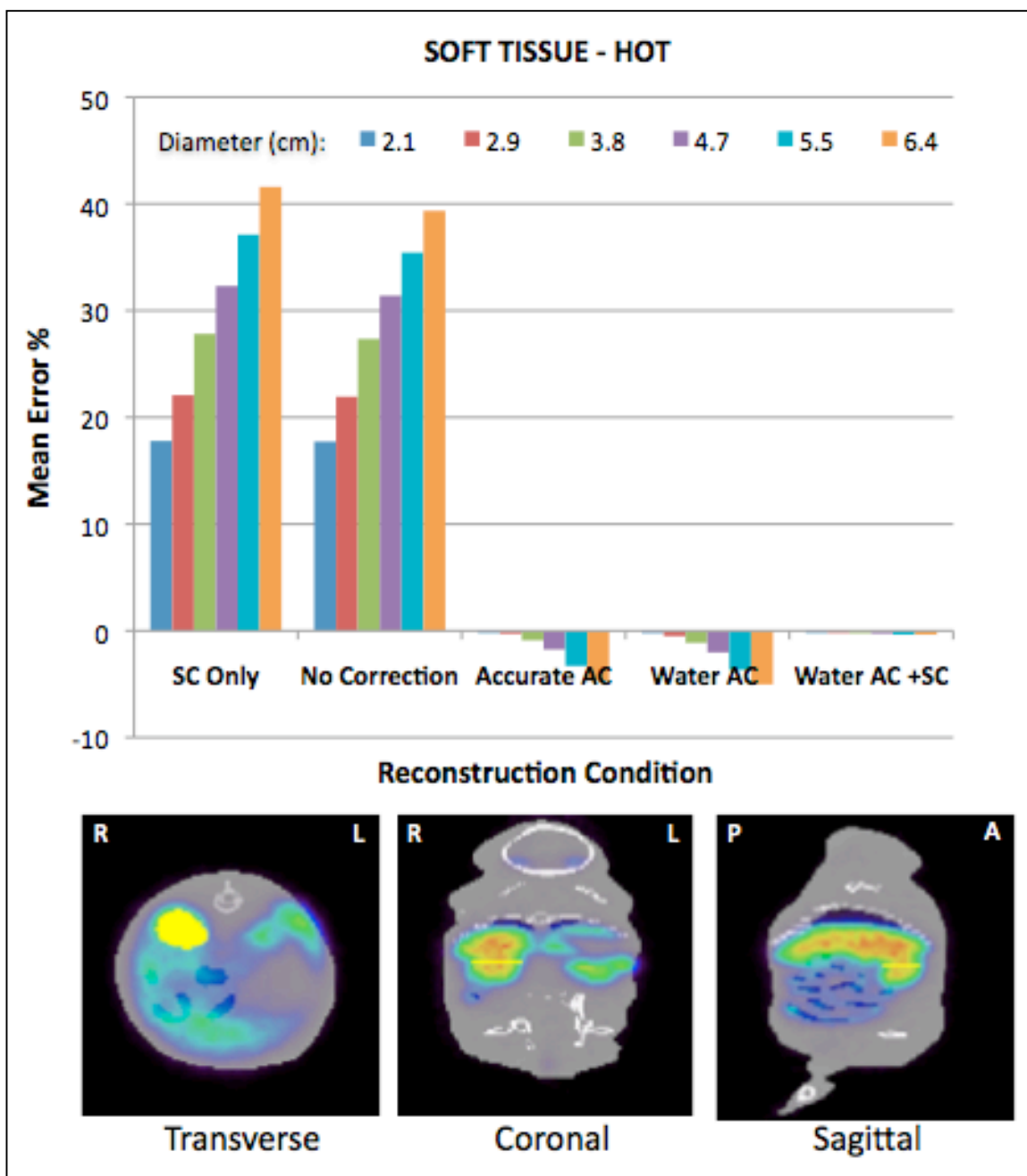
Figure 38 Mean error percents for the ROI (yellow 2D contour) of a soft tissue. In this region, the attenuation coefficient of the MOBY phantom was 0.096 cm^{-1} and its corresponding activity level was 75 (unitless). The errors increased regularly with the increasing phantom size. For the smallest size phantom, the error percent was 18 % when attenuation was not corrected. Whereas when AC was performed the error percent was 5% even for the larges size phantom. The additional SC decreased the error to below 0.4%.
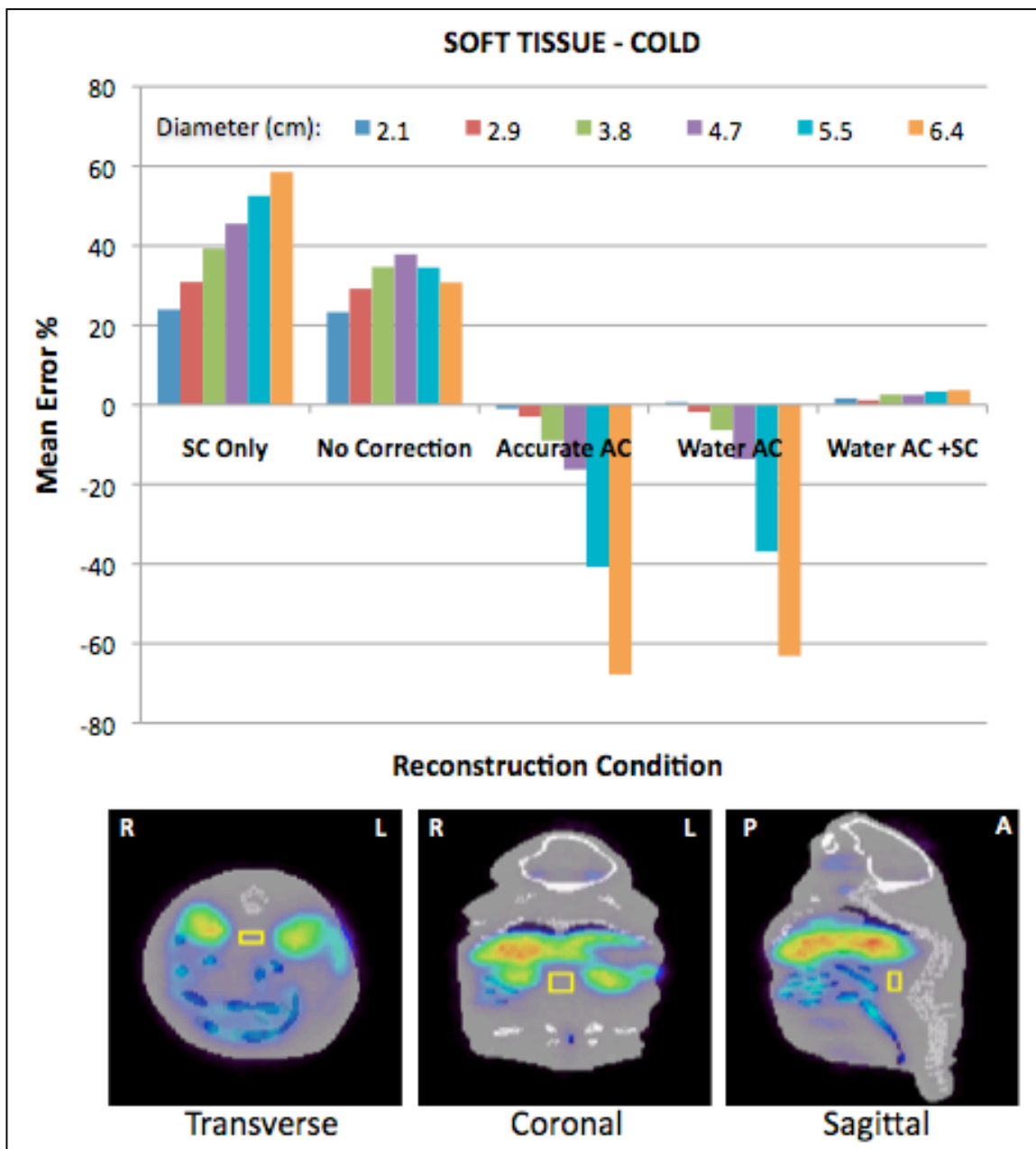
Figure 39 Mean error percents for the ROI (yellow box) of a soft tissue. In this region, the attenuation coefficient of the MOBY phantom was 0.096 cm^{-1} and its corresponding activity level was 2 (unitless). When a correction performed the errors increased regularly with the increasing phantom size. For the smallest size phantom, the error percent was 22% when attenuation was not corrected. When AC was performed the error percent was below 3% up to 2.9 cm diameter. The additional SC decreased the error to below 4% even for the largest size phantom.
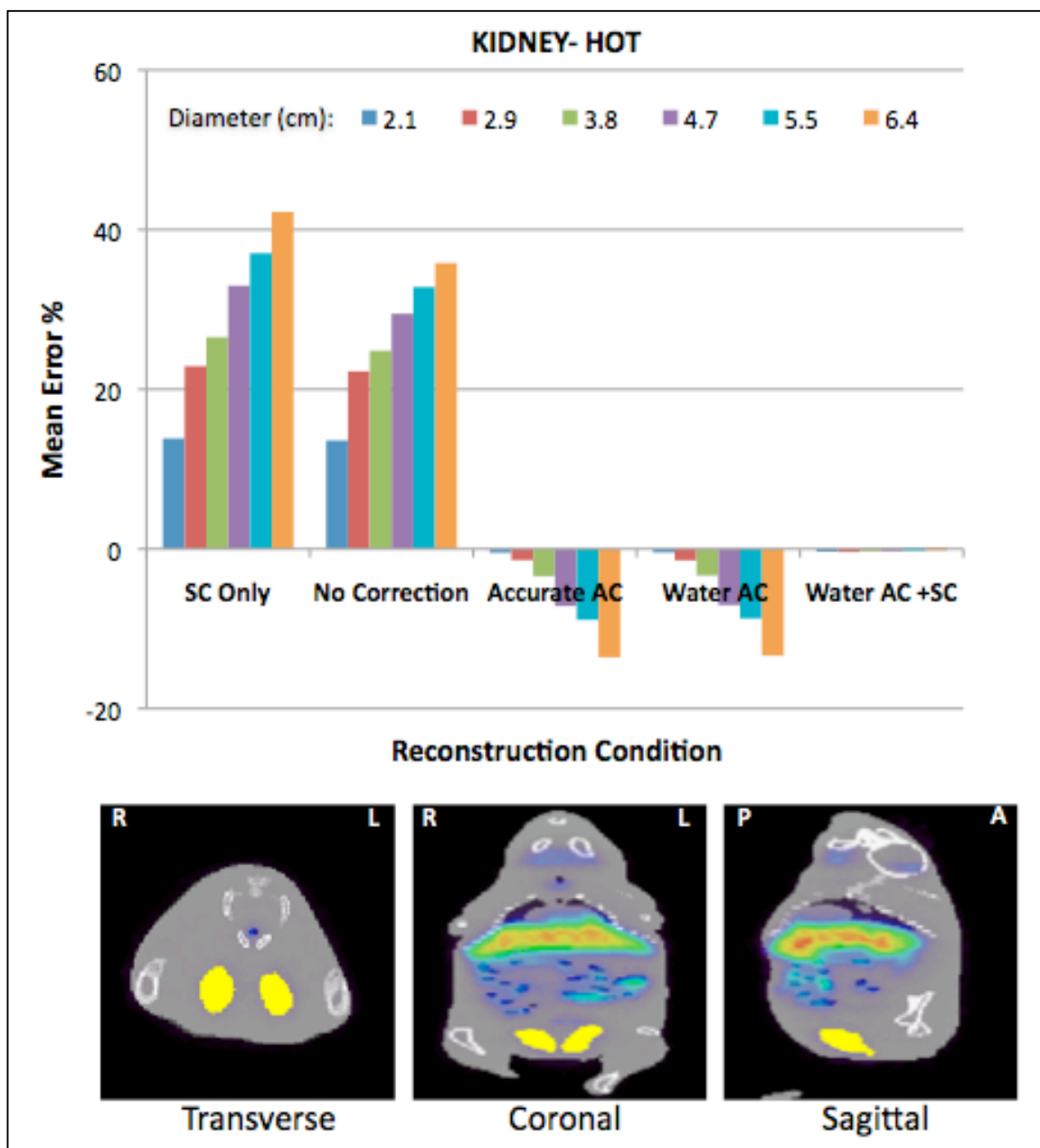
Figure 40 Mean error percents for the ROIs (yellow 3D contours) of the kidneys. In this region, the attenuation coefficient of the MOBY phantom was 0.096 cm^{-1} and its corresponding activity level was 15 (unitless). The errors increased regularly with the increasing phantom size. For the smallest size phantom, the error percent was 14% when attenuation was not corrected. Whereas when AC was performed the error percent was less than 3.5% up to 3.8 cm diameter phantom. The additional SC decreased the error to below 0.2%.
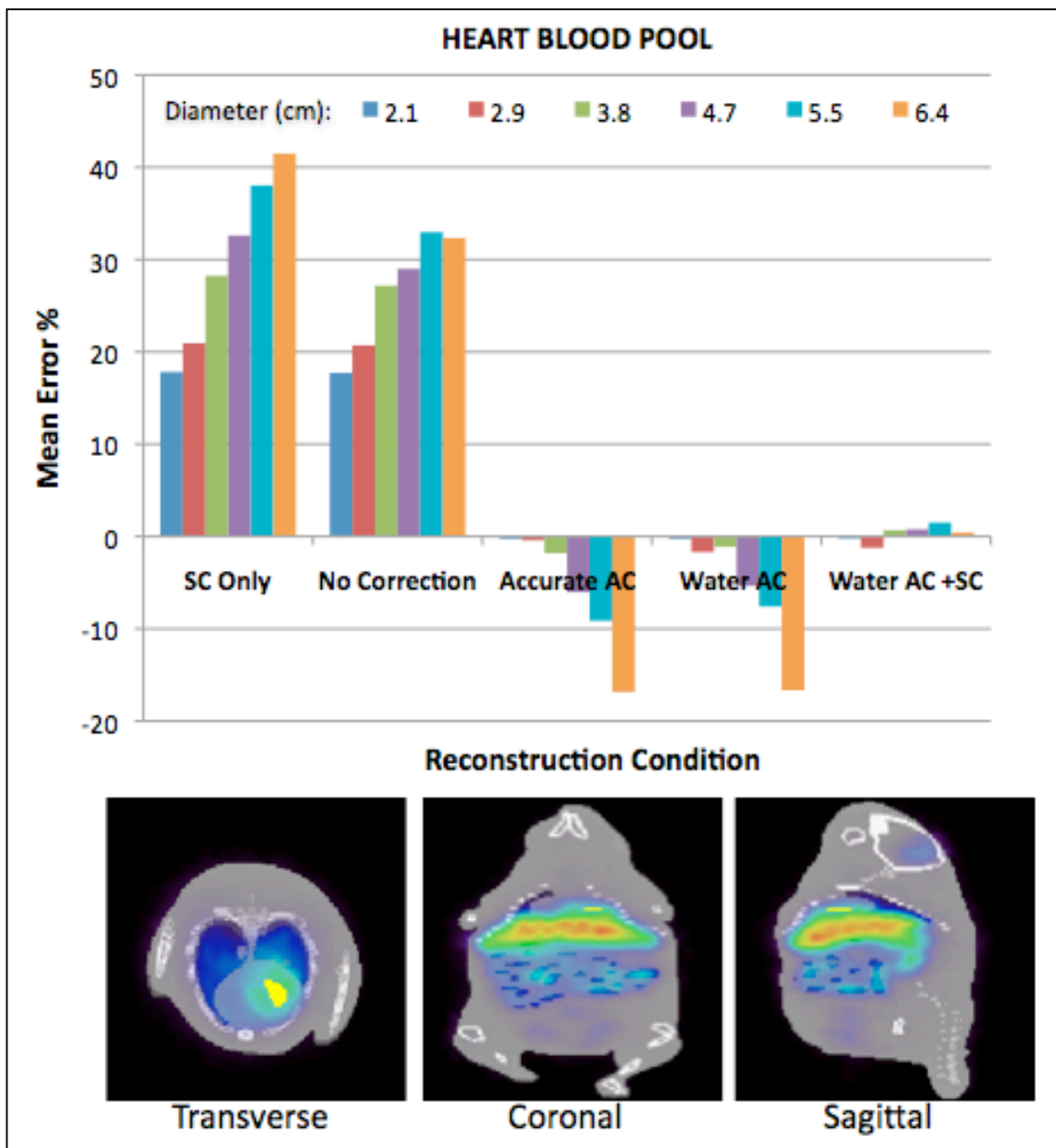
Figure 41 Mean error percents for the ROI (yellow 3D contour) of the heart blood pool. In this region, the attenuation coefficient of the MOBY phantom was 0.096 cm^{-1} and its corresponding activity level was 2 (unitless). The errors increased regularly with the increasing phantom size. For the smallest size phantom, the error percent was 14% when attenuation was not corrected. Whereas when AC was performed the error percent was less than 3.5% up to 3.8 cm diameter phantom. The additional SC decreased the error to below 1.5% for all sizes.

Real Data: ROI Meaurements

The University of Iowa Hospital and Clinics (UIHC) recently acquired an Inveon small animal scanner system[30], which has the same PET and SPECT components modeled in our GATE simulations. The 3D sinogram data from an existing mouse study were reconstructed with and without corrections following similar approaches applied in the GATE simulation work.   The sinogram data were reconstructed using a 3D reprojection algorithm [87] with the following conditions:

- Accurate attenuation and scatter correction using attenuation maps obtained from CT transmission data (Accurate AC + SC)

- Uniform attenuation correction and scatter correction (Water AC + SC)

- Uniform attenuation correction only (Water AC)

- Accurate attenuation correction only (Accurate AC)

- No correction (NC).

The first condition in this list is considered as the reference reconstruction. Mean values of ROIs from the rest of the conditions were compared to the reference reconstruction. Unlike the previous section, the SC only was not an available option in the Inveon reconstruction software.

The PET acquisition for this study was performed at a 350-650 keV energy window, as in our simulation work.   An additional CT transmission scan was also acquired using the MicroCAT™ II tomograph built in the PET/CT/SPECT multimodality system (Siemens Preclinical Solutions, Knoxville, TN). The transmission data were employed in both "accurate" attenuation and scatter corrections. The scatter correction was based on the single scatter counts, which incorporated both emission and CT transmission data in the Klein-Nishina equation. The uniform attenuation correction was

---

[30] The Inveon small animal is a combined PET/CT/SPECT small animal scanner, allowing PET/CT and SPECT/CT studies on the same platform

performed using a mouse size cylindrical phantom with the water attenuation coefficient (0.096 cm^{-1}). The mean error percents for various regions for this mouse (~2.7 cm diameter and ~7.8 cm long) were calculated. The results are presented with respect to reconstruction conditions and regions in Figures 42 and 43, respectively. In addition, ROIs are shown for selected reconstructed image slices in Figure 44.
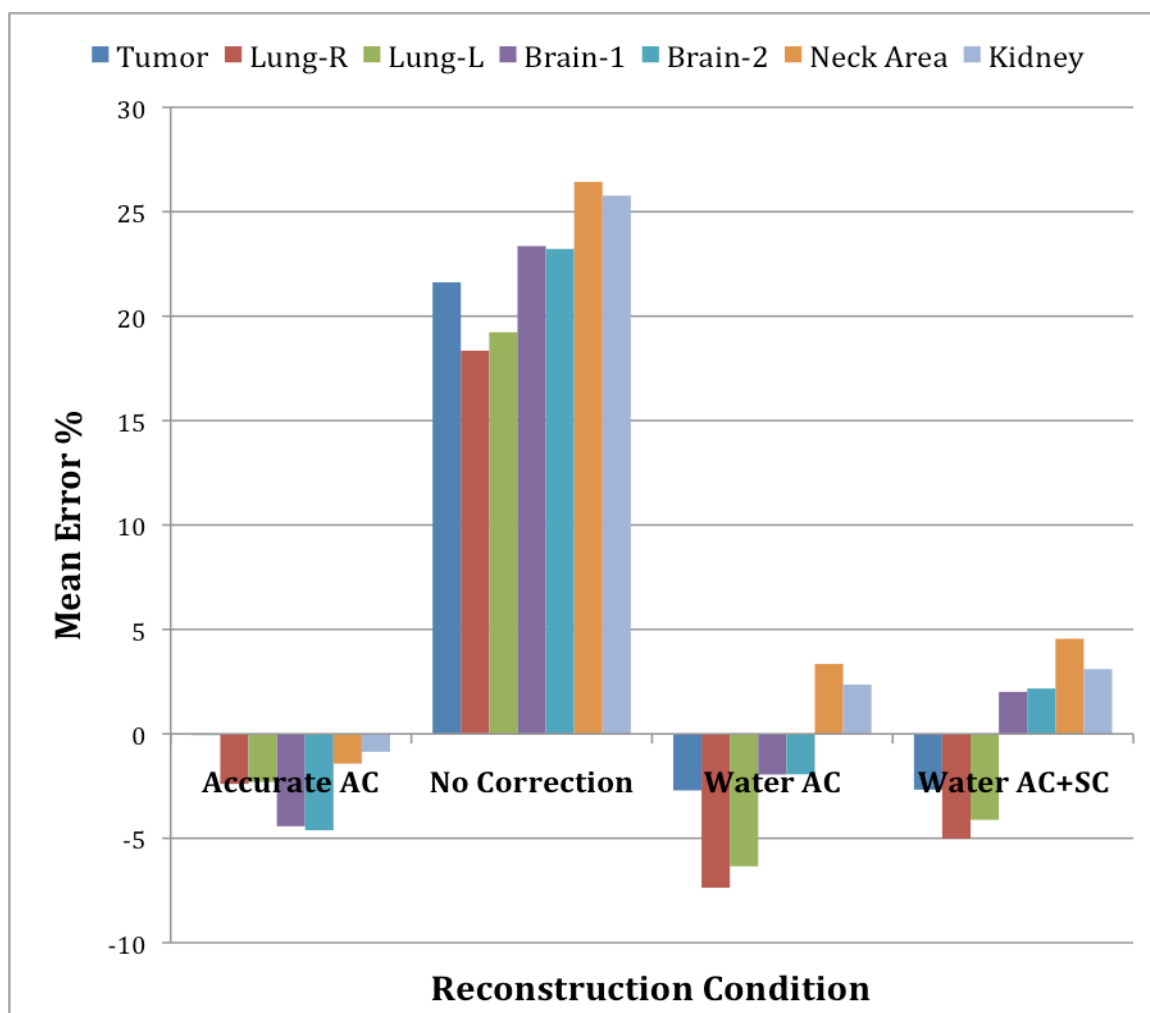
Figure 42 Mean error percents for various ROIs and correction conditions for a real mouse (2.7 cm diameter and 7.8 cm long). Without any correction, the smallest error was 18% (Lung). When attenuation correction was applied, the error was below 7% for all regions.
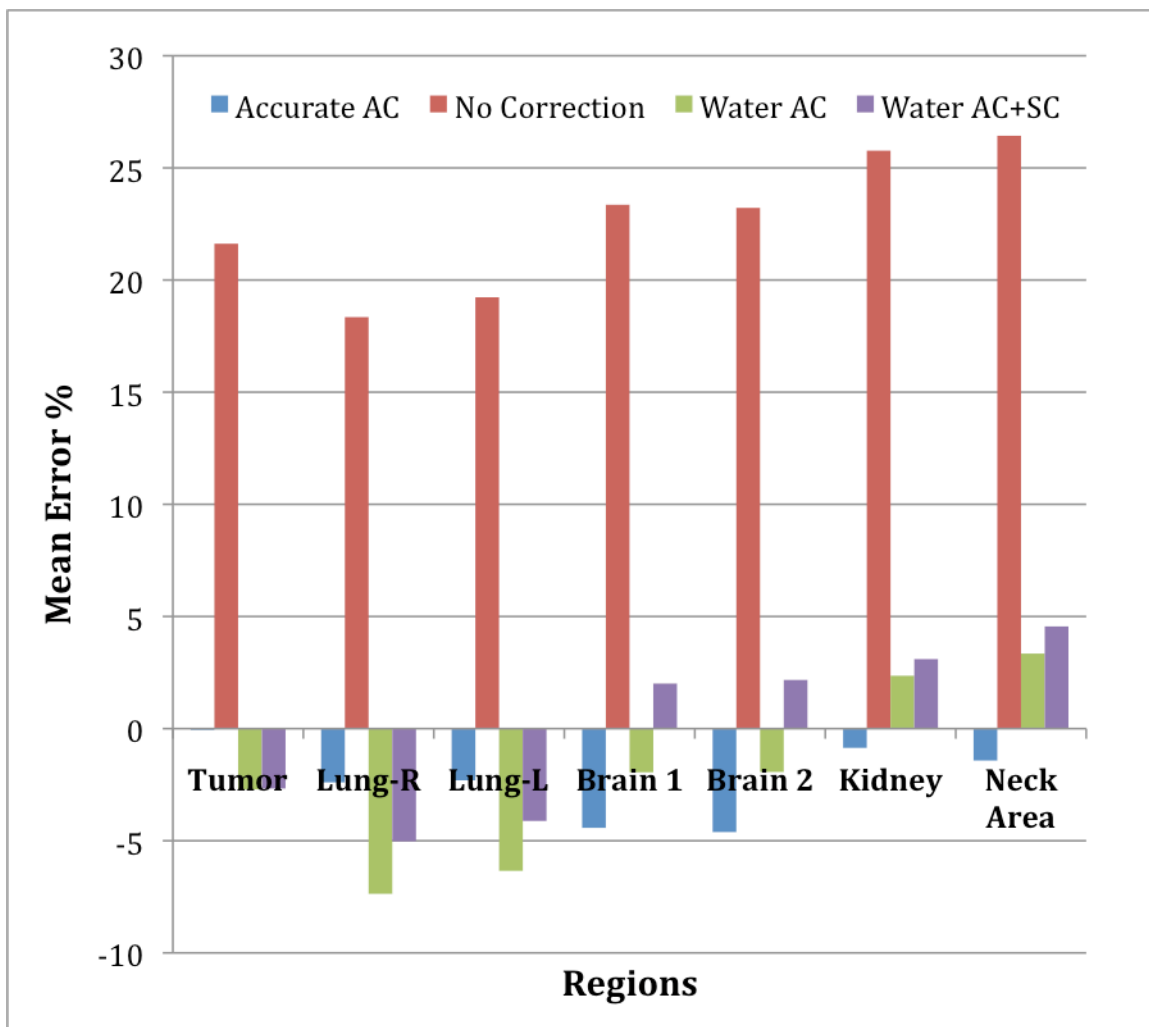
Figure 43 Mean error percents for various ROIs and correction conditions for a real mouse (2.7 cm diameter and 7.8 cm long). The maximum error was 7% (lung-R) when a correction was performed.
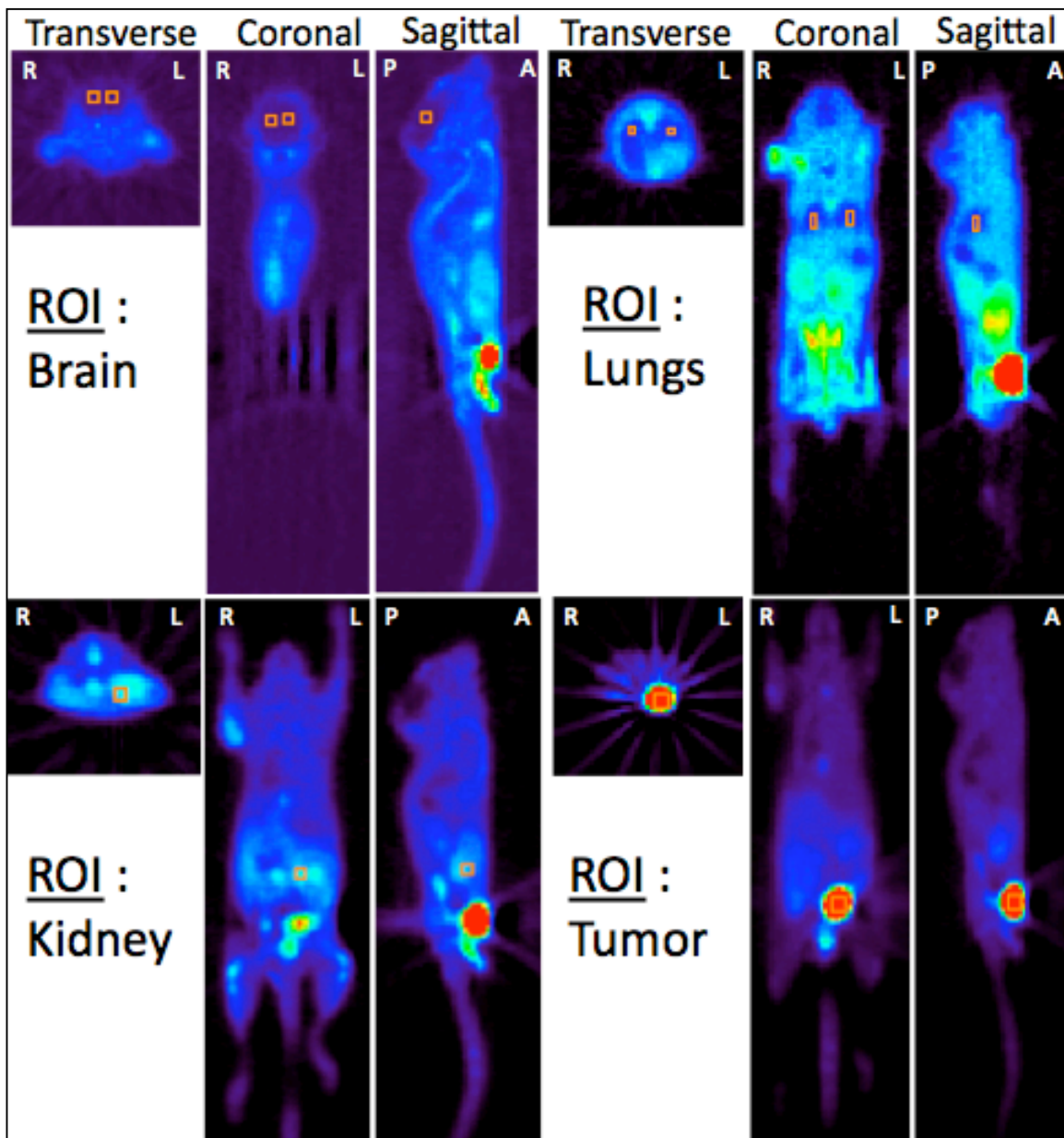
Figure 44 ROIs (boxes) of the real mouse data shown for selected slices in transverse, coronal and sagittal views. As can be seen in these images the ROIs of kidney and tumor were hot, whereas the lung and brain were cold. The orientation of these slices is indicated with letters R (right), L (left), P (posterior) and A (anterior).

Results

      The mean error percents were calculated for various ROIs in the selected reconstruction slices of 6 different sizes of MOBY phantoms and for real mouse data. The results from both GATE simulations of MOBY phantoms and the real mouse data for the respective regions and reconstruction conditions are summarized in Table 10. We found that even for the smallest sized MOBY phantom (2.1 cm diameter), the error percent was at least 14% when no correction was performed. When only uniform attenuation correction (labeled as water AC) was performed, the quantitative accuracy dramatically improved, particularly in hot regions (as indicated in Figures 34- 41 and 44). For hot regions, error percentages decreased to less than 3% and 7% for sizes smaller than ~ 4 and ~ 5 cm, respectively. As a specific example, an error of 41% in the liver (hot) was reduced to 6% for the largest MOBY phantom (6.4 cm diameter). Likewise, in the real mouse data (~2.7 cm diameter), the 22% error measured in the tumor (hot) region dropped to 3% when attenuation correction was applied. Performing AC in cold regions was less effective overall, although for sizes smaller than ~3 cm and ~4 cm the errors were still less than 4.5% and 9% for all regions, respectively. These findings are consistent with the literature [64] [72] [88].

      Additional scatter correction significantly reduced the errors in the simulation study. Even for the largest sizes, all the regions in the MOBY phantom showed less than 4% error after further correction (i.e., water AC+SC). However, in the real mouse data, additional scatter correction did not provide a significant improvement; the only correction of note was an approximate ~2% error reduction in the lung regions.

      When only scatter correction was applied without attenuation correction, the errors increased for both MOBY phantoms and the real mouse compared to when correction was not performed at all.

MOBY DATA: MEAN ERROR %					
ROIs ⇓	SC only	NC	Accurate AC	Water AC	Water AC + SC
Kidney-Hot	14-42	14-36	0-13	0-13	0
Lungs-Cold	15-46	15-18	0-60	7 - 60	0-17
Brain-Hot	14-30	14-24	0-10	0-8	0-2
Brain-Cold	17-37	17-20	0-34	2-30	1-3
Soft Tissue-Hot	18-42	18-39	0-5	0-5	0
Soft Tissue-Cold	24-58	23-31	1-68	6-63	1-4
Liver-Hot	19-43	19-41	0-5	0-6	0
Heart-Cold	18-41	18-33	0-17	0-17	0-2
REAL MOUSE DATA: MEAN ERROR %					
ROIs ⇓	SC only	NC	Accurate AC	Water AC	Water AC + SC
Kidney	N/A	26	1	2	3
Lungs	N/A	19	2	7	5
Brain	N/A	23	4	2	2
Tumor	N/A	21	0	3	3
Neck Area	N/A	26	1	3	4

Table 10 Approximate mean error percents for various ROIs of simulations and real mouse data. Absolute error values are shown. The error range shown for the MOBY phantoms includes all phantom sizes (2.1-6.4 cm diameter and 3.5-10.5 cm length). The real mouse was 2.7 cm in diameter and 7.8 cm long.

Discussion

The level of requirement of attenuation and scatter correction in small animal PET imaging was evaluated based on ROI analysis of the MOBY phantoms and real mouse data. The results of this study can be used in determining the correction method for a particular study.

When only attenuation correction is performed, the emission values are overestimated (negative error); extra counts from scatter were amplified. The error was more significant for larger sizes, particularly in the lungs ($\mu = 0.35$ cm^{-1}). For this reason, scatter correction is applied prior to attenuation correction. If scatter correction is not going to be performed, a broad-beam attenuation coefficient (a lower value than narrow beam attenuation coefficient) can be used [89]. On the other hand, when attenuation correction is not performed (i.e., "No correction" and "SC only" conditions), the emission values are underestimated (positive error). In addition, errors with "SC only" were higher than when not performing any correction. In fact, performing only scatter correction is not an available option in the reconstruction software of the Inveon PET scanner.

In the simulation study, attenuation corrections (accurate AC and water AC) resulted in overestimation of the activities for all regions. However, in the real mouse there was underestimation for the kidney and neck areas. These different behaviors can be attributed to the different methods applied for the corrections. In the MOBY phantom study the boundaries of the attenuation maps were more accurate for both types of attenuation corrections. The attenuation coefficients representing soft tissue and water in the anatomical MOBY phantom and the values chosen for the uniform attenuation correction were identical. In contrast, in the real mouse study, the attenuation map for "water AC" was approximated by a uniform cylinder. Unlike the MOBY phantom, the activity distributions and the tissue densities were more heterogeneous. As well, the constant value chosen for the uniform attenuation coefficient does not necessarily reflect the most proper value in the real mouse study.

Another concern to be addressed regards the error trend and size relationship. Although for a given reconstruction condition and ROI most error values followed an increasing trend with sizes (as expected), there were exceptions in certain regions. One explanation would be related to imperfect scaling factors that we obtained manually by overlaying and zooming the reconstructed images. Therefore, our attenuation maps were not perfectly aligned with the reconstructed images by visual inspection. In addition, the reconstructions of different sizes were rescaled to a single size (that of the MOBY phantom) in order to use the same ROIs for all sizes. In doing so, not only were the same imperfect scaling factors used, but by the nature of zooming the pixel values were smoothed and their actual quantitative values altered.

Existing real mouse data obtained from an Inveon small animal PET scanner (the same scanner used in our simulations) was used to validate simulation results. However, an accurate comparison of the real mouse and MOBY phantom is difficult since the length/diameter ratios are not the same. Nevertheless, a rough comparison can be made with respect to the diameter sizes, as in 3D imaging most of the counts come from direct sinograms formed by the detection of annihilation photons traveling on the transaxial plane (i.e, along the diameter of the object). In fact, the mean error percents found for the second smallest size MOBY phantom (2.9 cm) were similar to that of real mouse (2.7 cm).

We intended to conduct a similar study with the real SPECT data from the Inveon multimodality system. However, Inveon SPECT scanner software does not have an attenuation correction algorithm installed and the scatter correction is limited to energy-based methods, which is default for any SPECT system. Therefore, we could not perform a similar analysis for various reconstruction conditions on the Inveon SPECT system.

Conclusion

Both ROI studies on the reconstructed images from the real mouse data and GATE simulations of the MOBY phantoms indicated that, regardless of the method used, correction for attenuation is absolutely necessary for the quantitative accuracy of small animal PET imaging. The attenuation correction is particularly effective in all hot regions and for cold regions smaller than 4 cm diameter.

Our results suggest that many PET small animal imaging studies can be performed by applying uniform attenuation correction without needing an additional transmission scan depending on the size of the animal and the accuracy level desired. The error results presented here for various animal sizes and imaging regions can be used as a guide for deciding the correction method for a particular study. For example, a mouse size up to 4 cm diameter can be imaged with less than 6% error using only uniform attenuation correction. If this error is acceptable for the objective of a given study, transmission-based correction may not be necessary.

In cold regions for diameter sizes larger than 4 cm, attenuation correction (without scatter correction) does not provide significant improvement, and in some cases elevates the error level even further. Therefore, for imaging larger animal sizes with low activity regions and heterogeneous tissue distribution (e.g. thorax), sophisticated correction methods employing transmission data may be necessary.

CHAPTER VI

SUMMARY AND FUTURE DIRECTIONS

In human PET and SPECT imaging, an additional transmission scan is often required to obtain accurate attenuation maps for attenuation and scatter corrections. These methods have been translated to small animal imaging, although the impact of photon interactions on the reconstruction of mouse/rat images is significantly less than that in human imaging. The value of these sophisticated correction methods is not obvious, considering the cost of additional instrumentation, complexity, software, and requirement of more dedicated computers (faster CPU and larger memory). Therefore, investigation is necessary to determine if simpler methods based on emission data only would be sufficient for small animal imaging.

We presented a series of simulation work performed on IDL and GATE for evaluation of the requirement for scatter and attenuation correction methods in PET and SPECT imaging. Our IDL simulations of a digital phantom and real chest data scaled to 5 different sizes (from human to mouse) showed the effect of attenuation correction in PET and SPECT imaging in the absence of scatter. Next, we performed scatter fraction simulations on GATE for a wide range of sizes of NEMA cylindrical phantoms (mouse, rat and human), MOBY (realistic mouse/rat model), and XCAT (human model) digital phantoms using human PET, small animal PET and SPECT scanners. Scatter fraction measurements allowed us to estimate the magnitude of scatter and the level of scatter correction required depending on the size of the object and scanner used. Finally, we performed ROI studies on the PET reconstructed images of six different sizes of MOBY phantoms and data from a real mouse study.

Our results from IDL simulations, scatter fraction simulations in GATE, and ROIs studies based on simulations and real small animal scanner were consistent with each other and in good agreement with the other works reported in the literature. Based on our

results we concluded that, for human 3D-PET imaging, accurate attenuation and sophisticated scatter corrections are necessary. In small animal PET and SPECT imaging, regardless the method, attenuation correction needs to be performed for all sizes. For objects larger than 4-5 cm additional scatter correction employing transmission data may also be necessary depending on the objective of a given study. The work presented here can be expanded in many directions, some of which are discussed here.

Our research only used traditional detectors, which employ common scintillator crystals NaI(Tl), BGO and LSO coupled to photo multiplier tubes (PMT). However, recently introduced semiconductor-based detector systems, such as CdTe and CdZnTe (CZT) detectors, are becoming increasingly popular in commercial SPECT systems. Because these scanners provide better energy resolution (e.g., 2-5% for 140 keV) [90], they can be operated using narrower energy windows, thus reducing scatter counts. For these systems, energy based scatter corrections would be more efficient because of the reduced scatter fraction. In addition, new SPECT scanner geometries introduced in recent years exhibit various designs compared to conventional dual-head cameras simulated in this work [91]. These relatively new systems would show a different characteristic for the scatter effect. A similar work can be performed to evaluate the effectiveness of the attenuation and scatter corrections for these new systems.

Our scatter fraction values were limited to the photon interactions occurring in the phantom only. Additional contributions to scatter, such as from the gantry and collimator, should be also considered when evaluating the impact of scatter on the reconstructed images.

Another shortcoming of our studies was that PET simulations of ROIs had considered only a single energy window (350-650 keV). However, the magnitude of scatter is highly dependent on the selection of energy window. Although this is a typical energy window used for ECAT and Inveon PET scanners, usage of other windows might be considered for particular applications (e.g., to increase the sensitivity). We partially

addressed this issue by performing additional scatter fraction simulations using a wider energy window (250-750 keV). Although the raw data values obtained from the wider window were significantly higher than those of narrow window, when the counts outside the object boundary set to zero (as in NEMA), the scatter fraction values from both windows were similar, in particular for smaller objects. This suggested that for sizes up to 5-6 cm similar correction approaches could be applied for both acquisitions.

In our analyses, we did not simulate transmission acquisition to obtain the attenuation map. Instead, we assumed that the scatter free sinograms represented corrections using transmission scan. Ideally, it would be useful to assess the accuracy of the transmission-based corrections. This could be addressed by using the new GATE version (v6), which includes simulation for CT imaging. Simulating combined PET/CT and SPECT/CT would allow more realistic approaches for the CT transmission based attenuation and scatter correction. However, CT simulations require additional computer resources.

Our scatter fraction measurements were performed for both PET and SPECT scanners. However, due to lengthy simulation times and limited computing resources, we restricted our simulations to PET small animal imaging. Since SPECT imaging is 100 times less sensitive than PET imaging, acquiring projection files from SPECT imaging was not practical with the given computing resource.

Finally, in this investigation we only considered scatter corrections employing transmission data. However, relatively simple approaches using emission data only (e.g., tail fitting method), could be also useful in reducing the errors. Future research could be done to compare the scatter correction methods in more detail.

REFERENCES

[1]   T. Beyer, *et al.*, "A combined PET/CT scanner for clinical oncology," *J Nucl Med,* vol. 41, pp. 1369-79, Aug 2000.

[2]   B. H. Hasegawa, K. H. Wong, K. Iwata, W. C. Barber, A. B. Hwang, A. E. Sakdinawat, M. Ramaswamy, D. C. Price, and R. A. Hawkins, "Dual-modality imaging of cancer with SPECT/CT," *Technol Cancer Res Treat,* vol. 1, pp. 449-58, Dec 2002.

[3]   A. Del Guerra and N. Belcari, "Advances in animal PET scanners," *Q J Nucl Med,* vol. 46, pp. 35-47, Mar 2002.

[4]   R. Golestani, C. Wu, R. A. Tio, C. J. Zeebregts, A. D. Petrov, F. J. Beekman, R. A. Dierckx, H. H. Boersma, and R. H. Slart, "Small-animal SPECT and SPECT/CT: application in cardiovascular research," *Eur J Nucl Med Mol Imaging,* Jan 13 2010.

[5]   H. Liang, Y. Yang, K. Yang, Y. Wu, J. M. Boone, and S. R. Cherry, "A microPET/CT system for in vivo small animal imaging," *Phys Med Biol,* vol. 52, pp. 3881-94, Jul 7 2007.

[6]   W. Wang, M. Chen, S. Carlin, C. Oehler, P. Zanzonico, and J. Humm, "Impact of attenuation and scatter correction in estimating tumor hypoxia-related kinetic parameters for FMISO dynamic animal-PET imaging," in *Nuclear Science Symposium Conference Record, 2008 NSS,IEEE*, 2008, pp. 5234-5239.

[7]   Y. Yongfeng and S. R. Cherry, "Observations regarding scatter fraction and NEC measurements for small animal PET," *Nuclear Science, IEEE Transactions on,* vol. 53, pp. 127-132, 2006.

[8]   H. Zaidi and B. H. Hasegawa, "Attenuation Correction Strategies in Emission Tomography," in *Quantitative Analysis in Nuclear Medicine Imaging.* , H. Zaidi, Ed., ed New York: Springer Science, 2006.

[9]   H. Zaidi and K. F. Koral, "Scatter Correction Strategies in Emission Tomography," in *Quantitative Analysis in Nuclear Medicine Imaging.* , H. Zaidi, Ed., ed New York: Springer Science, 2006, pp. 207-208.

[10]   S. Jan, *et al.*, "GATE: a simulation toolkit for PET and SPECT," *Phys Med Biol,* vol. 49, pp. 4543-61, Oct 7 2004.

[11]   *GATE publications*. Available: http://www.opengatecollaboration.org/publications/peer-reviewed-papers.html

[12]   "Performance Measurements of Small Animal Positron Emission Tomographs. NEMA Standards Publication NEMA NU 4-2008, National Electrical Manufacturers Assocation."

[13]   "NEMA Standards Publication NU 4-2008 Performance Measurements of Small Animal PET ".

[14] W. P. Segars, M. Mahesh, T. J. Beck, E. C. Frey, and B. M. Tsui, "Realistic CT simulation using the 4D XCAT phantom," *Med Phys,* vol. 35, pp. 3800-8, Aug 2008.

[15] W. P. Segars, B. M. Tsui, E. C. Frey, G. A. Johnson, and S. S. Berr, "Development of a 4-D digital mouse phantom for molecular imaging research," *Mol Imaging Biol,* vol. 6, pp. 149-59, May-Jun 2004.

[16] A. C. Kak and M. Slaney, *Principles of Computerized Tomographic Imaging*: Society of Industrial and Applied Mathematics, 2001.

[17] B. M. W. Tsui and E. C. Frey, "Analytic Image Reconstruction Methods in Emission Computed Tomography.," in *Quantitative Analysis in Nuclear Medicine Imaging.* , H. Zaidi, Ed., ed New York: Springer Science, 2006, pp. 83-85.

[18] S. R. Cherry and M. Dahlbom, *PET: Physics, Instrumentation, and Scanners*. New York, NY: Springer, 2006.

[19] D. S. Lalush and M. N. Wernick, "Iterative Image Reconstruction," in *Emission Tomography: The Fundamentals of PET and SPECT* M. N. Wernick and J. N. Aarsvold, Eds., ed San Diego: Elsevier Academic Press, 2004, pp. 443-472.

[20] M. T. Madsen, "Recent advances in SPECT imaging," *J Nucl Med,* vol. 48, pp. 661-73, Apr 2007.

[21] U. Nestle, W. Weber, M. Hentschel, and A. L. Grosu, "Biological imaging in radiation therapy: role of positron emission tomography," *Phys Med Biol,* vol. 54, pp. R1-25, 2009.

[22] C. M. Feng, S. Narayana, J. L. Lancaster, P. A. Jerabek, T. L. Arnow, F. Zhu, L. H. Tan, P. T. Fox, and J. H. Gao, "CBF changes during brain activation: fMRI vs. PET," *Neuroimage,* vol. 22, pp. 443-446, 2004.

[23] S. R. Cherry, J. A. Sorenson, and M. E. Phelps, *Physics in Nuclear Medicine*, 3 ed. Philadelphia, PA: Saunders, 2003.

[24] T. Jones, "The role of positron emission tomography within the spectrum of medical imaging," *Eur J Nucl Med,* vol. 23, pp. 207-211, 1996.

[25] S. W. Schwarz, C. J. Anderson, and J. B. Downer, "Radiochemistry and Radipharmacology " in *Nuclear Medicine Technology and Techniques*, R. B. Donald, P. E. Christian, and J. K. Langan, Eds., 4 ed St. Louis, 1997, pp. 160-168.

[26] M. D. Harpen, "Positronium: Review of symmetry, conserved quantities and decay for the radiological physicist " *Medical Physics,* vol. 31, 2004.

[27] S. J. Park, W. L. Rogers, and N. H. Clinthorne, "Effects of Positron Range and Annihilation Photon Acolinearity on Image Resolution of a Compton PET," *Nuclear Science, IEEE Transactions on Nuclear Science,* vol. 54, pp. 1543-1552, 2007.

[28] S. W. Schwarz, C. J. Anderson, and J. B. Downer, "Radiochemistry and Radiopharmacology," in *Nuclear Medicine and Technology*, D. R. Bernier, P. E. Christian, and J. K. Langan, Eds., 4 ed St. Louis,Missouri, 1997, pp. 164-166.

[29]   E. V. Garcia, T. L. Faber, C. D. Cooke, and R. D. Folks, "Computer Analysis of Nuclear Cardiology Procedures," in *Emission Tomography: The Fundamentals of PET and SPECT* M. N. Wernick and J. N. Aarsvold, Eds., ed San Diego: Elsevier Academic Press, 2004, p. 543.

[30]   S. Dadparvar, R. Hussain, S. P. Koffler, M. M. Gillan, E. I. Bartolic, and C. Miyamoto, "The role of Tc-99m HMPAO functional brain imaging in detection of cerebral radionecrosis," *Cancer J,* vol. 6, pp. 381-7, Nov-Dec 2000.

[31]   F. H. Fahey, Z. R. Abramson, B. L. Padwa, R. E. Zimmerman, D. Zurakowski, M. Nissenbaum, L. B. Kaban, and S. T. Treves, "Use of (99m)Tc-MDP SPECT for assessment of mandibular growth: development of normal values," *Eur J Nucl Med Mol Imaging,* vol. 37, pp. 1002-10, May 2010.

[32]   G. L. Zeng, J. R. Galt, M. N. Wernick, R. A. Mintzer, and J. N. Aarsvold, "Single-Photon Emission Computed Tomography," in *Emission Tomography: The Fundamentals of PET and SPECT* M. N. Wernick and J. N. Aarsvold, Eds., ed San Diego: Elsevier Academic Press, 2004.

[33]   C. Soler, P. Beauchesne, K. Maatougui, T. Schmitt, F. G. Barral, D. Michel, F. Dubois, and J. Brunon, "Technetium-99m sestamibi brain single-photon emission tomography for detection of recurrent gliomas after radiation therapy," *Eur J Nucl Med,* vol. 25, pp. 1649-57, Dec 1998.

[34]   H. H. Ertl, L. E. Feinendegen, and H. J. Heiniger, "Iodine-125, a Tracer in Cell Biology: Physical Properties and Biological Aspects," *Phys Med Biol,* vol. 15, pp. 447-456, 1970.

[35]   T. K. Leipert, J. D. Baldeschwieller, and D. A. Shirley, "Applications of Gamma Ray Angular Correlations to the Study of Biological Macromolecules in Solution," *Nature* vol. 220, pp. 907-909, 1968.

[36]   L. A. Feldkamp, L. C. Davis, and J. W. Kress, "Practical cone-beam algorithm," *J. Opt Soc Am.,* vol. 1, pp. 612-619, 1984.

[37]   N. Karakatsanis*, et al.*, "Comparative evaluation of two commercial PET scanners, ECAT EXACT HR+ and Biograph 2, using GATE," *Nuclear Instruments and Methods in Physics Research,* vol. 569, pp. 368-372, 2006.

[38]   R. D. Evans, *The Atomic Nucleus*, 14 ed. New York: McGraw-Hill, 1972.

[39]   F. H. Attix, *Introduction to Radiological Physics and Radiation Dosimetry*: John Wiley & Sons, 1986.

[40]   *X-Ray Mass Attenuation Coefficients.* Available: http://physics.nist.gov/PhysRefData/XrayMassCoef/tab2.html

[41]   M. J. Berger, J. H. Hubbell, S. M. Seltzer, J. Chang, J. S. Coursey, Sukumar, and D. S. Zucker. *XCOM: Photon Cross Sections Database*. Available: http://physics.nist.gov/PhysRefData/Xcom/Text/XCOM.html

[42]   H. Zaidi and B. Hasegawa, "Determination of the attenuation map in emission tomography " *J Nucl Med,,* vol. 44, pp. 291-315, 2003.

[43]   P. D. Shreve, "Whole Body PET Imaging Methods," in *Positron Emission Tomography: Basic Science* ed London: Springer, 2005.

[44]   A. M. Alessio, P. E. Kinahan, P. M. Cheng, H. Vesselle, and J. S. Karp, "PET/CT scanner instrumentation, challenges, and solutions," *Radiol Clin North Am,* vol. 42, pp. 1017-32, vii, Nov 2004.

[45]   M. Hofmann, B. Pichler, B. Scholkopf, and T. Beyer, "Towards quantitative PET/MRI: a review of MR-based attenuation correction techniques," *Eur J Nucl Med Mol Imaging,* vol. 36 Suppl 1, pp. S93-104, Mar 2009.

[46]   D. Wagenaar*, et al.*, "A multi-ring small animal CZT system for simultaneous SPECT/MRI imaging," *J. Nucl. Med.,* vol. 48 (Supplement 2), p. 89, 2007.

[47]   A. Krol, J. E. Bowsher, S. H. Manglos, D. H. Feiglin, M. P. Tornai, and F. D. Thomas, "An EM algorithm for estimating SPECT emission and transmission parameters from emissions data only," *IEEE Trans Med Imaging,* vol. 20, pp. 218-32, Mar 2001.

[48]   R. Licho, S. J. Glick, W. Xia, T. S. Pan, B. C. Penney, and M. A. King, "Attenuation compensation in 99mTc SPECT brain imaging: a comparison of the use of attenuation maps derived from transmission versus emission data in normal scans," *J Nucl Med,* vol. 40, pp. 456-63, Mar 1999.

[49]   L.-T. Chang, "A Method for Attenuation Correction in Radionuclide Computed Tomography " *Tomography Nuclear Science, IEEE Transactions on,,* vol. 25, pp. 638-643, 1978.

[50]   P. E. Kinahan, D. W. Townsend, T. Beyer, and D. Sashin, "Attenuation correction for a combined 3D PET/CT scanner," *Med Phys,* vol. 25, pp. 2046-53, Oct 1998.

[51]   K. Wienhard, M. Dahlbom, L. Eriksson, C. Michel, T. Bruckbauer, U. Pietrzyk, and W. D. Heiss, "The ECAT EXACT HR: performance of a new high resolution positron scanner," *J Comput Assist Tomogr,* vol. 18, pp. 110-8, Jan-Feb 1994.

[52]   T. Lewellen and J. Karp, "PET systems " in *Emission Tomography: The Fundamentals of PET and SPECT*, M. Wernick and J. Aarsvold, Eds., ed San Diego: Elsevier Academic Press, 2004, p. 190.

[53]   A. Rahmim and H. Zaidi, "PET versus SPECT: strengths, limitations and challenges," *Nucl Med Commun,* vol. 29, pp. 193-207, Mar 2008.

[54]   S. R. Cherry and S.-C. Huang, "Effects of scatter on model parameter estimates in 3D PET studies," *iEEE Transactions on Nuclear Science,* vol. 42, pp. 1174-1179, 1995.

[55]   Y. Yang and S. R. Cherry, "Observations Regarding Scatter Fraction and NEC Measurements For Small Animal PET," *iEEE Transactions on Nuclear Science,* vol. 53, pp. 127-132, 2006.

[56]   I. Buvat, M. Rodriguez-Villafuerte, A. Todd-Pokropek, H. Benali, and R. D. Paola, "Comparative assessment of nine scatter correction methods based on spectral analysis using Monte Carlo simulations," *J Nucl Med,* vol. 36, pp. 1476-88, Aug 1995.

[57]   K. Ogawa, Y. Harata, T. Ichihara, A. Kubo, and S. Hashimoto, "A practical method for position-dependent Compton-scatter correction in single photon emission CT," *IEEE Trans Med Imaging,* vol. 10, pp. 408-12, 1991.

[58]   D. L. Bailey and S. R. Meikle, "A convolution-subtraction scatter correction method for 3D PET " *Phys. Med and Bio,* vol. 39, pp. 411-424, 1994.

[59]   C. E. J. Floyd, R. J. Jaszczak, K. L. Greer, and R. E. Coleman, "Deconvolution of Compton scatter in SPECT," *J. Nucl. Med.,* vol. 26, pp. 403-408, 1985.

[60]   J. S. Karp, G. Muehllehner, D. A. Mankoff, C. E. Ordonez, J. M. Ollinger, M. E. Daube-Witherspoon, A. T. Haigh, and D. J. Beerbohm, "Continuous-Slice PENN-PET: A Positron Tomograph with Volume Imaging Capability " *J. Nuclear Med,* vol. 31, pp. 617-627, 1990.

[61]   S. R. Cherry and S.-C. Huang, "Effects of scatter on model parameter estimates in 3D PET studies of the human brain," *Nuclear Science IEEE Transactions,* vol. 42, pp. 1174-1179, 1995.

[62]   D. L. Bailey, "Quantitative Procedures in 3D PET," in *The Theory and Practice of 3D PET,* , B. Bendriem and D. W. Townsend, Eds., ed: Kluwer Academic, 1998, p. 77.

[63]   J. M. Ollinger, "Model-based scatter correction for fully 3D PET," *Phys Med Biol,* vol. 41, pp. 153-76, Jan 1996.

[64]   D. L. Bailey, "Transmission scanning in emission tomography," *Eur J Nucl Med,* vol. 25, pp. 774-87, Jul 1998.

[65]   J. S. Barney, J. G. Rogers, R. Harrop, and H. Hoverath, "Object shape dependent scatter simulations for PET " *iEEE Transactions on Nuclear Science,* vol. 38, pp. 719-725, 1991.

[66]   A. S. Goggin and J. M. Ollinger, "A model for multiple scatters in fully 3D PET," in *Nuclear Science Symposium and Medical Imaging Conference*, 1994, pp. 1609-1613.

[67]   C. C. Watson, "New, faster, image-based scatter correction for 3D PET " *iEEE Transactions on Nuclear Science,* vol. 47, pp. 1587-1594, 2000.

[68]   H. Zaidi, "Monte Carlo Modeling in Nuclear Medicine Imaging," in *Quantitative Analysis in Nuclear Medicine Imaging*, Z. H., Ed., ed New York: Springer, 2006, pp. 358-363.

[69]   I. Buvat and I. Castiglioni, "Monte Carlo simulations in SPET and PET," *The quarterly journal of nuclear medicine, ,* vol. 46, pp. 48-61, 2002.

[70]   R. Harrison. *Simulation System for Emission Tomography*. Available: http://depts.washington.edu/simset/html/simset_main.html

[71]   N. I. a. M. S. Agostinelli et al., "Geant4 - A Simulation Toolkit," *Nuclear Instruments and Methods A 506,* pp. 250-303, 2003.

[72] P. L. Chow, F. R. Rannou, and A. F. Chatziioannou, "Attenuation correction for small animal PET tomographs," *Phys Med Biol,* vol. 50, pp. 1837-50, Apr 21 2005.

[73] I. Buvat and D. Lazaro, "Monte Carlo simulations in emission tomography and GATE: An overview: " in *Proceedings of the 3rd International Conference on Imaging Technologies in Biomedical Sciences - Innovation in Nuclear and Radiological Imaging: from Basic Research to Clinical Application Nuclear Instruments and Methods in Physics Research Section A: Accelerators, Spectrometers, Detectors and Associated Equipment*, Paris, 2006, pp. 323-329.

[74] K. Wienhard, M. Dahlbom, L. Eriksson, C. Michel, T. Bruckbauer, U. Pietrzyk, and W. D. Heiss, "The ECAT EXACT HR: Performance of a New High Resolution Positron Scanner," *Journal of Computer Assisted Tomography,* vol. 18, pp. 110-118, 1994.

[75] C. C. Constantinescu and J. Mukherjee, "Performance evaluation of an Inveon PET preclinical scanner," *Phys Med Biol,* vol. 54, pp. 2885-99, May 7 2009.

[76] D. W. Austin, M. J. Paulus, S. S. Gleason, R. A. Mintzer, S. B. Siegel, S. D. Figueroa, T. J. Hoffman, and J. S. Wall, "Design and Performance of a New SPECT Detector for Multimodality Small Animal Imaging Platforms " in *IEEE Nuclear Science Symposium Conference Record*, 2006 IEEE Nuclear Science Symposium Conference Record.

[77] J. Sebastien, C. Comtat, D. Strul, G. Santin, and R. Trebossen, "Monte Carlo Simulation for the ECAT EXACT HR+ System Using GATE," *iEEE Transactions on Nuclear Science,* vol. 52, pp. 627-633, 2005.

[78] C. C. Watson, D. Newport, M. E. Casey, R. A. DeKemp, R. S. Beanlands, and M. Schmand, "Evaluation of simulation-based scatter correction for 3-D PET cardiac imaging," *Nuclear Science IEEE Transactions,* vol. 44, pp. 90-97, 1997.

[79] T. Mizuta, K. Kitamura, H. Iwata, Y. Yamagishi, A. Ohtani, K. Tanaka, and Y. Inoue, "Performance evaluation of a high-sensitivity large-aperture small-animal PET scanner: ClairvivoPET," *Ann Nucl Med,* vol. 22, pp. 447-55, Jun 2008.

[80] A. F. Chatziioannou, S. R. Cherry, Y. Shao, R. W. Silverman, K. Meadors, T. H. Farquhar, M. Pedarsani, and M. E. Phelps, "Performance evaluation of microPET a high-resolution lutetium oxyorthosilicate PET scanner for animal imaging," *J Nucl Med,* vol. 40, pp. 1164-1175, 1999.

[81] J. S. Kim, J. S. Lee, M. J. Park, S. J. Hong, and D. S. Lee, "Comparative Evaluation of Three MicroPET Series Systems Using Monte Carlo Simulation: Sensitivity and Scatter Fraction " in *IEEE Nuclear Science Symposium Conference Record*, 2007.

[82] S. Surti, A. Kuhn, M. E. Werner, A. E. Perkins, J. Kolthammer, and J. S. Karp, "Performance of Philips Gemini TF PET/CT scanner with special consideration for its time-of-flight imaging capabilities," *J Nucl Med,* vol. 48, pp. 471-80, Mar 2007.

[83]   L. Eriksson, *et al.*, "The ECAT HRRT: An example of NEMA scatter estimation issues for LSO based PET systems," *IEEE Transactions on Nuclear Science,* vol. 52, pp. 90-94, 2004.

[84]   A. Ferrero, J. K. Poon, and R. D. Badawi, "Characterization of the scatter fraction arising from different sized objects – a simulation study," 2009.

[85]   Q. Bao, D. Newport, M. Chen, D. B. Stout, and A. F. Chatziioannou, "Performance evaluation of the inveon dedicated PET preclinical tomograph based on the NEMA NU-4 standards," *J Nucl Med,* vol. 50, pp. 401-408, Mar 2009.

[86]   B. J. Kemp, C. B. Hruska, A. R. McFarland, M. W. Lenox, and V. J. Lowe, "NEMA NU 2-2007 performance measurements of the Siemens Inveon(TM) preclinical small animal PET system,," *Phys. Med and Bio,* vol. 54, pp. 2359-2376, 2009.

[87]   P. E. Kinahan and J. G. Rogers, "Analytic 3D image-reconstruction using all detected events," *IEEE Trans Nucl Sci,* vol. 36, pp. 964-968, 1989.

[88]   R. Yao, J. Seidel, J.-S. Liow, and M. V. Green, "Attenuation Correction for the NIH ATLAS Small Animal PET Scanner," *iEEE Transactions on Nuclear Science,* vol. 52, pp. 664-668, 2005.

[89]   P. K. Hooper, S. R. Meikle, S. Eberl, and M. J. Fulham, "Validation of postinjection transmission measurements for attenuation correction in neurological FDG-PET studies," *J Nucl Med,* vol. 37, pp. 128-36, Jan 1996.

[90]   D. J. Wagenaar, "CdTe and CdZnTe Semiconductor Detectors for Nuclear Medicine Imaging " in *Emission Tomography: The Fundamentals of PET and SPECT* M. N. Wernick and J. N. Aarsvold, Eds., ed San Diego: Elsevier Academic Press, 2004.

[91]   K. Erlandsson, K. Kacperski, D. v. Gramberg, and B. F. Hutton, "Performance evaluation of D-SPECT: a novel SPECT system for nuclear cardiology " *Phys Med Biol,* vol. 54, pp. 2635-2649, 2009.